博士論文

Reaction Pathway Analysis for the Mobility of Partial Dislocation in 3C-SiC and Shuffle-set Perfect Dislocation in Silicon

（3C-SiCの部分転位とシリコンのシャフルセット完全転位の移動度に関する反応経路解析）

楊晶

THE UNIVERSITY OF TOKYO

Reaction Pathway Analysis for the Mobility of Partial Dislocation in 3C-SiC and Shuffle-set Perfect Dislocation in Silicon

by

楊晶

A thesis submitted in partial fulfillment for the
PhD degree

Department of Mechanical Engineering
School of Engineering

Feb 2016

Abstract

Dislocations are linear defects that carry out the plastic flow at the microscopic scale, and have strongly influence on semiconductor materials' electric and mechanic properties. During the wafer growth of the semiconductor materials by CVD, dislocation propagation is thought to be one of main factors that cause the wafer warpage. With the purpose of obtaining a high quality of wafer, the reaction pathway analysis is performed for a good understanding of the dislocation propagation in wafer.

In this paper, the mobility of Shockley partial dislocations in 3C-SiC and Shuffle-set perfect dislocation in silicon have been investigated by reaction pathway analysis. For 3C-SiC, there are two types of dislocations according to which kind of atom, Si or C, comprises the core edge of the dislocation line. 3C-SiC is represented by Vashishta potential function, and the reaction path of kink pair nucleation and kink migration are investigated by NEB. The dependence of the activation energy on the driving shear stress has been obtained. The results show that during kink migration, 30 °partial dislocations have a lower activation energy barrier than 90 °partial dislocation. And, C-core partial dislocations have a higher activation energy barrier than Si-core dislocations for both degrees of partial dislocations during kink migration and nucleation. This conclusion is consistent with the experimental result that Si-core dislocations migrate more readily than C-core dislocations. Besides I have found that the partial dislocation with a larger distance between the dangling bond atoms along the dislocation line also has a higher activation energy barrier for both 30 °and 90 °partial dislocations. Moreover, based on the activation energy barrier calculation, new models are proposed to explain the morphological character of different partial dislocation lines that the 30 ° partial dislocation lines prefer to be smooth because of the large activation energy difference between kink nucleation and kink migration. And the 90 ° partial dislocations lines prefer to be zigzagged for the reason that the 90 ° partial dislocation lines have the possibility to migrate and nucleate simultaneously. Based on our mobility analysis, the stacking fault morphologies have been discussed. Our consultations agree well with previous experiment data.

For the shuffle-set perfect dislocation analysis in silicon, the EDIP potential function is employed for representing the silicon. There are three possible shuffle-set dislocation core structures named as S1, S2 and S3. Here, the activation energy barriers of the kink migration and nucleation in S1and S2 types are investigated by NEB method. The simulation results show that the resolved shear strain of the shuffle-set dislocation in S1 type is around 5%, and the S1 type is the dominate one in the shear strain of 0% to 5%. I also have found that the activation energy barriers of the two sides kink migration is nearly two times than that of the one side kink migration. More interestingly, the kink

nucleation path is accomplished by the motion of two atoms simultaneously. These phenomena could be responsible for the missing long segment of shuffle-set perfect dislocation in the experiment observation. I am guessing whether it is possible that the dislocation propagation and the movement of shuffle-set perfect dislocation segment have different mechanisms. During the shear strain from 5% to 12.5%, the dislocation can move as the S1 core kink nucleation and migration and the S1 dislocation core is in process of transforming into S2. The S2 dislocation core structures begin to appear along the S1 dislocation line since the shear strain is larger than 5% shear strain, and the transition is ended around the shear strain 12.5%. The kink structures are asymmetric in S2 dislocation and both the LK and RK migration process have been studied. In the RK migration process with S2 dislocation we find that both the shuffle-set and glide-set bond breaking and forming are involved. This may imply that there could be a possibility that the shuffle-set dislocation core can translated into a glide-set dislocation core. The high activation energy barrier indicates that this transition could only happen in high temperature. S3 dislocation motion is not considered here for the bad representation of kink structures.

We believe that our dislocation reaction pathway analysis can improve our understanding of dislocation motion in 3C-SiC and silicon and provide more evidences for solving the unclear issues in both of them.

Keywords: Reaction path way, partial dislocation, shuffle-set perfect dislocation, 3C-SiC, silicon, activation energy barriers, dislocation line morphology, stacking fault morphology

Contents

List of Figures

List of Tables

Chapter 1

1 Background and motivation

1.1 Defects in crystal

In nature, there is no pure perfect crystal for the reason that the atom arrangement in the real material is not always in a regular pattern. The irregular part is called defect. Based on the dimension of defects, people name them as point defect for zero dimension, dislocation for one dimension, planer for two dimension and bulk for third dimension.

1.1.1 Point defects

Several types of point defects have been showed in Fig.1. Generally, there are two kinds of point defects, the intrinsic and the extrinsic defects. The defects with missing atoms in the original lattice structure, or an atom located in the lattice where no atom should appear in the perfect lattice are called intrinsic defects. Vacancies can diffuse to neighboring atomic sites through the movement of neighboring atoms which affect the atom migration in crystal lattice. Interstitial defects usually have higher energy than the regular lattice structure. Notice that, the

new located atom is same to or one kind of atoms in the original lattice. In Fig.1.1 (b), we can see that the extrinsic point defects can be formed by replacing the original atoms to other kinds of atoms. These extrinsic point defects have influence on electrical and mechanical properties for semiconductor materials and metal or alloy respectively.

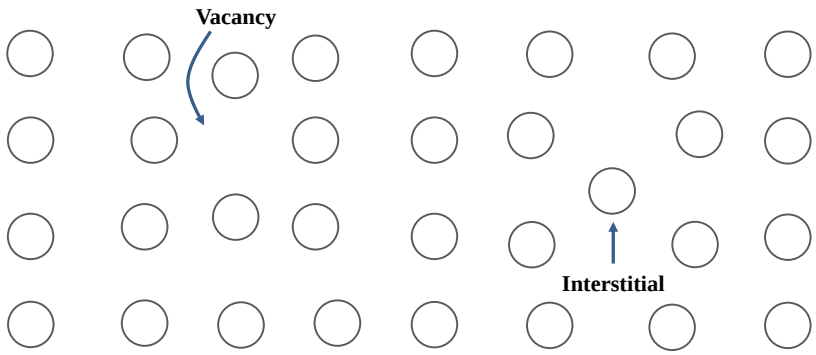

(a) Schematic representation of intrinsic point defect.

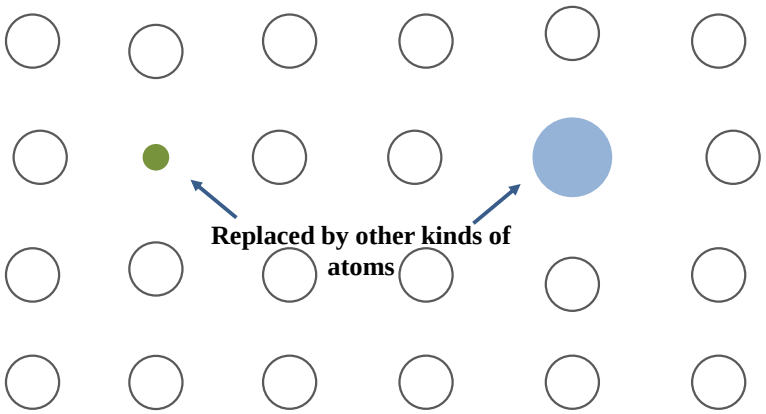

(b) Schematic representation of extrinsic point defect.

Figure 1.1 Schematic representations of point defects. (a) shows the vacancy and interstitial formed by missing or adding an atom respectively. (b) shows the extrinsic point defects formed by atom replaced by foreign atoms.

1.1.2 Linear defects

Dislocations are linear defects that carry out the plastic deformation at the microscopic scale, and have strongly influence on semiconductor materials' electrical and mechanical properties. The definition of dislocation was first proposed in the early 20 century, at that time, people find

a large difference between the theoretical estimation and experimental tests about the critical resolved shear stress. The stress shows the transition spot between the elastic deformation and plastic deformation in material. At that time, a rigid model, shown in Fig.1.2, was used for the theoretical estimation. The critical stress was calculated by breaking all the atomic bonds along the gliding surface which was 1000 times large than the experiment data. For a better explaining of the plastic deformation, the current dislocation theory had been proposed by Taylor (1934).

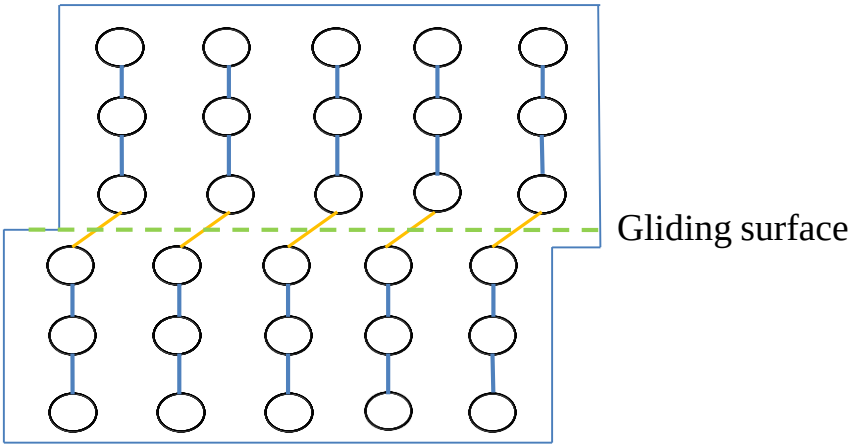

Figure 1.2 Rigid model for estimating the critical resolved shear stress in early 20 century.

Based on the dislocation theory, there are two kinds of dislocations, i.e., edge dislocation and screw dislocation. In the actual lattice structure, few of dislocations are pure edge or screw. Most of them are mixed by both edge and screw dislocations. Think the edge dislocation as an extra half plane of atoms inserted into the perfect crystal as shown in Fig.1.3.

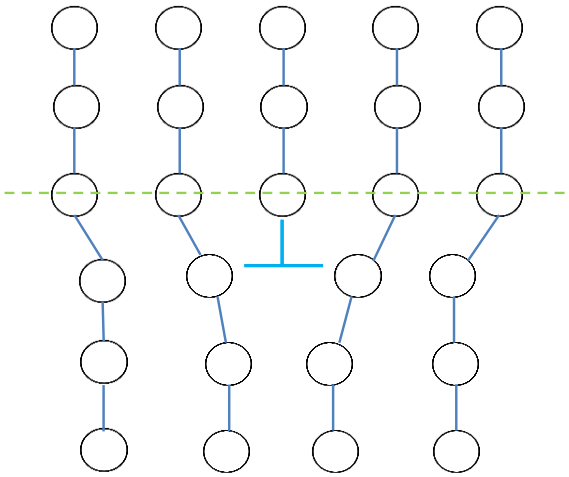

Figure 1.3 Schematic representation of edge dislocation. The dash line shows the slip plane and the upside down blue T mark is used to show the position of dislocation.

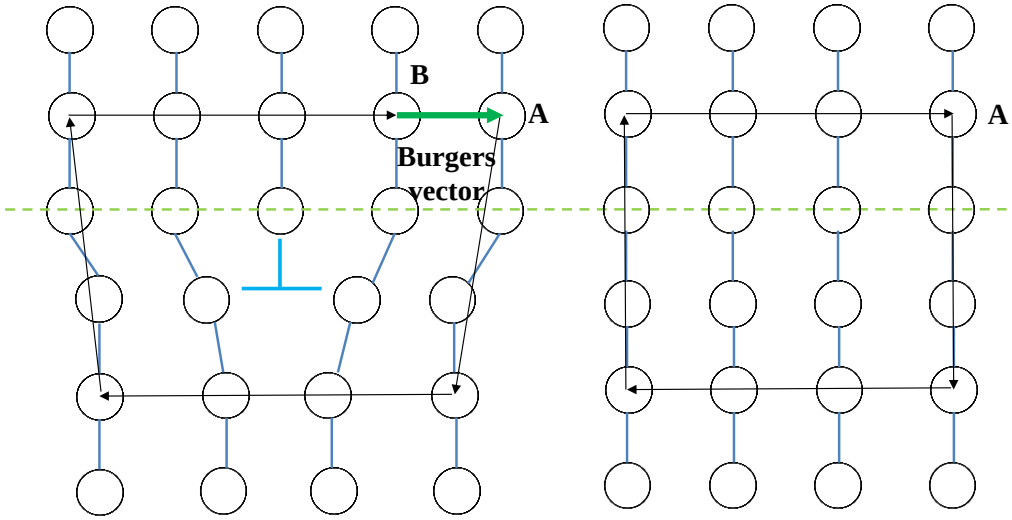

Figure 1.4 Schematic illustration of burgers vector. The green arrow is the burgers vector of this edge dislocation. The right figure shows the perfect crystal with an encompassed loop while the left one represents the edge dislocation with the same path of the loop. The encompassed loop in perfect crystal became to an open curve after an extra half plane atoms inserted. In the crystal with edge dislocation, the curve started from point A will reach point B, the vector from B to A is called Burgers vector.

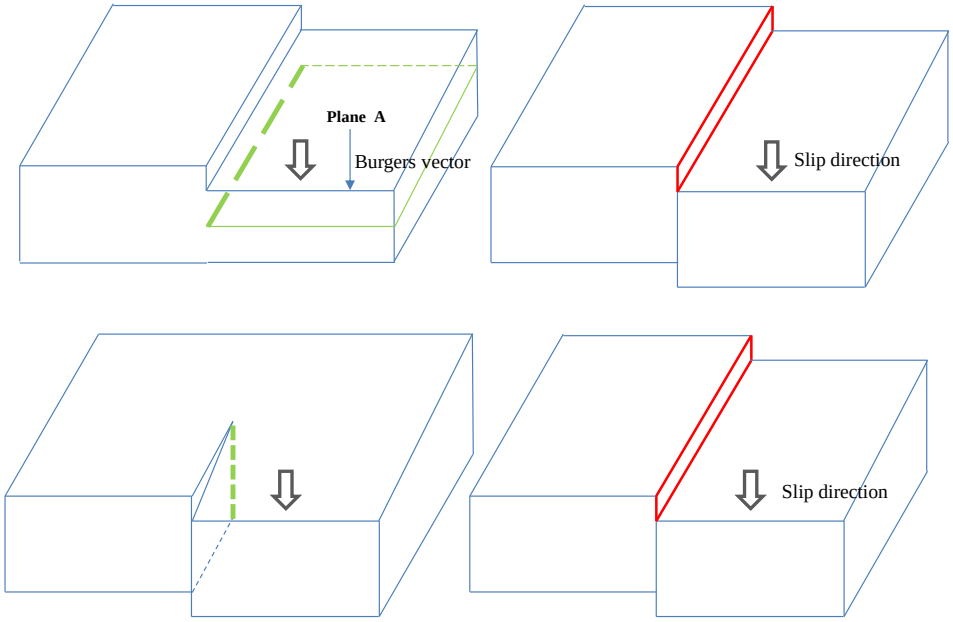

Figure 1.5 Schematic representation of difference between the edge and screw dislocation. The bolded dash lines represented the dislocation lines. The arrows show the slip direction. The upper two figures are for edge dislocations. The left one shows the crystal with edge dislocation, the area compassed by green lines is an extra half plane. The lower two figures show the screw dislocations. These two kinds of dislocations with same burgers vector can reach to the same final configuration after they slipped.

The light green dashed line shows the slip plane of the dislocation movement. With applying stress, dislocation can move on the slip plane until it comes out of the lattice surface. Usually, an upside down T is used to show the location of the dislocation and two possible move directions. Before the introduction of the screw dislocations, the burgers vector is illustrated in Fig. 1.4. Burgers vector shows the difference between the distorted crystal with dislocations and the perfect crystal. The burgers vector can be obtained by following steps. First, draw a encompassed loop in a perfect crystal, like 4×4×4 in Figure 1.4. This encompassed loop will deformed by the dislocation existing and became to an unclosed curve. The vector from the starting point to the ending point is called burgers vector. Based on the dislocation line and the direction of burgers vector, we can tell the difference between the screw dislocation and edge dislocation. As shown in Fig. 1.5, the upper figures show the slip process of the edge dislocation when the bottom figures for the screw dislocation. In the edge dislocation, the dislocation line is vertical to the direction of its burgers vector. While for the screw dislocation, the dislocation line is parallel to its burgers vector. As we mentioned, dislocations will keep slipping until they come out of the surface. Here, these two types of dislocations with same burgers vector can reach the same final configurations after the dislocation motion.

1.1.3 Plane defect

Stacking fault, grain boundaries and twin boundaries are three kinds of plane defects. In perfect crystal, the atoms are arranged periodically. For example, like ABCABCABC. As showing in Fig. 1.6, the stacking faults means this regular arrangement has been interrupted, the ABCABCABC became to ABCABABC. Here the whole plane of atom C is missing. This change in atoms sequence is called stacking fault, it is most likely to happened in the close packed plane such as the (111) plane in FCC (face centered cubic). The dislocation motion and applied stress can cause the formation of stacking faults. Grain boundaries are the interface between two regions of crystal with different crystal local coordination. In Fig. 1.7, the structure with grain boundaries has been illustrated. The bold green lines show the grain boundaries. These defects can be produced when serval pieces of crystal collapse with each other during the growth. The dislocations motion can be interrupted by the existing of grain boundaries.

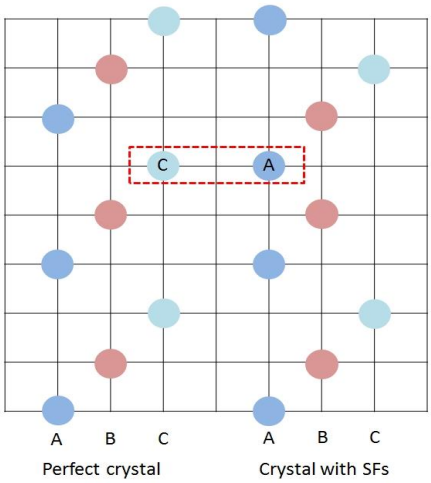

Figure 1.6 Atom arrangement of perfect crystal and the crystal with stacking faults (SFs).

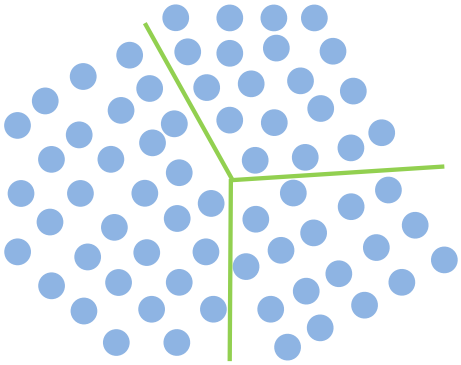

Figure 1.7 Schematic representation of grain boundaries. The green lines represent the grain boundaries

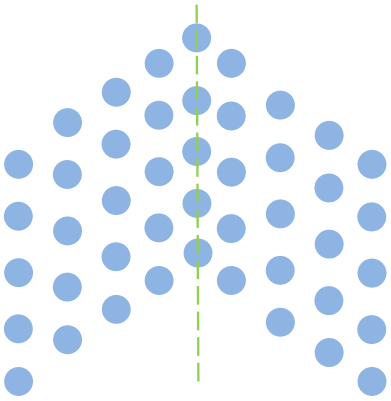

Figure 1.8 Schematic representation of twin boundaries.

In Fig. 1.8, the twin boundary marked by dash green line appearing as a mirror for both sides of the lattice. It can be formed by orientation change during the lattice growth or part of regular structure transform into another stable form by temperature and stress changing. Moreover, the interface of twin boundary has a lower energy than the grain boundary. Bulk defects have larger scale than previous mentioned defects. They can be formed by a region atoms missing from the lattice as void or part of the lattice transform into another type of atom arrangement as homogeneous.

1.2 Dislocation in semiconductor materials

In this paper, I focus on the dislocations analysis in the semiconductor such as silicon carbide and silicon. The dislocations as the carriers of the material plastic deformation have great influence on the materials' mechanic and electric properties. For the advanced semiconductor with extraordinary performance, the investigation of the dislocations can help us have a better understanding of these materials which are working under high temperature and high stress.

1.2.1 Dislocation motion in crystal structures

In the real crystal structures, there is no single and straight dislocation line. Dislocations move as kink pair functions because of the lattice resistance. Lattice resistance is one kind of atom interaction; like that the atoms will repel each other, when they are getting too close. Here, still use the edge dislocation for illustration, as shown in Fig. 1.9, the dislocation line is represented by a dashed green line. Notice that, the geometry of the dislocation looks like a line. It does not mean the atoms along the dislocation are connected one by one with strong atomic bonds. The atom along the dislocation line has an independent possibility to move. The Fig. 1.10 (Cai *et al*., 2004) is employed for easy understanding the dislocation motion mechanism. The dark area is the energy landscape, obtained by the Peierls stress estimation. The bottom valley shows the position where the dislocation can lie and the blue line is the dislocation. As shown in this figure, due the atom independent moving possibility, part of the dislocation has moved to new position while the rest part does not. Then this kind of structure is called kink.

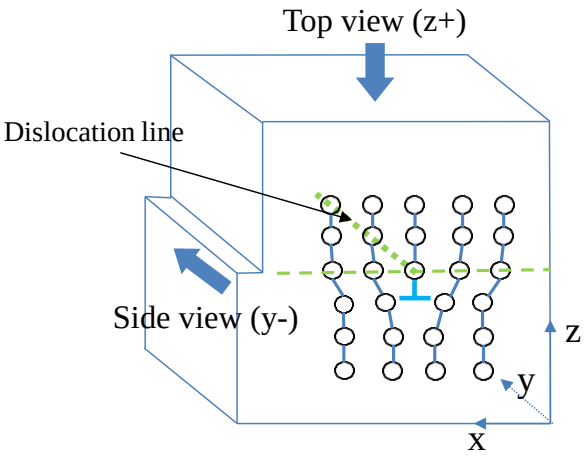

Figure 1.9 3D model of dislocation in crystal.

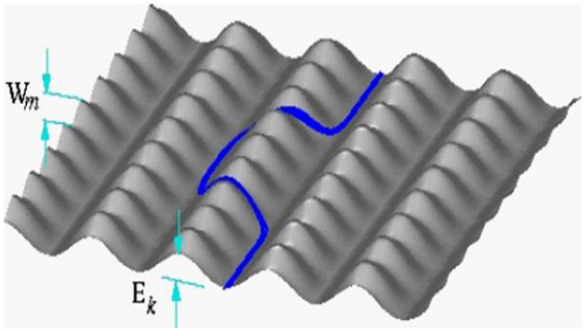

Figure 1.10 Schematic of the Peierls barrier and kink mechanism for dislocation motion. (Cai *et al*., 2004). With the permission from Elsevier.

On the other hands, the TEM studies (Shen *et al*., 2004 and Kolar *et al*., 1996) also showed that the straight dislocation was not observed. There are always kinks along the dislocation line as shown in Fig. 1.11. Generally, based on the dislocation theory, there are two states during the dislocation motion as kink pair function, the kink nucleation and kink migration. Use the 90 Si-core partial dislocation propagation processes for example. As shown in Fig. 1.12, the kink nucleation started from the single straight dislocation line, ended when a kink pair had been formed in the new dislocation position. Since the kink pair nucleated in the new position, it will expand the kink width; this kink width changing process is called kink migration. Therefore, our dislocation mobility study is focusing the kink nucleation and migration of the dislocation in Si and 3C-SiC.

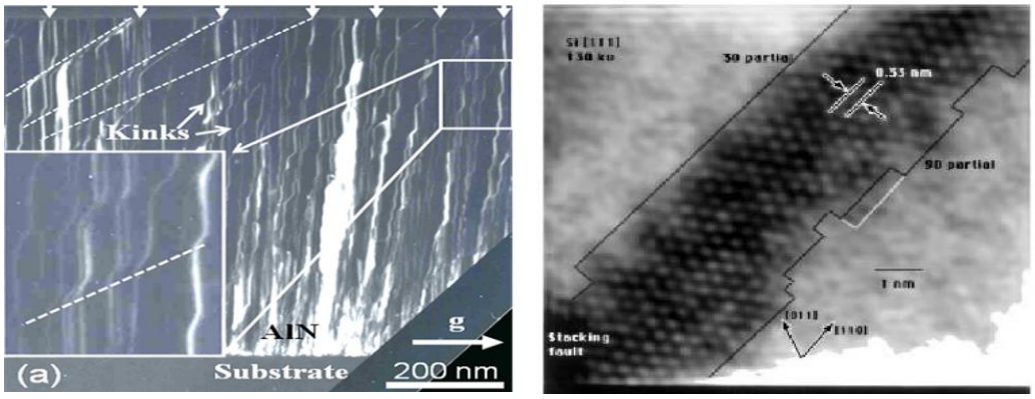

(a) (b)

Figure 1.11 (a) TEM image of Kink structures in AlN layers.(Shen *et al*., 2004) With the permission from AIP Publishing LLC. (b) TEM image of kink along the partial dislocation in silicon. (Kolar *et al*., 1996), With the permission from American Physical Society.

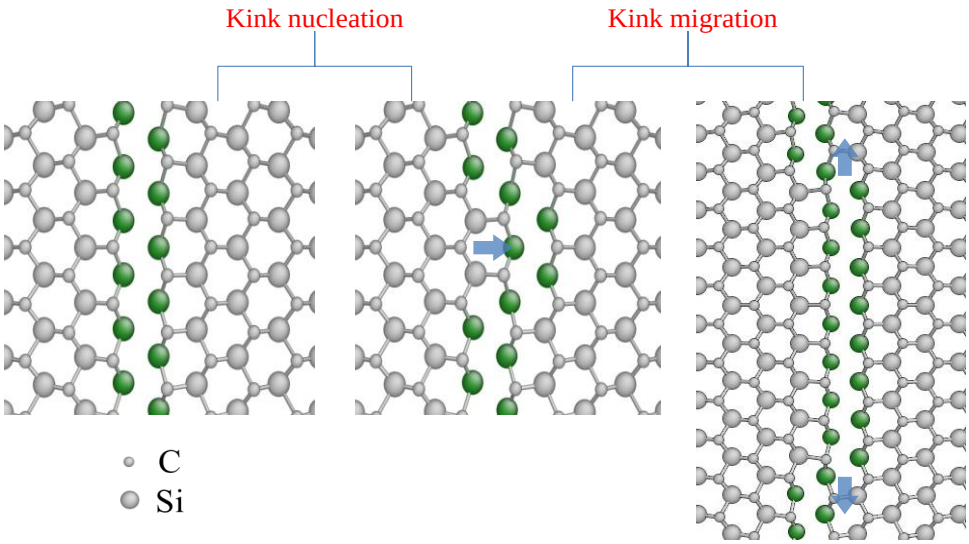

Figure 1.12 Kink nucleation and kink migration process in Si-core 90° partial dislocation propagation.

1.2.2 Dislocation in silicon carbide

Silicon, gallium nitride and silicon carbide are three major kinds of semiconductor materials which have been widely used in nowadays. Their material properties are shown in Table 1.1 (Levinshtein *et al*., 2001; Chow and Tyagi, 1994). The wide bond-gap, high saturation velocity and high thermal conductivity make the silicon carbide has excellent performance in high temperature, especially in the field of the high frequency and high power application (Sasaki *et al*., 1984; Ruff *et al*., 1994).

Table 1-1 Material parameters at 300 K

Materials	Silicon	GaN	SiC-3C	SiC-4H
Bond-gap(eV)	1.12	3.39	2.36	3.25
Electron Mobility (cm^2 /V-sec)	1400	2000	800	900(a-axis)
Electron Saturation Velocity (10^6 cm/sec)	10	22	20	25
Thermal Conductivity (Watts/cm•K)	1.5	1.3	5	4.5
Critical Field (10^6 V/cm)	0.3	3.3	1.2	3

Silicon Carbide has more than two hundred and fifty polytypes, the α-silicon carbide is one major type with hexagonal or rhombohedral crystal structure, such as 2H-SiC, 4H-SiC, 6H-SiC. Another major type is β-silicon carbide, the 3C-SiC, which has a lower growth temperature compared with α-silicon carbide and can be grown on silicon substrate by chemical vapor deposition method (CVD). With this lower formation temperature, 3C-SiC can be grown with a larger wafer diameter compared with other polytypes. The larger diameter of silicon carbide wafer is important in the semiconductor device manufacture. The unit cell of 3C-SiC is showed in Fig. 1.13. The green atoms and dark atoms represent the silicon and carbon respectively. In 3C-SiC the atoms number ratio of silicon to carbon is 1:1.

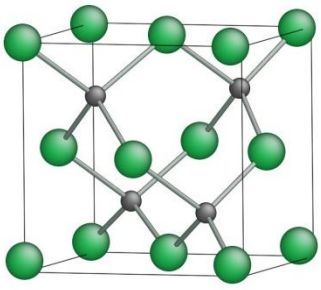

Figure 1.13 Unit cell of 3C-SiC.

During the growth of 3C-SiC on silicon, lattice mismatch caused by the difference in lattice constant and thermal misfit due to the differences in thermal expansion coefficient will contribute to large residual stress (Nagasawa and Yagi, 1997; Sun *et al*., 2012; Zielinski *et al*., 2007; Severino *et al*., 2007). The large stress induces a high dislocation density and wafer warpage in device manufacture. For a high quality of silicon carbide wafer with lower residual stress, researchers are focusing on the technical method approaching by optimizing the growth process (Wang *et al*., 2011; Nagasawa *et al*., 2006; Neudeck *et al*., 2006; Chaussende *et al*., 2008). As we mentioned in last section, the dislocation as the key role during the material

deformation, its nucleation and propagation is thought to be one of the main factors cause the wafer warpage. Therefore, for a good understanding of how to reduce dislocation density and the wafer warpage, the dislocation analysis is performed.

There are two types of dislocations in 3C-SiC due to which kind of atoms constitute the dislocation line, i.e. Si-core and C-core (Fig. 1.9). Moreover, all dislocations in all SiC polytypes are dissociated into two partials. Thus the screw dislocation is dissociated into two 30 ° partials, the 60 ° dislocation is dissociated into a 90 ° and a 30 ° partial dislocation (Pirouz and Yang, 1993). Fig. 1.14 shows the partial dislocation structures in close packed plane (111). Two columns of three-fold silicon atoms represented by green atoms are the dislocation line. The 90 ° and 30 ° partial dislocations mean the angle between the dislocation line and their burgers vector are 90 ° and 30 °, respectively. The dislocation dissociation is schematic represented in Fig. 1.15. There are two layers of atoms in this figure. The atoms with solid outline are in the top plane while the atoms with dash line are in the bottom plane. In a perfect dislocation, the bottom layer atom moves from location A to location B. The perfect dislocation dissociates into a 90 ° and a 30 ° dislocation for a lower activation energy barrier. In this figure, the AC and CB shows the 90 ° and 30 ° partial dislocation, respectively.

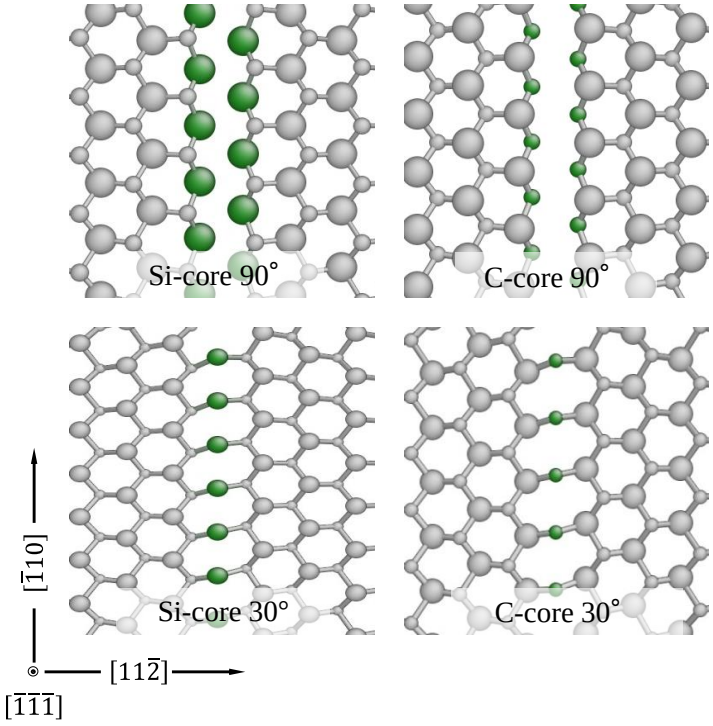

Figure 1.14 Four kinds of partial dislocations in 3C-SiC. The gray balls represent the silicon atoms have four-fold coordinates while the green balls have three-fold coordinates.

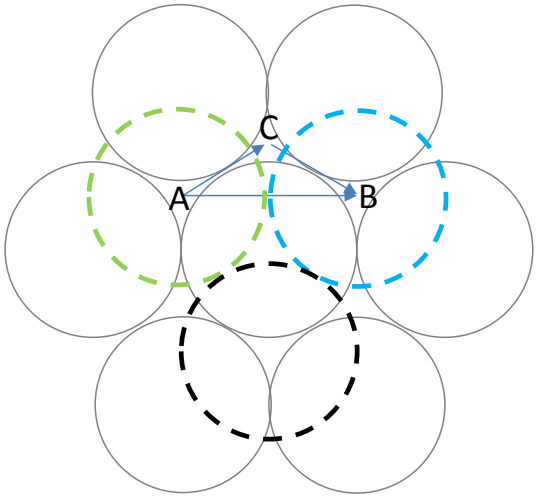

Figure 1.15 Schematic representation of dislocation dissociation.

Dislocations can be observed by experiment method like transmission electron microscope and large-angle convergent beam electron diffraction (Ning *et al*., 1996; Mussi *et al*., 2007, 2008; Long *et al*., 2013; Kiani *et al*., 2014), however, these previous experimental data about which partial dislocation has a higher mobility cannot consistent with each other. In addition, there is also a controversy between experimental results and the theoretical studies. Therefore, the reaction path way analysis is applied to solve this problem. More details are introduced in chapter 3.

1.2.3 Dislocation in silicon

Silicon as the second generation semiconductor material has attracted a lot of attention for decades (Seitz 1952; Hirth 1982; Rabier *et al*., 2010). It also has been considered as the one ideal test material for a better understanding the nature and properties of defects in semiconductor field because of its common crystal structure. (Cai *et al*., 2004; Rabier *et al*., 2010). The lattice structure of silicon is showed in Fig. 1.12 (a), which is similar to that of 3C-SiC. (b) shows the structure projection on plane (110). In this figure, the a, A, b, B, c, C represent different (111) planes, which is the closest packed plane that the dislocations are gliding on. In the dislocation motion, the dislocations glide by breaking the bond between the A and b, b and B are called shuffle-set dislocation and glide-set dislocation, respectively.

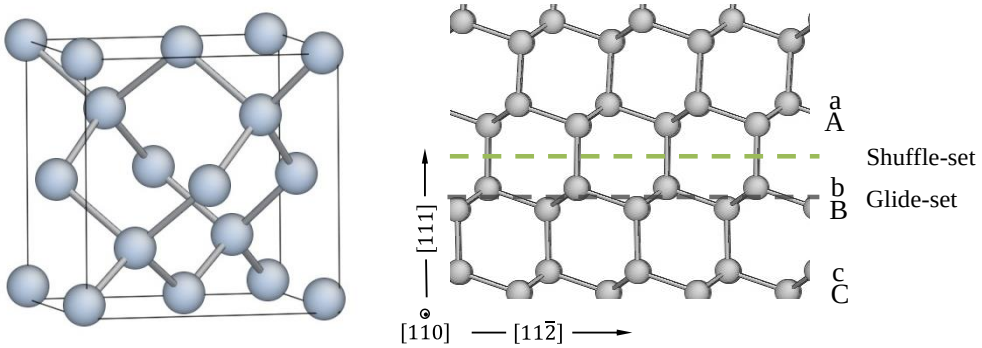

Figure 1.16 (a) Unit cell of Silicon. (b) Illustration of shuffle-set and glide-set dislocation in silicon.

For glide-set dislocations in silicon, the perfect dislocation dissociates into a 90 ° and a 30 ° dislocation (Raya and Cockaynea, 1970). The previous experiments and theoretical studies showed that glide-set dislocations move easily than shuffle-set dislocations in the region of high temperature and low stress (Gomez *et al*., 1975; Wessel and Alexander, 1977; Sato *et al*., 1980; Ren *et al*., 1995; Duesbery and Joos, 1996). In addition, by using electronic paramagnetic resonance which technique is sensitive to unpaired electrons, the experiment data showed that the number of unpaired atoms is less than 5% of the atom sites along the dislocation lines (Alexander 1965, 2013). That implied the partial dislocations in silicon are reconstructed. Therefore, the reconstructed partial dislocations were investigated. In 90 ° partial dislocation, the single period reconstruction and double period reconstruction could be coexist in the bulk with small energy differences. In 30 ° partial dislocation, serval reconstructed core structures had been proposed due to the unsymmetrical kink structure (Heggie 1983; Bennetto *et al*., 1997; Bulatov 1995; Cai *et al*., 2004).

After decades' studies, however, there are still something unclear about the mobility of the shuffle-set dislocation. Since 1996, Duesbery and Joos (1996) suggested that the shuffle-set dislocation may be more mobile than the glide dislocation at high stress and glide-set partial dislocation domain at low stress based on the energy calculation. More recently, the experiment data that came from Rabier and Demenet (2005) showed that shuffle-set and glide-set dislocations nucleated in different range of temperature and stress. On the other hands, Pizzagalli *et al*. (2008b, 2009a) proposed that the shuffle-set dislocation should be the most mobile one during the entire stress region by the theoretical studies of shuffle-set screw dislocations. This issue has lasted for years. More interestingly, a possible shuffle-glide transition mechanism was discussed by Rabier (2007). He found that the transition may be

involved with cross slip or climb. Moreover, Saka *et al*. (2006) observed that perfect dislocation transformed to dissociated dislocation in glide-set by testing the material with supersaturation of interstitials. Izumi *et al.* (2010) also observed a similar transformation in SiN film during the heating process. This transition mechanism is still unclear.

For theoretical studies, various methods had been applied in shuffle-set dislocation analysis including *ab initio* tight-binding, classical molecule dynamics and DFT. The screw dislocation core structures had been investigated by Wang *et al*. (2006) and Pizzagalli *et al*. (2009a, 2011). The activation energy of kink formation and migration were discussed by Pizzagalli *et al*. (2008b, 2011). Godet *et al*. (2004, 2006, 2009) performed dislocation nucleation from surface step by MD and first principles calculation. His simulation result showed that shuffle-set dislocation domain at low temperature and high stress, while the glide-set domain at high temperature and low stress. Izumi and Yip (2008) analyzed the shuffle-set dislocation loop nucleated from sharp corners. The dependence of activation energy barrier on stresses was obtained by reaction path way that based on NEB. They showed the resolved shear strain of shuffle-set dislocation nucleation is about 5%. Latter, Shima *et al*. (2010) proposed that the shuffle-set and glide-set dislocation domain on different stress regimes by performing the dependence of activation energy barrier on stress for both dislocations.

Based on above, we can see that the shuffle-set perfect dislocation motion in silicon is still unclear. And, none of the kink investigation for shuffle-set perfect dislocation has been reported yet. Therefore, the reaction path way analysis that based on NEB is performed to solve this problem. More details see chapter 4.

1.3 Problem statement

Dislocations which play an important role during the material plastic deformation have been studied for several decades. However, there are still some controversies between the experiment data and theoretical analysis. The willing of solving these interesting controversies is indeed one important motivation for the development of science.

This thesis has two major parts. The first part is aiming at figuring out the controversy between the experiment data and theoretical analysis about the partial dislocation motion in 3C-SiC. Another part is for filling the blank about the activation energy barriers during the shuffle-set perfect dislocation prorogation in silicon. In chapter 2, theories about classical molecule dynamics, NEB and energy minimization methods are stated and the empirical

potentials for silicon and 3C-SiC are introduced. In chapter 3, the activation energy barriers of partial dislocations nucleation and migration for both C-core and Si-core are calculated by NEB method with different driving shear stresses. The morphologies of partial dislocation lines and the stacking fault morphology are discussed. In chapter 4, the dislocation motion in two types of shuffle-set perfect dislocation core structures are investigated. At last, the conclusions and future work are presented in chapter 5.

Chapter 2

2 Theory

2.1 Introduction

A brief introduction of the related atomic simulation theory is presented in this chapter, including classical molecule dynamic simulation, NEB (nudged elastic method), energy minimization method and empirical potentials for SiC and silicon.

2.2 Classical molecule dynamics

Molecule dynamics simulation is used to represent the movement of atoms or molecules under different physical conditions. Potential functions are applied to define the interaction between the atoms or molecules. Besides, the interactive forces and the energy for each atoms or molecules can be calculated by the potential functions too. The trajectories of atoms and molecules are described by solving the Newton's equations of motion. In classical molecule dynamics, ions and electrons are considered as one entity. For N parts system, the atoms coordinates can be represented by a 3N-dimentsion vector. In Equation (2-1), the velocities of

atoms are obtained from the system temperature. The kinetic energy which is obtained from the atom weight and their velocities can be represented as a function of temperature. k_B is Boltzmann constant. The process of molecule dynamic simulation is showed in Fig. 2.1 as a flow chart. For simply, the whole process can be thought as calculate the physical properties for each steps until the set up steps is run out. When the simulation is finished, the output can be the physical properties of system and the atoms trajectories. The molecule dynamics simulation can also be performed in biology and chemistry for protein and chain molecule respectively.

$$\sum_{i=1}^{3N} \frac{1}{2} m_i v_i^2 = \frac{3N}{2} k_B T \tag{2-1}$$

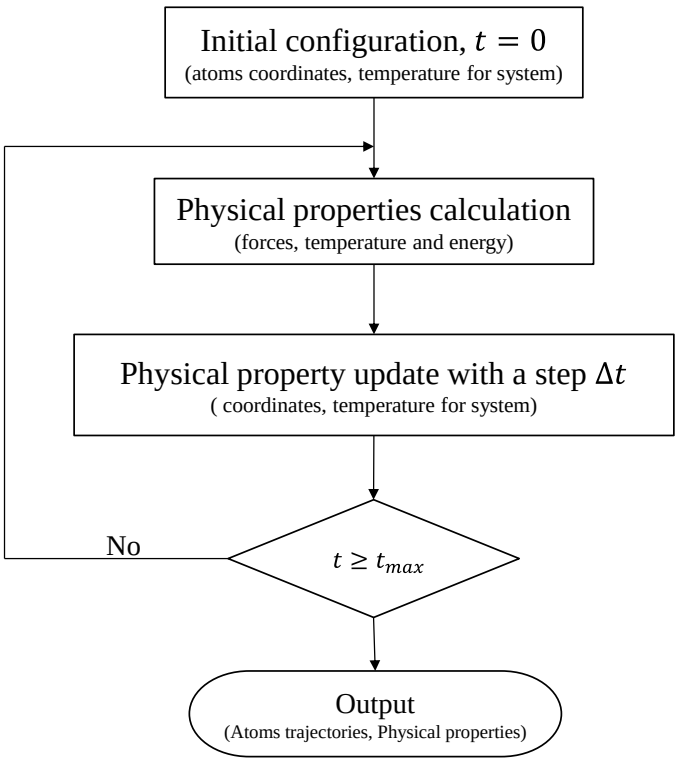

Figure 2.1 Flow chart of molecule dynamics simulation.

2.2.1 Periodical boundary condition

PBC (periodical boundary condition) is applied to eliminate the surface effects for the atoms are interacted in a small simulation box. In a finite simulation box, because of different coordination,

the atoms around the box boundary have less coordination numbers than the inside ones. During the simulation, the atoms interaction is performed by atom force which is influenced by coordination numbers of atom. Therefore, for simulating part of a large system, the PBC is applied to the unit box to insure the atoms in box have same surrounding atoms. As shown in Fig. 2.2, our simulation box is in the center with a blue circle. The other surrounding boxes are replicas of middle one, called images. When the atoms come out from the top of the box, the same numbers atoms come in from the bottom boundary of the box. The total number of the atom can be kept in constant by the setting. This setting is called periodical boundary condition. There is a limitation of this boundary condition setting, the box length must no smaller than twice of the cut-off distance. This limitation is used to avoid over calculating of the atom interaction force between the atom in the middle box and the some atom in the other boxes.

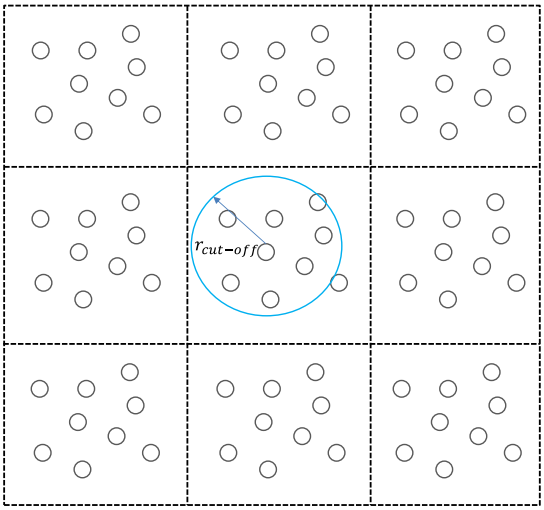

Figure 2.2 Schematic illustration of periodic boundary condition.

2.2.2 Newton's equation of motion

In MD simulation, the basic motion equation is Newton's equation as shown in Equation 2.2. The acceleration of each atom and the interaction force can been given by this equation. As a function of time, based on the initial positions and velocities of atoms, the system state can be predicted. Here, $\boldsymbol{F}_i$ $\boldsymbol{r}_i$ and m_i are the force vector, position vector and the mass of atom I, respectively.

$$\boldsymbol{F}_i = m_i \frac{d^2 \boldsymbol{r}_i}{dt^2} \tag{2-2}$$

The NVT ensemble is applied in our simulation. N is the number of atoms in our system

while V and T are the volume and temperature of system, respectively. The NVT ensemble means the three physical quantities are keeping as constants during the whole simulating process.

2.2.3 Dimensionless units

The dimensionless units, shown in Table.2-1, are used for no additional numerical factor during the molecule dynamics simulation. The quantity with star mark represents dimensionless unit. Table.2-2 expresses the basic physical parameter for our simulation.

Table 2-1 Dimensionless units forms

Physical quantity	Dimensionless forms
Time	$t^* = \frac{t}{d\sqrt{m_0/eV}}$
Mass	$r^* = \frac{m}{m_0}$
Length	$r^* = \frac{r}{d}$
Velocity	$v^* = \frac{v}{\sqrt{eV/m_0}}$
Force	$F^* = \frac{Fd}{eV}$
Acceleration	$a^* = \frac{adm_0}{eV}$
Temperature	$T^* = \frac{Tk_B}{eV}$
Stress	$\sigma^* = \frac{\sigma d^3}{eV}$
potential	$\Phi^* = \frac{\Phi}{eV}$

Table 2-2 Parameters for dimensionless units

Mass of silicon atom: m_{si}	$4.66434 \times 10^{-25}(kg)$
Mass of silicon atom: m_c	$1.99426 \times 10^{-25}(kg)$
Boltzmann constant: k_B	$1.38062 \times 10^{-23}(JK^{-1})$
Energy: eV	$1.60219 \times 10^{-19}(J)$
Length: Å	$1.00000 \times 10^{-10}(m)$

2.3 Energy minimization

In order to have a stable configuration of the transition state of atomic model, the energy minimization methods are applied after the initial artificial structure is created. These methods include conjugate gradient relaxation, steepest descent method and line minimization. Here, the local minimization method, conjugate gradient relaxation is applied to get the local minimization configuration while the NEB method is applied for the finding of saddle point configuration during the configuration transitions.

2.3.1 Conjugate gradient relaxation

CG (Conjugate gradient relaxation) is an efficient energy minimization method which has been widely used for finding the local minimum configurations. In this method, the calculation of Hessian is unnecessary that makes the calculation faster than others. The following are the details of this relaxation method. The Φ is the potential energy as a function of position x.

1. Set up the initial searching direction by $d_0 = -\nabla\Phi(x)$.
2. By Equation 2-3, minimize the energy though solving β.

$$\Phi(x_k + \beta \boldsymbol{d}_k) \leq \Phi(x_k) + v\beta\nabla\Phi(x_k)^T \boldsymbol{d}_k \tag{2-3}$$

3. Position updating

$$x_{k+1} = x_k + \beta_k \boldsymbol{d}_k \tag{2-4}$$

4. Searching direction updating by Equation 2-5.

$$\boldsymbol{d}_{k+1} = -\nabla\Phi(x_{k+1}) + \gamma_k \boldsymbol{d}_k$$

$$\gamma_k = \frac{\|\nabla\Phi(x_{k+1})\|}{\|\nabla\Phi(x_k)\|} \tag{2-5}$$

5. Next step by k=k+1.

By using CG method, the kink with different widths as local stable atomic configurations can be got. These configurations are the input of the NEB calculation for investigating the dislocation mobility in Silicon and 3C-SiC. The NEB method is introduced in next part.

2.3.2 Nudged elastic band method

NEB is theoretical method that widely used for minimum energy path way analysis. It can be applied to search the saddle point configuration which has the maximum energy in the MEP. During the NEB calculation, at first, the initial and final configurations are needed for input data. Serval replicas are given by linear interpolation between the initial and final configuration, these replicas are thought as connected by springs. The word Nudged means during the interaction between the replicas only the perpendicular component is considered for avoiding the influence from the true force. The following equations show the algorithm of NEB (Henkelman *et al.*, 2002). The chain of N replicas are defined by $[R_0, R_1, R_2, R_3 \cdots R_N]$, The parallel component of spring force for replica i is given by Equation 2-6. The $\dot{\tau}_i$ is the vector of band tangent of replica i which is shown in Equation 2-7. The Equation 2-6 can be rewritten as 2-8. The k is the spring constant for all springs that between the replicas.

$$\boldsymbol{F}^s_{i-para} = (\boldsymbol{F}^s_i \cdot \dot{\tau}_i)\dot{\tau}_i \tag{2-6}$$

$$\dot{\boldsymbol{\tau}}_{\boldsymbol{i}} = \frac{\tau_i}{|\tau_i|}$$

$$\tau_i = \frac{R_i - R_{i-1}}{|R_i - R_{i-1}|} + \frac{R_{i+1} - R_i}{|R_{i+1} - R_i|} \tag{2-7}$$

$$\boldsymbol{F}^s_{i-para} = (k[(R_{i+1} - R_i) - (R_i - R_{i-1})] \cdot \dot{\tau}_i)\dot{\tau}_i \tag{2-8}$$

For the total force is given by the summation of the spring force along the local tangent and the true force perpendicular to the local tangent in Equation 2-9. The true force perpendicular to the

local tangent is represented by $\nabla\Phi(R_i)_{perp}$. The Φ is the system energy. By the above equations, the MEP and the saddle point's configuration can be obtained when the perpendicular force on each replica is smaller than our setting value.

$$\boldsymbol{F}_i = \boldsymbol{F}^s_{i-para} - \nabla\Phi(R_i)_{perp} \tag{2-9}$$

2.4 Potential functions

Potential functions are used to describe the atomic interaction during the MD simulation. In this paper, the Vashishta potential is applied to represent 3C-SiC while the silicon has been investigated by EDIP, SW and Tersoff.

2.4.1 Stillinger Weber potential

The SW potential was proposed by Stillinger and Weber (1985), this potential was designed for described the interaction of silicon atoms. Fig .2.3 represents the atomic configuration of silicon in diamond and the physic quantities are marked in this figure. r_{ij} means the distant between the atom i and j, θ_{ijk} means the angle from atom j to k through i. Equation 2-10 shows the system energy E is composed by a two body part ϕ_2 and a three body part ϕ_3. ϕ_2 and ϕ_3 can be got from equation 2-10 and 2-11. The values of these parameters are shown in equation 2-12. More detail in reference Stillinger and Weber (1985).

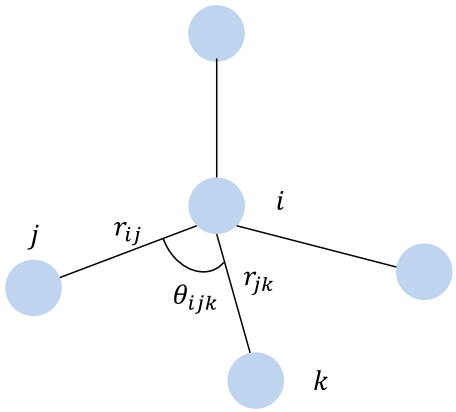

Figure 2.3 Atomic configuration of silicon.

$$E = \sum_i \sum_{j>i} \phi_2 (r_{ij}) + \sum_i \sum_{j \neq i} \sum_{k>j} \phi_3 (r_{ij}, r_{ik}, \theta_{ijk}) \tag{2-10}$$

$$\phi_2 (r_{ij}) = A_{ij} \varepsilon_{ij} \left[B_{ij} \left(\frac{\sigma_{ij}}{r_{ij}} \right)^{p_{ij}} - \left(\frac{\sigma_{ij}}{r_{ij}} \right)^{q_{ij}} \right] exp \left(\frac{\sigma_{ij}}{r_{ij} - a_{ij} \sigma_{ij}} \right) \tag{2-11}$$

$$\begin{aligned} \phi_3 (r_{ij}, r_{ik}, \theta_{ijk}) & \\ &= \lambda_{ijk} \varepsilon_{ijk} [\cos \theta_{ijk} \\ &\quad - \cos \theta_{0ijk}]^2 exp \left(\frac{r_{ij} \sigma_{ij}}{r_{ij} - a_{ij} \sigma_{ij}} \right) exp \left(\frac{r_{ik} \sigma_{ik}}{r_{ik} - a_{ik} \sigma_{ik}} \right) \end{aligned} \tag{2-12}$$

$$\begin{aligned} & A = 7.049556277, B = 0.6022245584, p = 4, q = 0, \\ & \mathrm{a} = 1.80, \lambda = 21.0, \gamma = 1.20 \end{aligned} \tag{2-13}$$

2.4.2 Tersoff potential

Tersoff (1988) designed an empirical interatomic potential for a better representation of the elastic properties for silicon. Similar to SW potential, the energy is represented as a function of atom coordinates. The physical quantities are the same as that of SW. There are several versions of Tersoff potential. In this work, the T3 version which has a better fitting of elastic properties is employed. Table 2-3 shows its parameters. Equation 2-14 to 2-18 show the how to get each value by initial input data such as atom coordinates etc. More details see references Tersoff (1988) and Plimpton (1995).

$$E = \sum_i \sum_{j \neq i} f_C (r_{ij}) [f_R (r_{ij}) + b_{ij} f_A (r_{ij})] \tag{2-14}$$

$$f_C = \begin{cases} 1 : r < R - D \\ \frac{1}{2} - \frac{1}{2}\sin\left(\frac{\pi}{2}\frac{r-R}{D}\right) : R - D < r < R + D \\ 0: \text{ r} > \text{R} + \text{D} \end{cases} \quad (2\text{-}15)$$

$$\begin{aligned} f_R(r) &= Ae^{-\lambda_1 r} \\ f_A(r) &= -Be^{-\lambda_2 r} \end{aligned} \quad (2\text{-}16)$$

$$\begin{aligned} b_{ij} &= (1 + \beta^n {\xi_{ij}}^n)^{-\frac{1}{2n}} \\ \xi_{ij} &= \sum_{k \neq i,j} f_C(r_{ik}) g(\theta_{ijk}) exp\left[{\lambda_3}^m (r_{ij} - r_{ik})^m\right] \end{aligned} \quad (2\text{-}17)$$

$$g(\theta) = r_{ijk}\left(1 + \frac{c^2}{d^2} - \frac{c^2}{[d^2 + (\cos\theta - \cos\theta_0)^2]}\right) \quad (2\text{-}18)$$

Table 2-3 Parameters Tersoff potential (Hara 2004, Li and Gao, 2013).

	Si(T3)
$A(eV)$	1.8308×10^3
$B(eV)$	4.7118×10^2
$\lambda_1(\text{Å}^{-1})$	2.4799
$\lambda_2(\text{Å}^{-1})$	1.7322
$\lambda_3(\text{Å}^{-1})$	1.7322
$R(\text{Å})$	2.85
$D(\text{Å})$	0.15
α	0.0
β	1.0999×10^{-6}
n	7.8734×10^{-1}
c	1.0039×10^5
d	1.6218×10^1
h	-5.9826×10^{-1}

2.4.3 Environment-dependent interatomic potential

Martin *et al*. (1997) developed the EIDP potential for better describing the phase and defects in bulk silicon. It includes two-body and three-body terms that depend on the atom environment. In our calculation for silicon, the EIDP potential is the major one for representing the kink structure well.

The following Equations tell us how to set the calculation in details.

$$E = \sum_{j \neq i} \phi_2 \left(R_{ij}, Z_i\right) + \sum_{j \neq i} \sum_{k \neq i, k > j} \phi_3 (R_{ij}, R_{ik}, Z_i) \tag{2-19}$$

$$\phi_2 (r, Z) = A \left[\left(\frac{B}{r}\right)^{\rho} - e^{-\beta Z^2} \right] exp\left(\frac{\sigma}{r - a}\right) \tag{2-20}$$

$$\phi_3 \left(R_{ij}, R_{ik}, Z_i\right) = exp\left(\frac{r}{R_{ij} - a}\right) exp\left(\frac{r}{R_{ik} - a}\right) h(cos\theta_{ijk}, Z_i) \tag{2-21}$$

$$\begin{aligned} Z_i &= \sum_{m \neq i} f\left(R_{im}\right) \\ f(r) &= \begin{cases} 1 : r < c \\ \exp(\frac{\alpha}{1 - x^{-3}}) : c < r < a \\ 0 : r > a \end{cases} \end{aligned} \tag{2-22}$$

$$\begin{aligned} h(l, Z) &= \lambda \left[\left(1 - e^{-Q(Z)(l + \tau(z))^2}\right) + \eta Q(Z)(l + \tau(Z))^2 \right] \\ Q(Z) &= Q_0 e^{-\mu Z} \quad \tau(Z) = \mu_1 + \mu_2 (\mu_3 e^{-u_4 Z} - e^{-2u_4 Z}) \end{aligned} \tag{2-23}$$

2.4.4 Vashishta potential

In our paper, the simulation of 3C-SiC is performed by Vashishta potential. Vashishta potential (Vashishta *et al.*, 2007) is an effective interatomic interaction potential for SiC that consists of two-body and three body parts. Fig. 2.4 shows the quantities of the SiC with atomic configuration.

The system energy is given by Equation 2-24. The two body part and the three body part are shown in Equation 2-25 and 2-26, respectively. H_{ij} is the strength of the steric repulsion, Z_i is the effective charge, D_{ij} the strength if charge-dipole attraction and W_{ij} represents the Van der Waals interaction. λ and ε are screening length for coulomb and charge-dipole terms, respectively (Vashishta *et al.*, 2007). In addition, the three body part in this potential is a kind of modification of the SW form. During the atomic simulation in lammps (Plimpton, 1995), we can apply this potential by changing some parameters with a SW form. Vashishta potential is used in our simulation because of its good representation of 3C-SiC. The physical quantities

comparison is shown in Table 2-4, the simulation output has a good agreement with the experiment data.

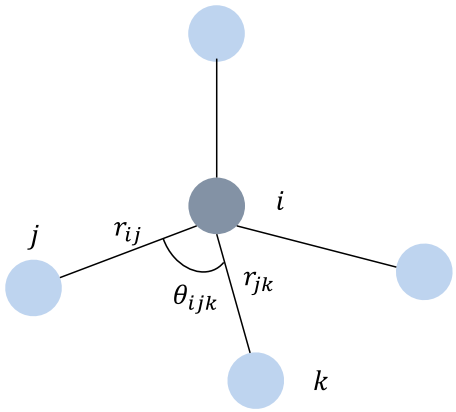

Figure 2.4 The structure of silicon carbide. The middle one represents silicon atom, when the others represent carbon atoms.

$$V = \sum_{i<j} V_{ij}^{(2)}\left(r_{ij}\right) + \sum_{i,j<k} V_{jik}^{(3)}(r_{ij}, r_{ik}) \tag{2-24}$$

$$V_{ij}^{(2)}(r) = \frac{H_{ij}}{r^{\eta_{ij}}} + \frac{Z_i Z_j}{r} e^{-r/\lambda} - \frac{D_{ij}}{2r^4} e^{-r/\varepsilon} - \frac{W_{ij}}{r^6} \tag{2-25}$$

$$V_{ijk}^{(3)}(r_{ij}, r_{ik}) = R^{(3)}(r_{ij}, r_{ik}) P^{(3)}(\theta_{ijk}) \tag{2-26}$$

$$R^{(3)}\left(r_{ij}, r_{ik}\right) = B_{jik} \exp\left(\frac{r}{r_{ij} - r_0} + \frac{r}{r_{ik} - r_0}\right) \Theta(r_0 - r_{ij}) \Theta(r_0 - r_{ik}) \tag{2-27}$$

$$P^{(3)}\left(\theta_{jik}\right) = \frac{(\cos\theta_{jik} - \cos\bar{\theta}_{jik})^2}{1 + C_{jik}(\cos\theta_{jik} - \cos\bar{\theta}_{jik})^2} \tag{2-28}$$

Table 2-4 Material property comparison between experiment and MD simulation with Vashishta potential. The data comes from following references (Vashishta 2007; Harrison 1980; Ioffe Institute 2003; Carnahan and Ceram 1968; Feldman *et al*., 1968).

	Experiment	MD
Lattice constant (Å)	4.3596	4.3581
Cohesive energy (eV)	6.34	6.3410868
Melting Temperature (K)	3103 ± 40	3250 ± 50
C_{11}	390	390.0
C_{12}	142	142.6
Bulk modulus (Gpa)	225-270	225.2

2.5 Stress application

During the dislocation mobility analysis, the dependences of activation energy barriers for kink nucleation and migration on driving stress are calculated. For applying the stress, the Parrinello and Rahman (1980, 1981) method are used by shaping the simulation box which is shown in Fig. 2.5. a b c are the sides vectors of the box. The positions of atoms in the box can be given by Equation 2-29. ρ is defined from 0 to 1.

$$r_i^a = a_i\rho_1^a + b_i\rho_2^a + c_i\rho_3^a \tag{2-29}$$

The shape matrix of simulation box is defined by Equation 2-30. For the initial box without deformation, only the diagonal elements are no-zero. The atom positions can be written as $\boldsymbol{r}_0^a = \boldsymbol{h}_0\rho_0^a$. After the deformation of the box, the shape matrix is changed in to $\boldsymbol{h}$. Therefore, the atom positions with new side vectors are given by $\boldsymbol{r}^a = \boldsymbol{h}\boldsymbol{h}_0^{-1}\,\boldsymbol{r}_0^a$. With these new atom coordinates, the stain can be applied to the model appropriately.

$$h = \begin{pmatrix} a_x & b_x & c_x \\ a_y & b_y & c_y \\ a_z & b_z & c_z \end{pmatrix} = \begin{pmatrix} h_{11} & h_{12} & h_{13} \\ h_{21} & h_{22} & h_{23} \\ h_{31} & h_{32} & h_{33} \end{pmatrix} \tag{2-26}$$

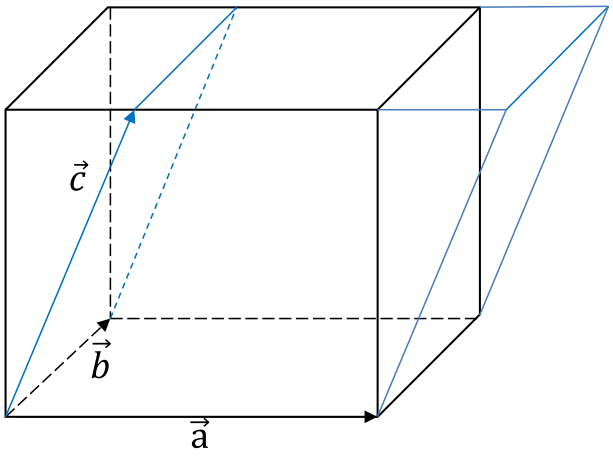

Figure 2.5 Unit cell and sides vectors.

2.6 Peach-koehler force

Peach-koehler force (Peach and koehles, 1950) is used to present the force that applied on the dislocation loop. As shown in Equation 2-30, the Peach-koehler force is given as the function of the burgers vector. The driving force of the dislocation $\boldsymbol{F}_p$ is defined by Equation 2-31, as the component along the $\mathbf{p}$ direction. Moreover, the driving stress per unit of the dislocation line in our thesis is written as Equation 2-32.

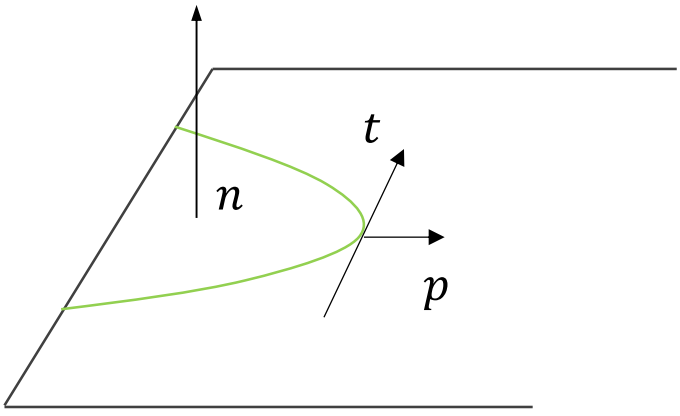

Figure 2.6 Dislocation loop

$$\boldsymbol{F} = (\boldsymbol{\sigma} \cdot \mathbf{b}) \times \mathbf{t} \tag{2-30}$$

$$\boldsymbol{F}_p = \boldsymbol{F} \cdot \mathbf{p} \tag{2-31}$$

$$\boldsymbol{\tau}_p = \boldsymbol{F}/|\boldsymbol{b}| \tag{2-32}$$

Chapter 3

3 Reaction path way analysis for partial dislocation in 3C-SiC

3.1 Introduction

3C-SiC can be grown in larger diameter of wafer than other polytypes for its' lower formation temperature. This makes lower cost in the semiconductor device manufacturing. As we mentioned in chapter 1.2.1, there is a controversy about which kind of partial dislocations move easier. For solving this controversy, the reaction pathway analysis is applied for partial dislocation nucleation and migration.

For theoretical analysis, few studies have been reported on the partial dislocations mobility in 3C-SiC. In 2003, Blumenau *et al.* (2003) pointed out that the core energies for different polytypes are quite similar by comparing the energy factor in 2H-SiC and 3C-SiC. This result implied that the kink migration and nucleation activation energies are nearly the same for most polytypes of silicon carbide with the assumption that the kink motion processes are the same. In

addition, forcing on the reconstructed dislocation structure, the kink formation and migration energies had been investigated by DFTB calculation with around 5000 atoms. The simulation data showed that the 90 °partial dislocation has a lower activation energy barrier than 30 °partial dislocation. And the obstacles in the material such as the carbon atom site occupied by nitrogen may play an important role during the dislocation motions. He also pointed out that only the Si-core partial dislocations are electrical active. Later, Savini *et al*. (2006, 2007) analyzed the partial dislocation motions by first-principle calculation. He forced on the asymmetric (AR) and symmetric structures (SR) which are called as reconstructed and unreconstructed structures in the reference by Blumenau *et al.* (2003), respectively. In this study, both the AR and SR dislocation were investigated with about 300 atoms. For AR dislocation, the activation energies of kink formation and migration of first-principle simulation were lower than that of DFTB. But they still got the same conclusion about that the C-core partial dislocation has lower activation energy barrier than Si-core partial dislocation. Moreover, Savini *et al*. (2007) pointed out that all the dislocations with SR have lower activation barrier than that those of AR and the 90° partial dislocations have lower barrier than 30° partial dislocations. More recently, Sun *et al.* (2013) investigated the 90° partial glide-set dislocation loop nucleation from sharp corners by empirical potential function, their simulation results showed that the Si-core dislocation has lower activation energy that agrees with the previously-mentioned experimental data.

For experiment observation, which kind of partial dislocation moves easier and has a higher mobility can be observed directly. Ning *et al*. (1996) observed that the Si-core partial dislocation was the leading partial dislocation in 3C-SiC TEM observation above 1300 ℃. Still by TEM observation, Ha *et al*. (2003) showed that the Si-core 30° partial dislocation was moving while the C-core dislocation is immobile in 4H-SiC. They indicated that under the forward bias, the Si-core 30 °partial dislocation can emit light for the electron-hole recombination while the C-core 30 °partial cannot emit light. Latter, Idrissi *et al*. (2007) and Lancin *et al*. (2009) observed the similar phenomenon that both of the C-core and Si-core partial dislocations can be nucleated, and the C-core partial dislocation was immobile after the Si-core partial dislocation had moved a long distance. The experimental data provided by Lara (2012) showed that most of the basal dislocations dissociated into partial dislocations under the temperature that higher than Tc~993 ℃. These partial dislocations moved simultaneously while the Si-core partial dislocations moved as the leading one and the C-core partial dislocations were trailing. All of

these experimental data showed that the Si-core partial dislocation moves easier than the C-core partial dislocation.

Thanks to Hirth and Lothe (1982), the empirical function shown in Equation 3-1 helped us build a connection between the activation energy barriers and the dislocation mobility. A higher activation energy barrier means lower dislocation mobility. In the equation, Q is given by $Q = 2F_k + w_m$ for short dislocation segments, and $F_k + w_m$ for long segments. Here, F_k represents the activation energy barrier of the kink nucleation while w_m represents the activation energy barrier of the kink migration.

$$v_{dis} \propto e^{-Q/kT} \tag{3-1}$$

Based on the above, the controversy about the partial dislocation mobility in 3C-SiC is raised. For the experimental results, there is a widely accept that the Si-core partial dislocation has a higher mobility than C-core partial dislocation. However, this conclusion is in contrast with the previous theoretical analysis (Blumenau *et al.,* 2003; Savini *et al.,* 2007) that the C-core partial dislocation has lower activation energy barrier than Si-core partial dislocation. This contradiction may be caused if these atomic models in those theoretical analyses represent the 3C-SiC well. Besides, more atoms should be employed in the simulation. Therefore, by using empirical potential the reaction pathway analysis is performed for solving this controversy about the partial dislocation mobility in 3C-SiC.

3.2 Atomic model

The simulation model is schematically shown in Fig. 3.1. The coordinate axes are [11-2], [-110], [111] for X, Y, Z directions, respectively. The model size is 9.60×22.2×2.26nm^3, including 46,656 atoms. The dislocation line is on the slip plane (111), and the burgers vectors are $b_{90} = a_0[11\bar{2}]/6$ and $b_{30} = a_0[1\bar{2}1]/6$ for 30 °and 90 °partial dislocations. The shear stress σ_{xz} was applied by displacing top and bottom atoms along the x and –x directions. Periodical boundary condition is applied in Y direction. Vashishta potential function was used to represent the 3C-SiC, which can reproduces the stacking fault energy calculated by DFT (Shimojo *et al.*, 2001). Therefore, with the combination of molecular dynamics and conjugate gradient method, several stable configurations of 30 ° and 90 ° partial dislocations with different widths of kink were obtained. Based on these configurations, I performed reaction pathway analysis (Izumi and

Yip 2008; Shima *et al.*, 2010) based on CI-NEB method to identify the activation energy barriers of kink nucleation and migration for these different kinds of dislocations.

One of our difficult points during the simulation is the structure modelling. Since the kink structures are artificially created based on the dislocation theory, the relaxation process with NVT ensemble are needed; which make the artificial kink structure more close to the real one. The problem appeared in the relaxation process. Due to the large stress which is caused by the artificial model, sometimes, the kink changes its width of position. Therefore, for obtaining our target configuration with a series of continues stress or strain, hundreds of tests had been tried.

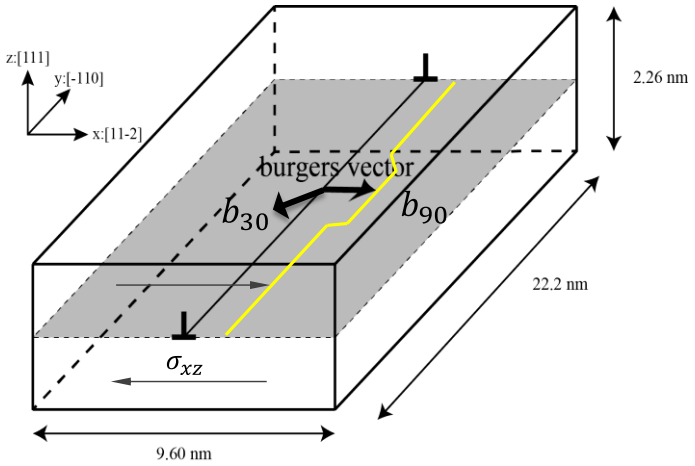

Figure 3.1 Schematic representation of the simulation model. The thin yellow line represents the location of the kink.

Fig. 3.2 shows the dislocation core structure's projection onto (111) and (110) planes with different direction of Si-core and C-core respectively. Along the dislocation line, two layers of atoms shown by green balls represent the atom with three-fold coordination while the other atoms have four-fold coordination. The larger atom represents silicon, the smaller one represents carbon. All these dislocations are unreconstructed structures that which are the same with the SR structures (Savini *et al.*, 2007a, 2007b). The reason I chose the unreconstructed configuration as the simulation model is because of that the model with reconstructed dislocation lines of Blumenau *et al.* (2003) failed to explain the electrical activity of both 30° partial dislocations. Savini, *et al*. (2007a, 2007b) proposed that the unreconstructed dislocation types, mentioned as SR in their paper, have a higher mobility and stability in heavily N-doped materials (Lacin *et al.*, 2009). Moreover, these unconstructed models are considered as one major explanation of the electrical activity for both 30° partial dislocations.

Atomeye (Li, 2003) is used to visualize the structure configuration, and the average Si-C

bond length is around 1.86 Å. Moreover, 2.16 Å is set up to decide whether the Si-C bond will be shown in the visualization. The dislocation structure characters are also shown in Fig. 2. For 90 ° partial dislocation structure, with 0.3 GPa driving shear stress, the dangling bond atoms along the dislocation line area are separated by 2.50 Å for C-core, and 2.28 Å for Si-core under 0.3 GPa driving shear stress. For 30 °partial dislocation, the distance between the dangling bond atoms along the dislocation line is 3.18 Å for Si-core and 3.31 Å for C-core under 1.8 GPa. All of these distances between the dangling bond atoms along the dislocation line are shown in Fig. 2 by dash yellow lines.

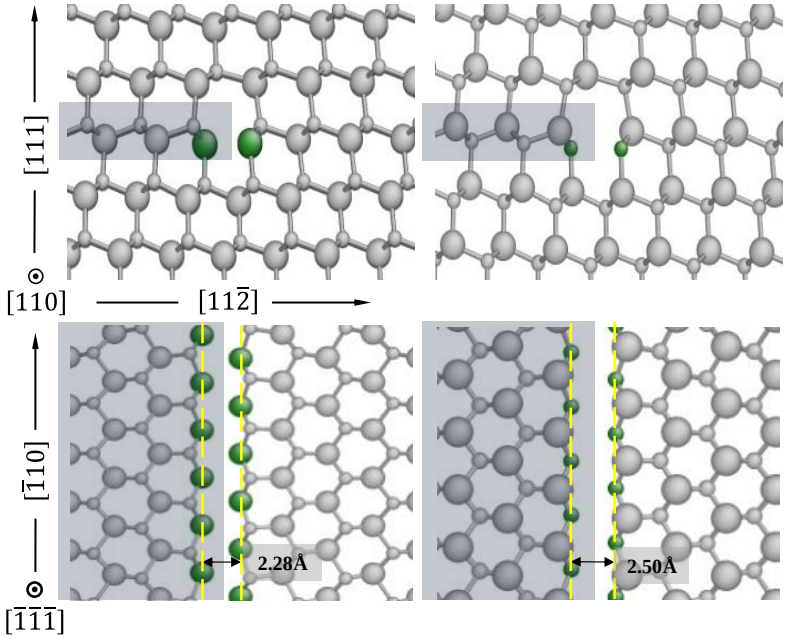

(a) 90 °Partial dislocation Si-core. (b) 90 °Partial dislocation C-core.

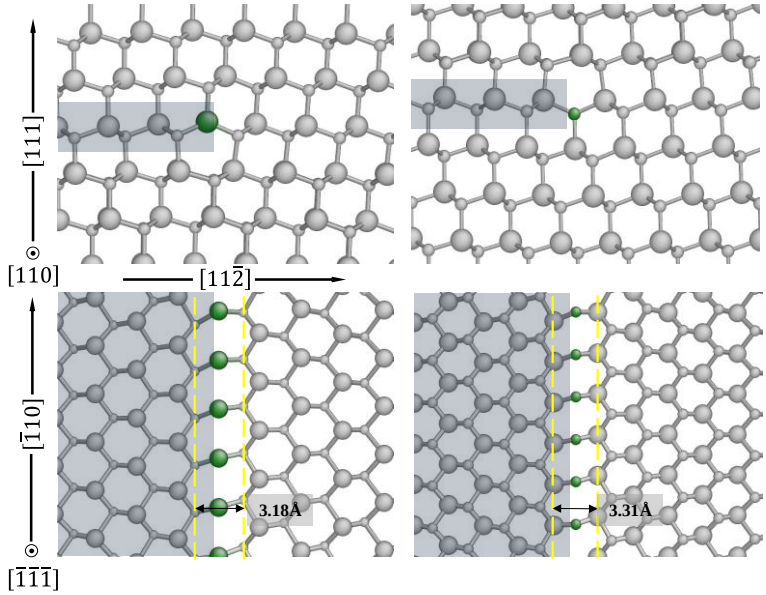

(c) 30 °Partial dislocation Si-core. (d) 30 °Partial dislocation C-core.

Figure 3.2 The relaxed core structure of the Shockley partial dislocation in {111} plane of 3C-SiC. The larger atoms represent silicon while the smaller ones represent carbon. For each partial dislocation, the upper Fig. shows a projection along the dislocation line while the bottom Fig. shows the projection onto (111) glide plane with the $[\mathbf{1\bar{1}0}]$ dislocation line vertical in the Fig. (a), (b) show the 90 ° partial dislocation core structure of Si-core and C-core respectively. (c), (d) show the 30 ° partial dislocation core structures of Si-core and C-core respectively. The stacking fault area is shown by shadow area. The dash yellow lines show the distance between the dangling bond atoms along the dislocation line.

3.3 Simulation results and discussion

3.3.1 90 °partial dislocation

In 90° partial dislocation, the kink nucleation and kink migration were analyzed for both C-core and Si-core. Fig. 3.3 shows the minimum energy pathway and the atomic configurations along the path. The atom marked by the small black arrow is moving along the burgers vector direction in that process which help us understand how does the atom move to accomplish the nucleation. Fig. 3.4 shows kink nucleation paths for C-core and Si-core. The kink pair of width 12 is shown in Fig. 3.5. The width is counted by the number of dangling bond atoms along dislocation line between the positive and negative kinks. In Si-core partial dislocation, during the kink migration, the carbon atom marked with small black arrow moves to elongate kink width, while the silicon atom moves in the C-core partial dislocation. The dependence of

activation energy on the driving shear stress was summarized in Fig. 3.6. Part of 90° partial dislocation calculation data comes from the master thesis by Muranaka *et al*. (2013).

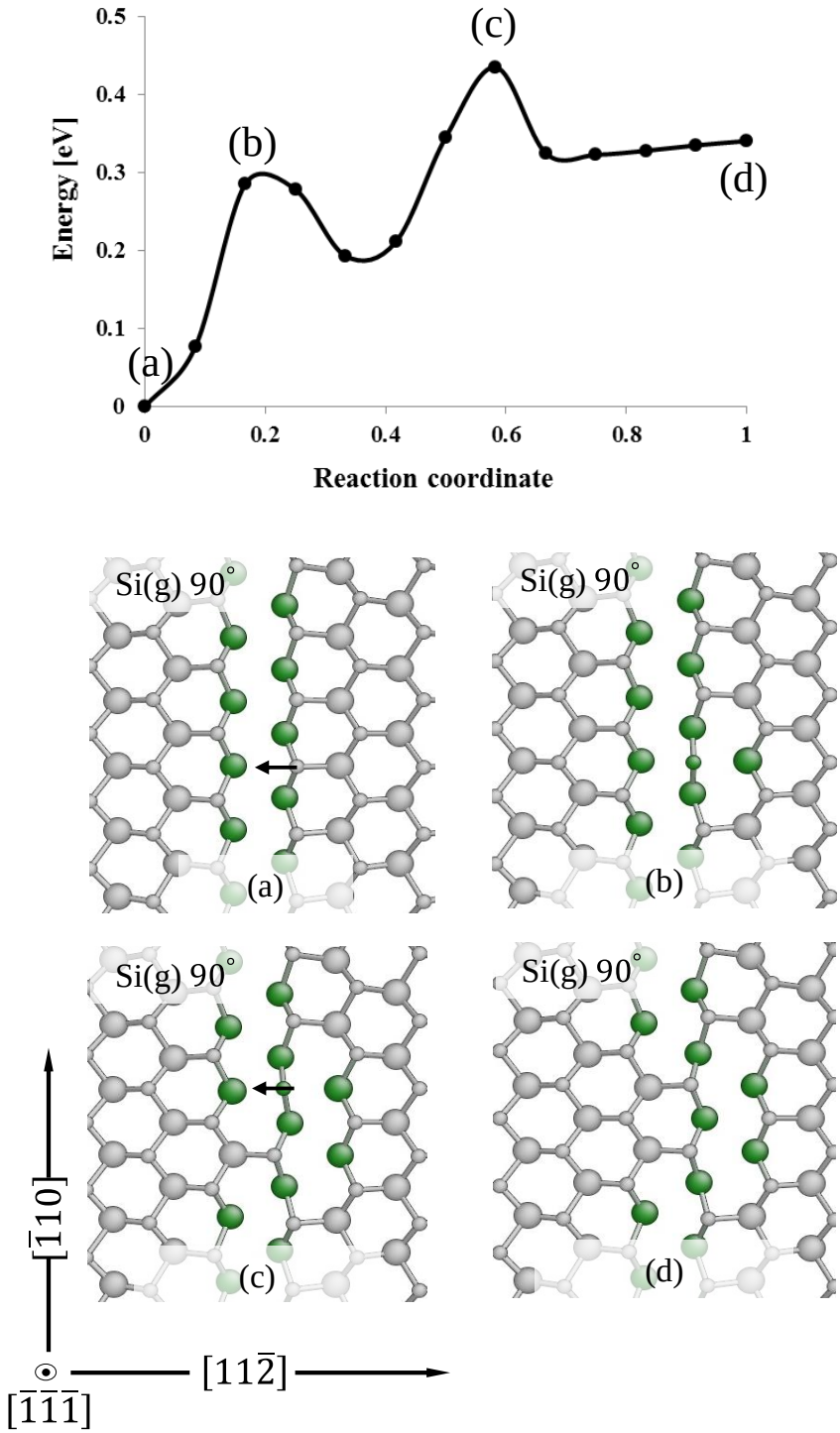

Figure 3.3 Minimum energy pathway of the Si-core 90° partial dislocation kink nucleation.

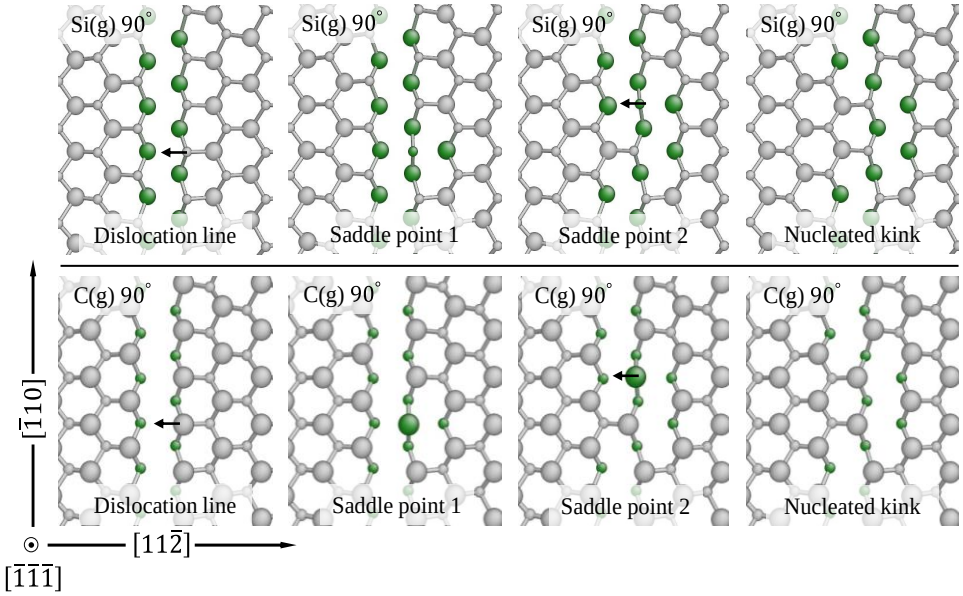

Figure 3.4 Kink migration path for 90 °partial dislocation of C-core and Si-core. The first row shows kink migration path of the Si-core glide set 90 °partial dislocation. The second row shows kink migration path of the C-core glide set 90 °partial dislocation. The small black arrow shows the atom moving direction during the reaction path way of kink migration period.

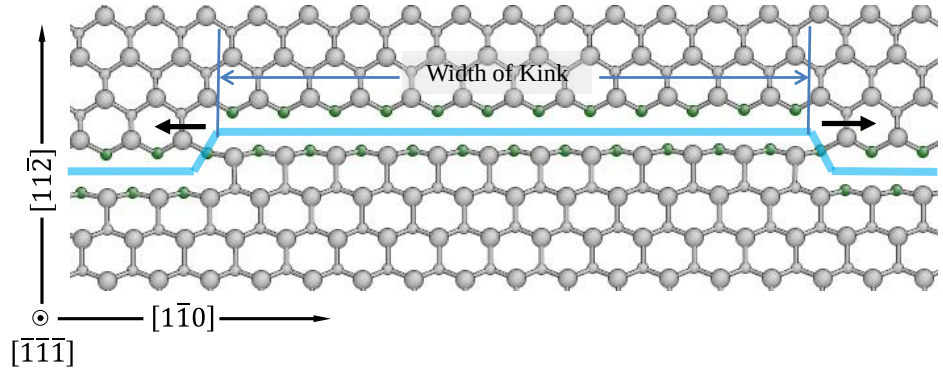

Figure 3.5 Kink pair structure for C-core 90 °partial dislocation with a width of 12. The width is measured by the number of dangling bond atoms along the kink. The black arrows show the direction of kink migration. The kink pair width increases after the kink migration.

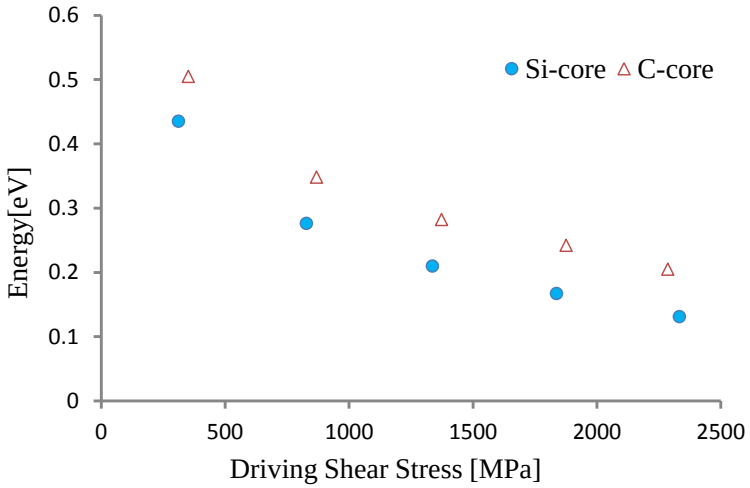

Figure 3.6 Dependence of activation energy on driving shear stress for Si-core and C-core 90° partial dislocation kink migration.

These results show that the C-core has a higher activation energy barrier. In addition, the activation energy difference of kink migration is 0.15±0.03eV between the two types 90°partial dislocations under different driving shear stresses. However, the previous simulation given by Blumenau *et al*. (2002, 2003) with DFTB and Savini *et al*. (2007a, 2007b) with first principle calculation showed that C-core has lower activation energy barrier in 90° partial dislocation. This difference between our study and previous numerical ones are caused by the different atomic models. As shown in Fig. 3.7, in the DFTB and first principle calculation, only the atoms on the slip plane are modeled, which is part of the deformed region that caused by the dislocation. The MD model is much larger with more atoms and more close to the real structure.

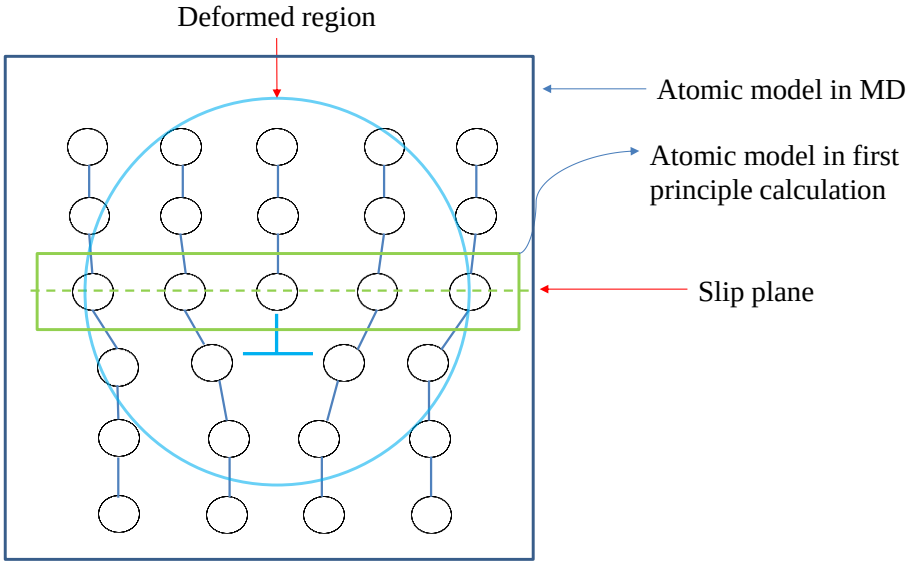

Figure 3.7 Atomic model in the MD and First principle calculation.

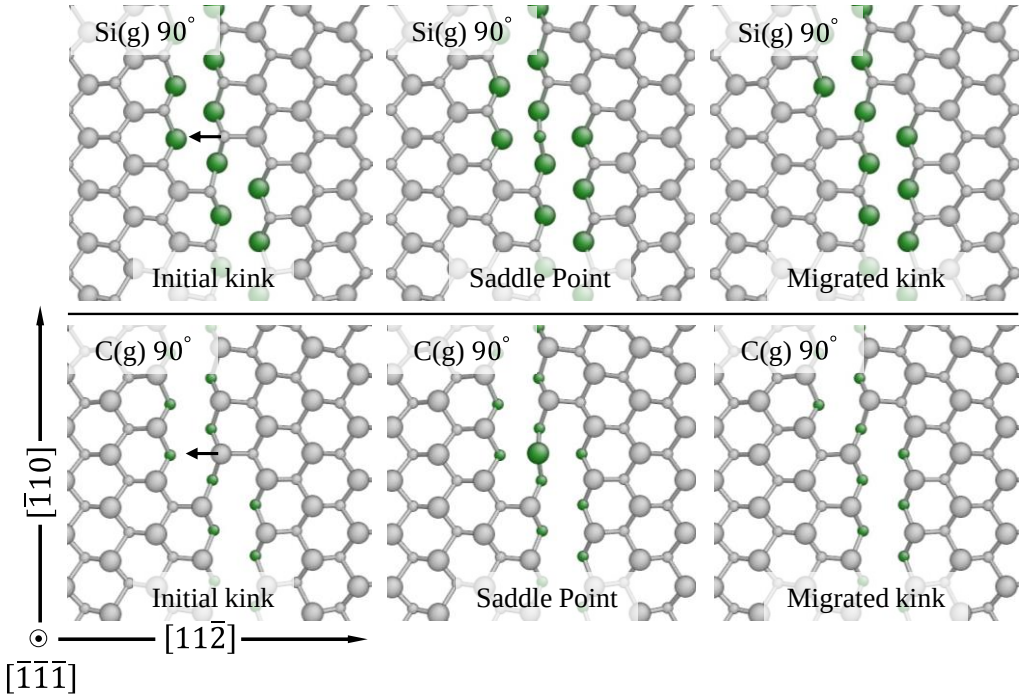

Figure 3.8 Kink nucleation path for C-core and Si-core 90 °partial dislocation. The first row shows kink nucleation path of the Si-core glide set 90 °partial dislocation. The second row shows kink nucleation path of the C-core glide set 90 °partial dislocation. During the kink nucleation path, the two atoms, marked by black arrows, move in sequence to complete the kink nucleation process. During the first atom is moving, the second atom almost doesn't move.

The kink migration path of 90° partial dislocation is shown in Fig. 3.8, while the kink nucleation activation energy as a function of driving shear stress is summarized in Fig. 3.9. These results indicate that the Si-core 90° partial dislocation has a lower activation energy barrier than C-core 90 °partial dislocation. This conclusion is also consistent with experimental data (Lara *et al*., 2012) that, above the critical temperature, the C-core and the Si-core partial dislocation glide simultaneously with a small separation between them, and Si-core partial dislocation is the leading partial dislocation. What's more, based on the reaction path way analysis in Fig. 3.8, we can see that the atom marked with a small black arrow moves, breaks one Si-C bond and forms a new one during kink migration. Simultaneously, two atom marked by black arrow move in sequence during kink nucleation. The motion of atoms around the kink during kink nucleation and kink migration are quite similar. The similarity of these processes implies that the C-core 90 °partial dislocation has lower activation energy for both nucleation and migration as compared to the Si-core 90 ° partial dislocation. In other words, it is not

possible that the C-core partial dislocation can have a higher activation energy for nucleation but a lower activation energy for migration compared to those for the Si-core partial dislocation. In addition, considering with characteristic of the dislocation core structure, shown in Fig. 3.2, the partial dislocation with a larger separation between the dangling bond atoms along the dislocation line also has higher activation energy. This consistence may suggest that based on characteristic of dislocation core structure, we can predict which kind of 90° partial dislocations has a lower activation energy barrier. Nonetheless, this hypothesis should be based on that the empirical potential which was carried out in the simulation can represent SiC well.

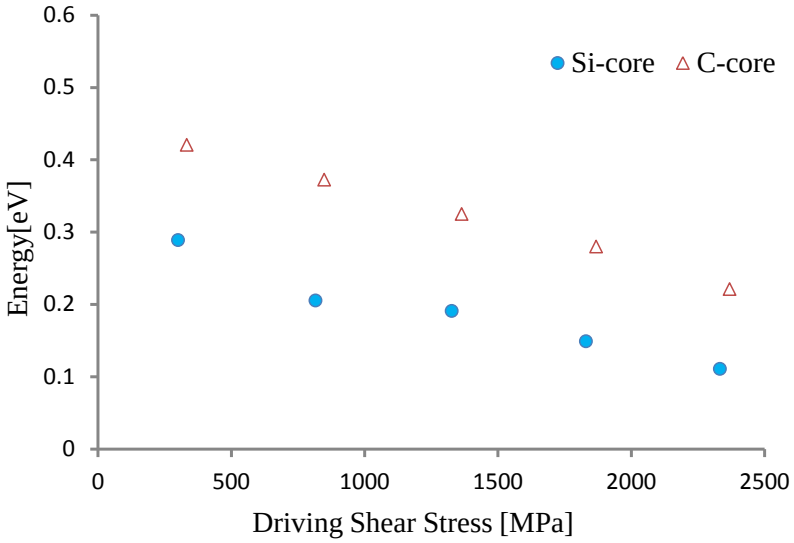

Figure 3.9 Dependence of activation energy on driving shear stress for Si-core and C-core 90 °partial dislocation kink nucleation.

3.3.2 30 °partial dislocation

For the unsymmetrical kink structure of 30 ° partial dislocation, there are two different activation energy barriers for the left and right kink (LK and RK) respectively. Their activation energy difference is caused by structure difference of RK and LK. The minimum energy paths for the LK and RK migration are shown from Fig. 3.10 to Fig. 3.31. The horizontal axis is the coordination and the perpendicular axis is the activation energy. The peak in the curve presents the activation energy barrier of the migration process.

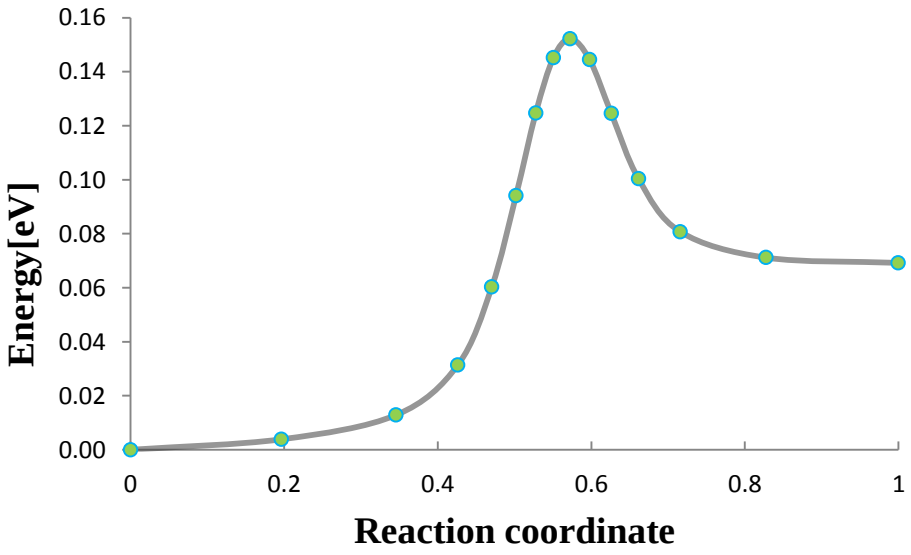

Figure 3.10 Minimum energy path for RK migration of Si-core 30 ° partial dislocation driving stress 1470 MPa.

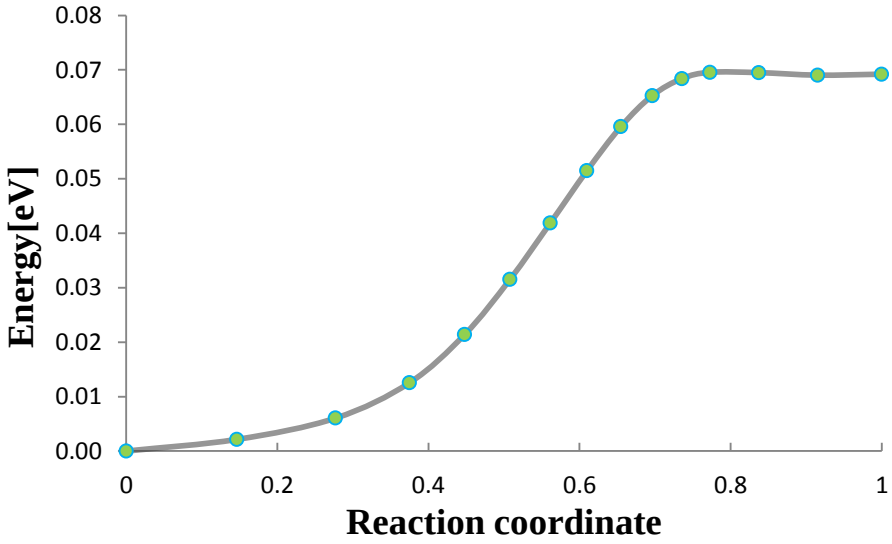

Figure 3.11 Minimum energy path for LK migration of Si-core 30 ° partial dislocation driving stress 1470 MPa.

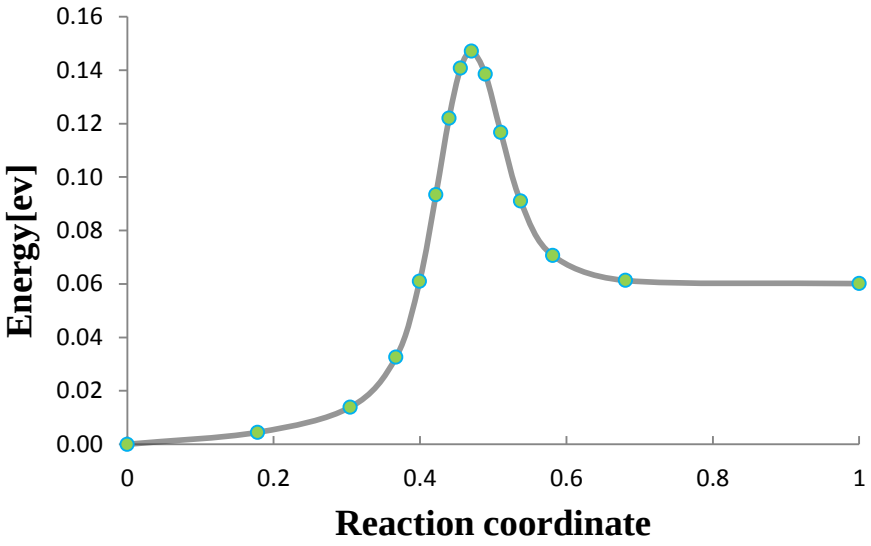

Figure 3.12 Minimum energy path for RK migration of Si-core 30 ° partial dislocation driving stress 1610 MPa.

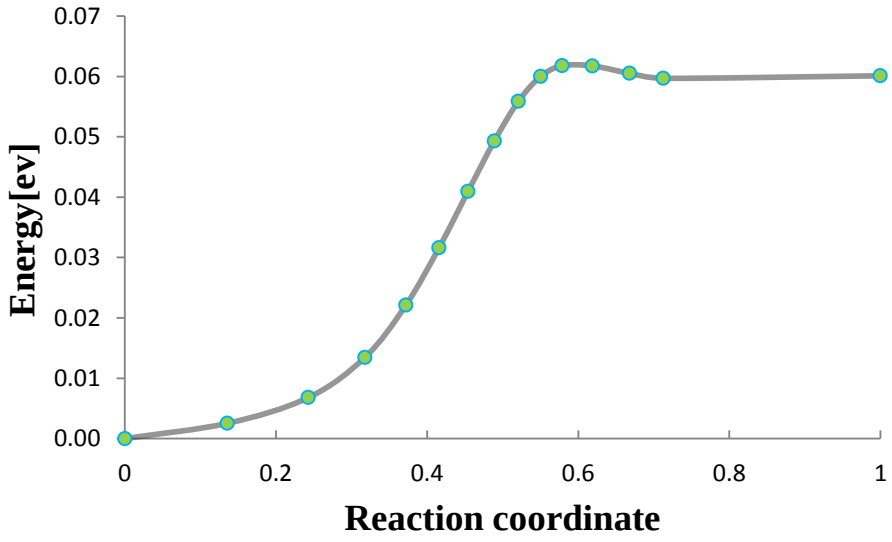

Figure 3.13 Minimum energy path for LK migration of Si-core 30 ° partial dislocation driving stress 1610 MPa.

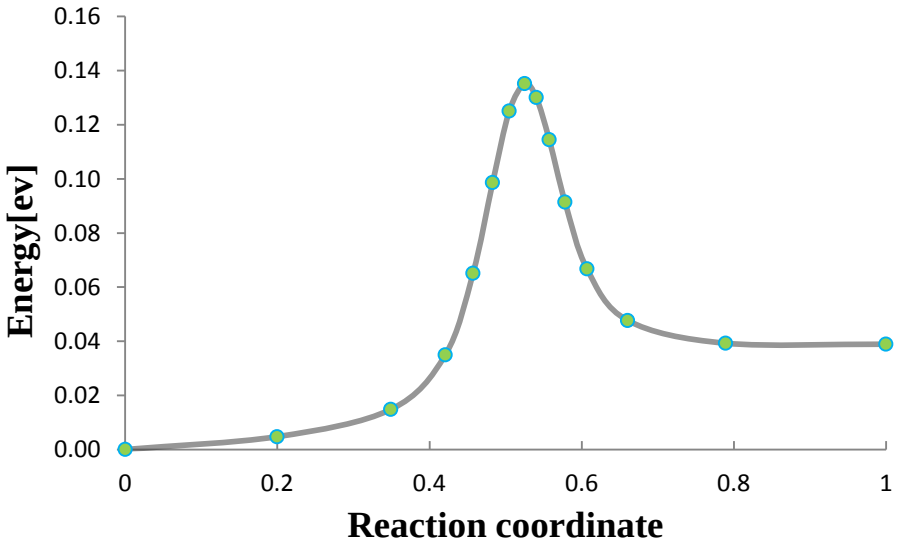

Figure 3.14 Minimum energy path for RK migration of Si-core 30 ° partial dislocation driving stress 1817 MPa.

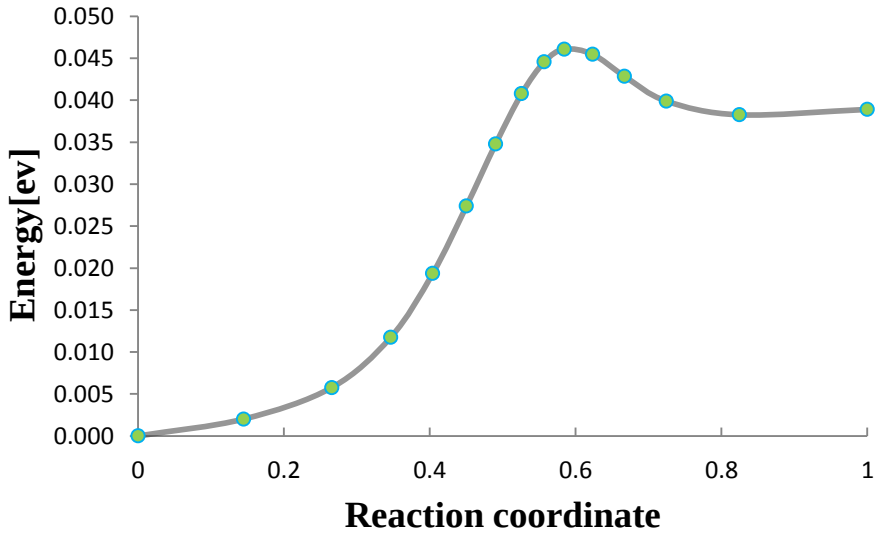

Figure 3.15 Minimum energy path for LK migration of Si-core 30 ° partial dislocation driving stress 1817 MPa.

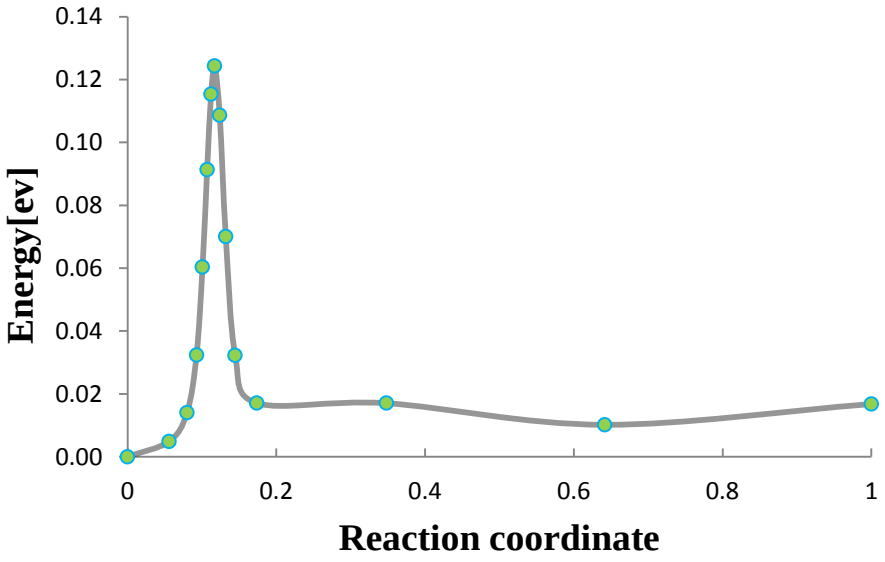

Figure 3.16 Minimum energy path for RK migration of Si-core 30 ° partial dislocation driving stress 2022 MPa.

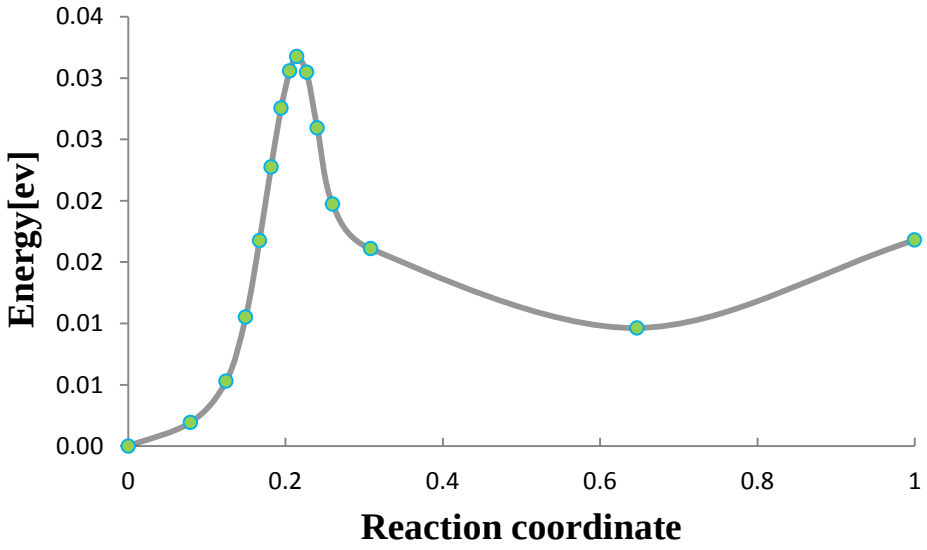

Figure 3.17 Minimum energy path for LK migration of Si-core 30 ° partial dislocation driving stress 2022 MPa.

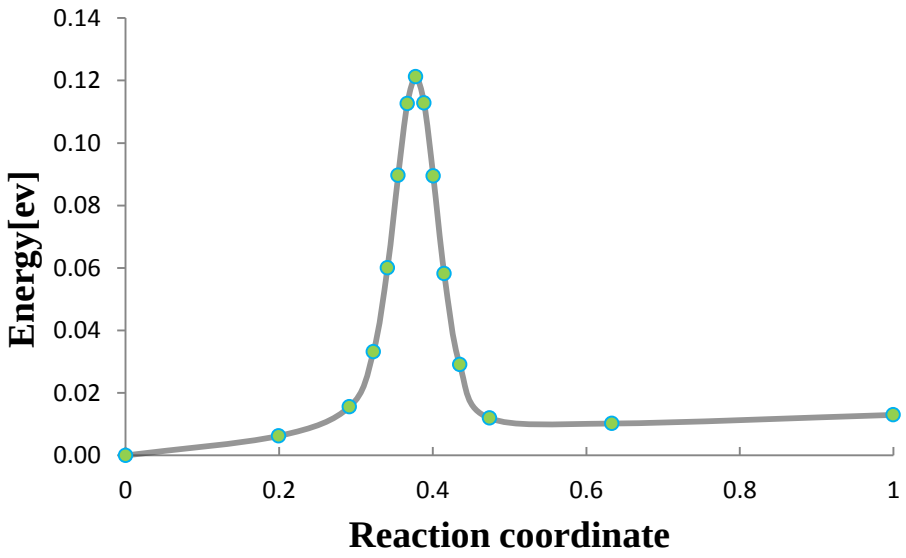

Figure 3.18 Minimum energy path for RK migration of Si-core 30 ° partial dislocation driving stress 2086 MPa.

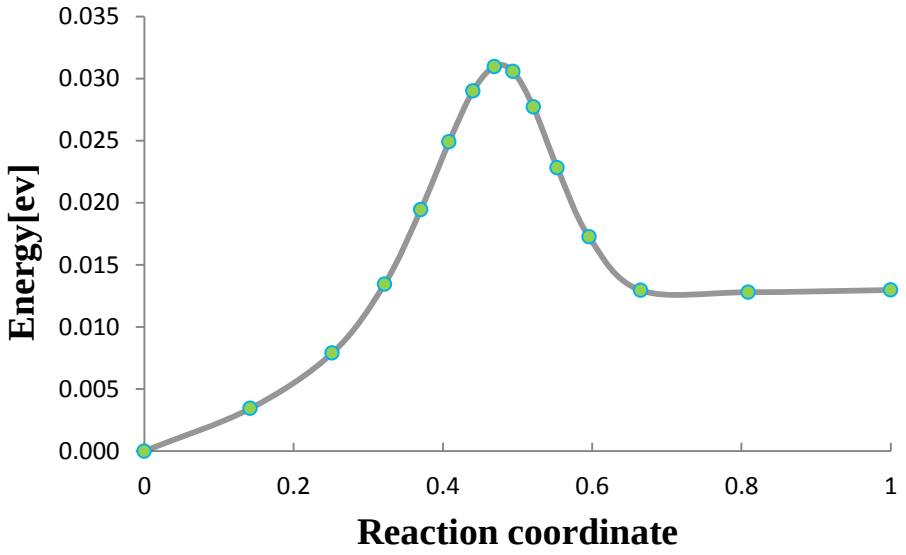

Figure 3.19 Minimum energy path for LK migration of Si-core 30 ° partial dislocation driving stress 2086 MPa.

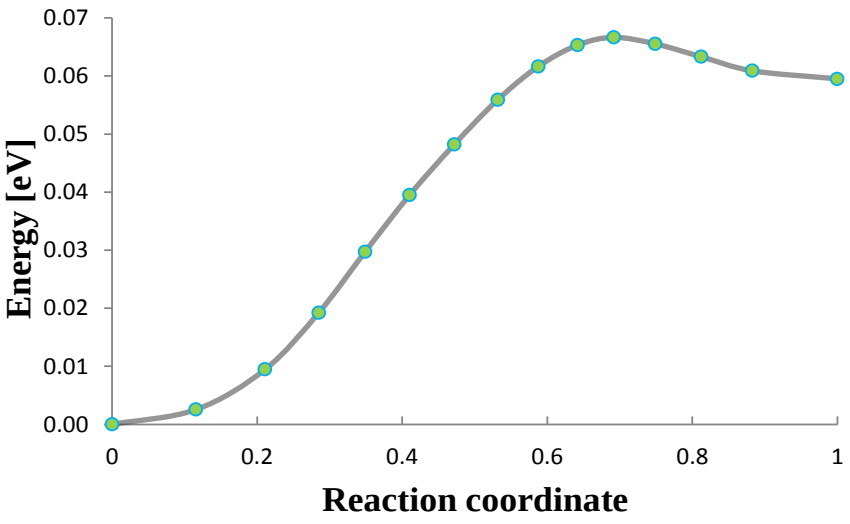

Figure 3.20 Minimum energy path for LK migration of C-core 30 ° partial dislocation driving stress 1665 MPa**.**

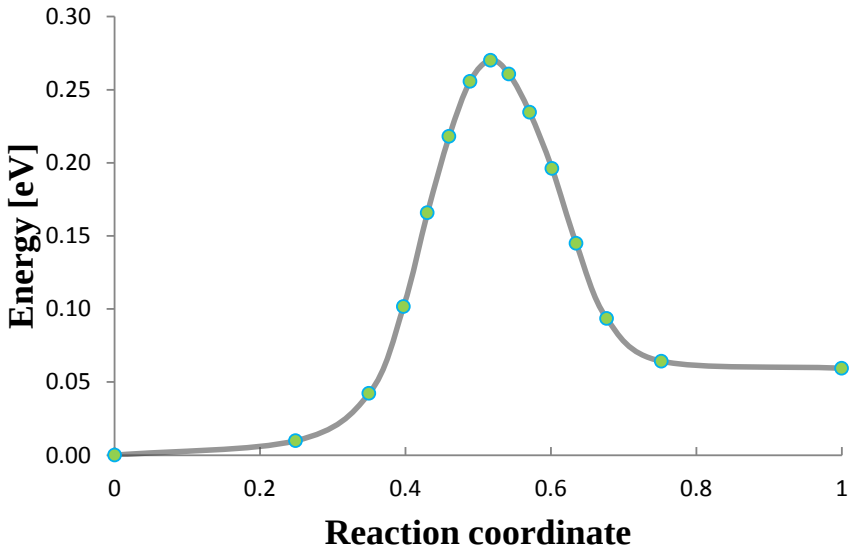

Figure 3.21 Minimum energy path for RK migration of C-core 30 ° partial dislocation driving stress 1665 MPa.

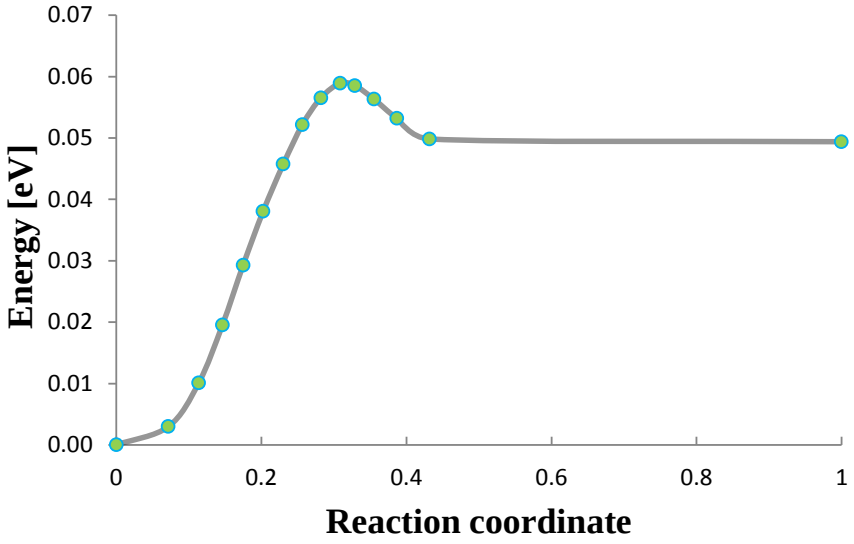

Figure 3.22 Minimum energy path for LK migration of C-core 30 ° partial dislocation driving stress 1752 MPa.

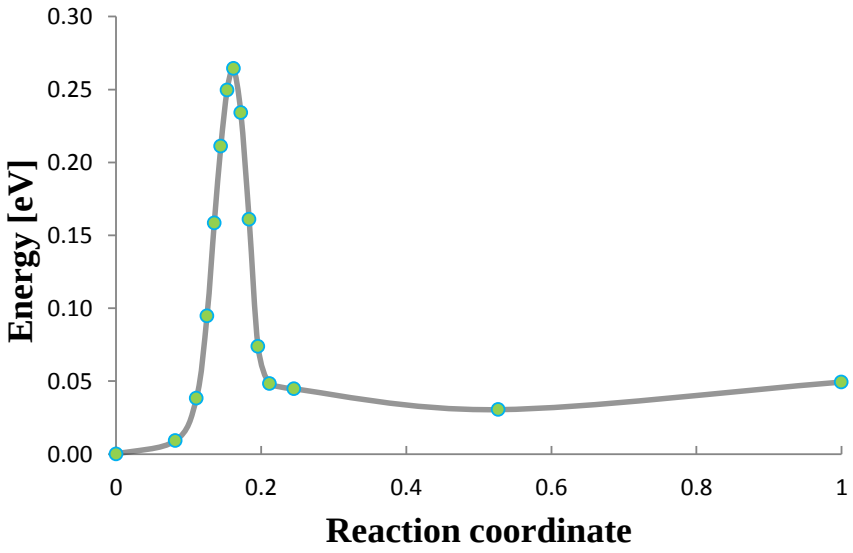

Figure 3.23 Minimum energy path for RK migration of C-core 30 ° partial dislocation driving stress 1752 MPa**.**

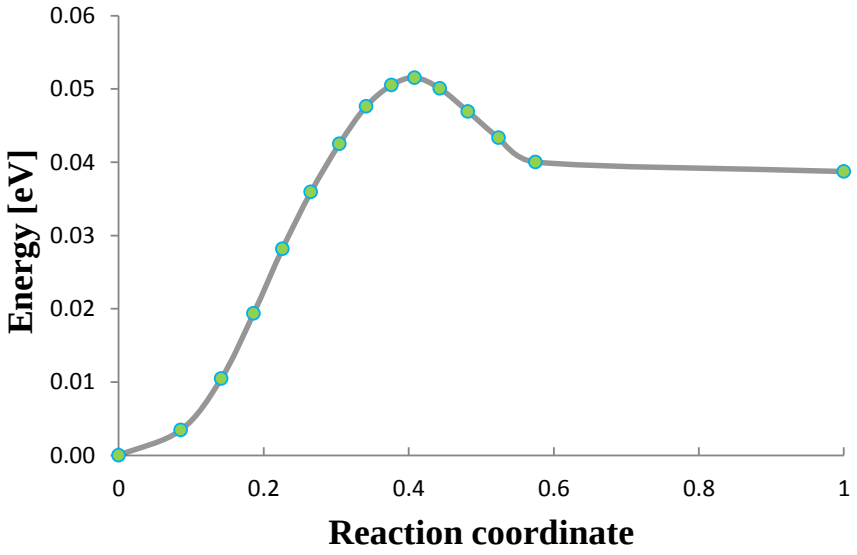

Figure 3.24 Minimum energy path for LK migration of C-core 30 ° partial dislocation driving stress 1860 MPa.

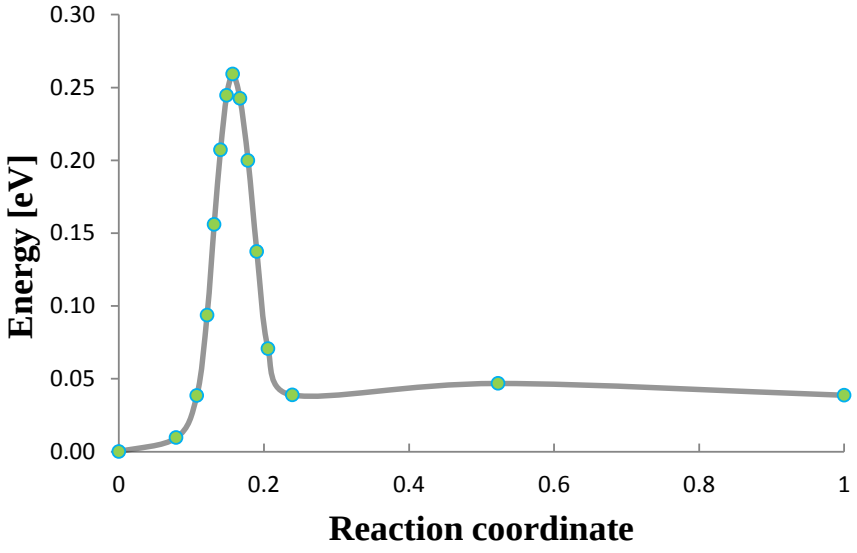

Figure 3.25 Minimum energy path for RK migration of C-core 30 ° partial dislocation driving stress 1860 MPa.

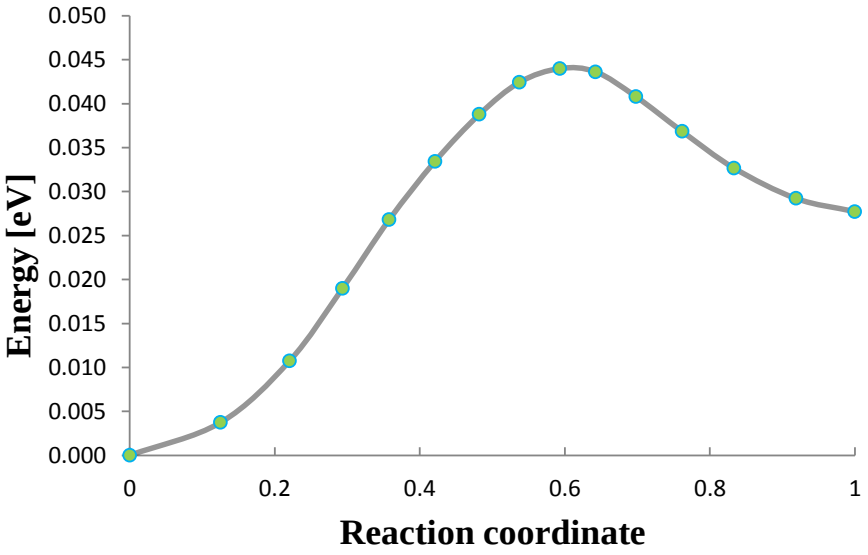

Figure 3.26 Minimum energy path for LK migration of C-core 30 ° partial dislocation driving stress 1966 MPa.

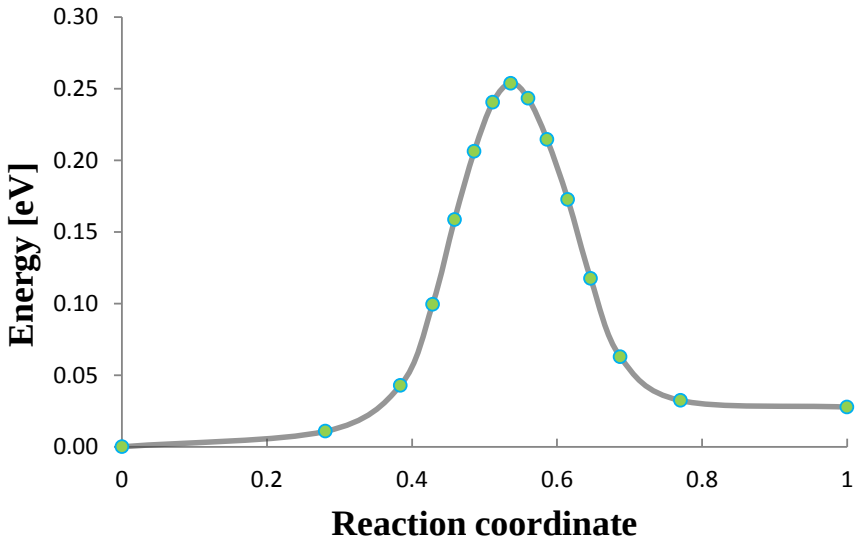

Figure 3.27 Minimum energy path for RK migration of C-core 30 ° partial dislocation driving stress 1966 MPa.

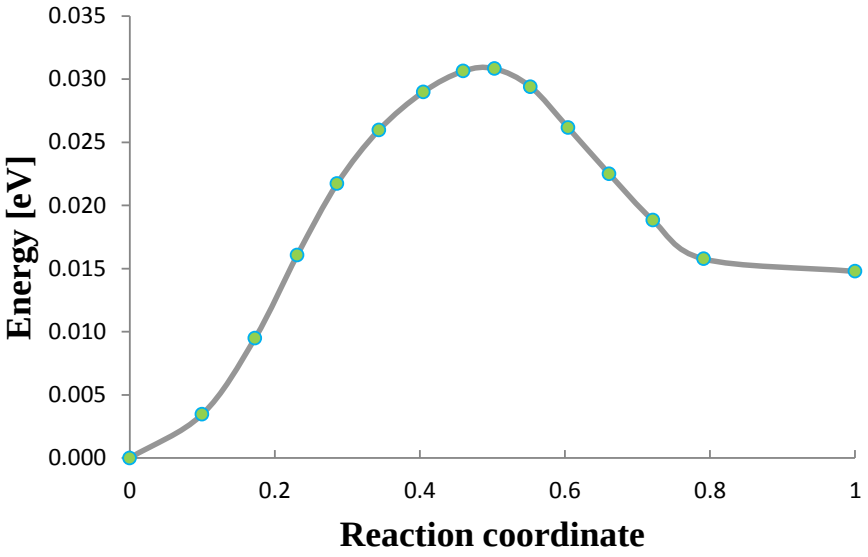

Figure 3.28 Minimum energy path for LK migration of C-core 30 ° partial dislocation driving stress 2173 MPa.

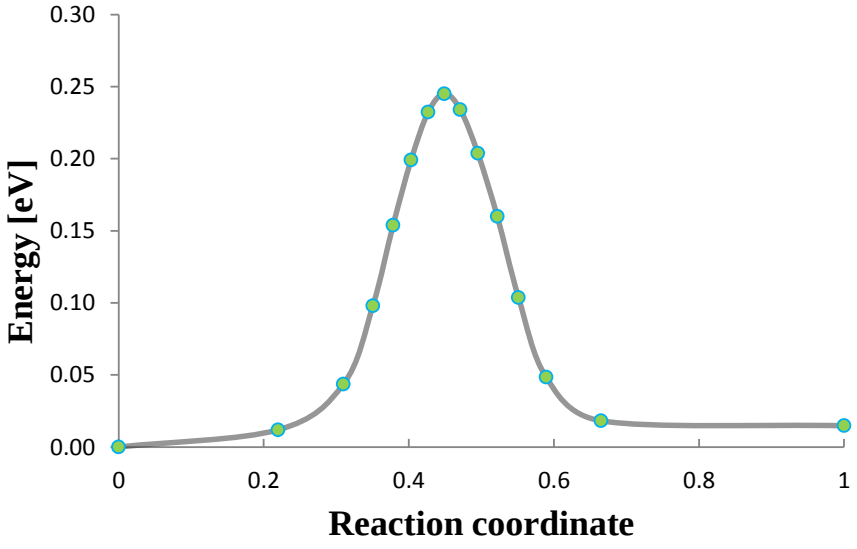

Figure 3.29 Minimum energy path for RK migration of C-core 30 ° partial dislocation driving stress 2173 MPa.

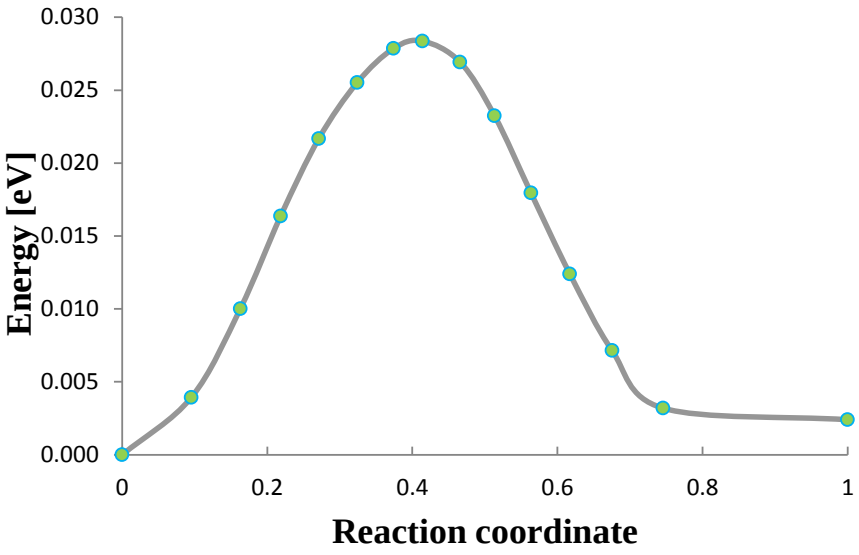

Figure 3.30 Minimum energy path for LK migration of C-core 30 ° partial dislocation driving stress 2312 MPa**.**

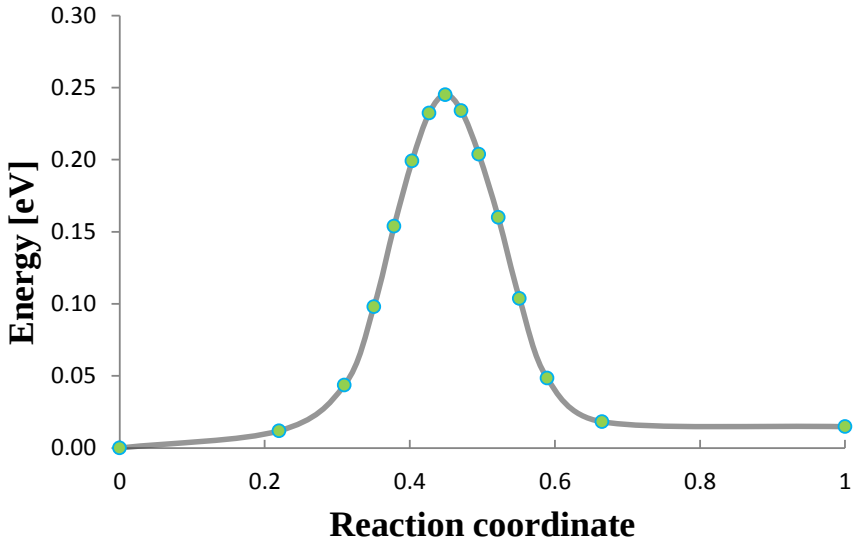

Figure 3.31 Minimum energy path for RK migration of C-core 30 ° partial dislocation driving stress 2312 MPa**.**

And Fig. 3.32 and Fig. 3.33 show the kink migration path of LK and RK for Si-core and C-core partial dislocation. The migration mechanism of LK is more complex compared with RK because of the structure difference. In LK migration path, the atom marked by black arrow is the major moving part while two atoms are shifting during the RK migration path.

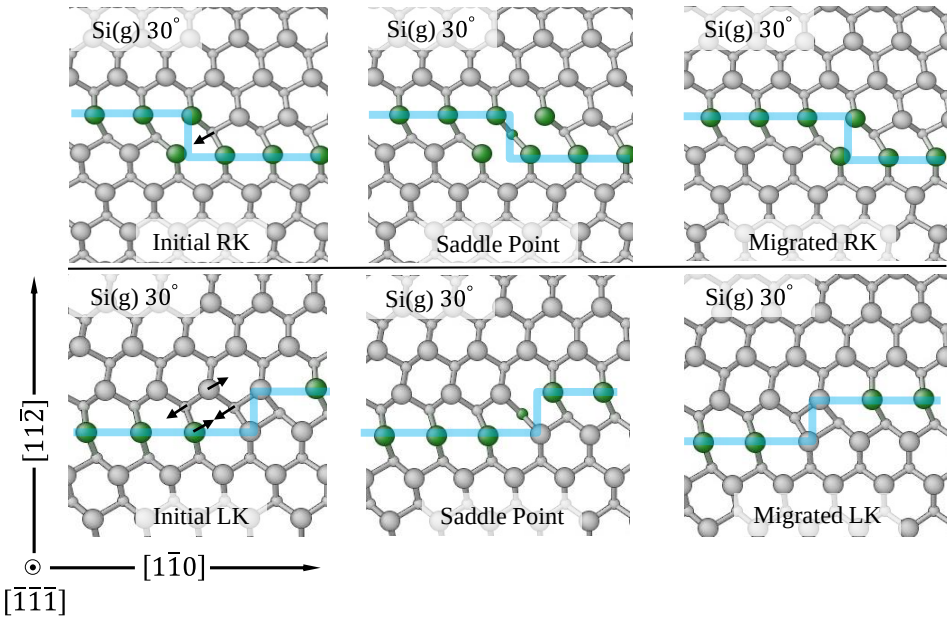

Figure 3.32 Kink migration paths for Si-core 30 °partial dislocations. The first and second row show the left and right kink (LK and RK) migration path respectively for the Si-core glide set 30 °partial dislocation.

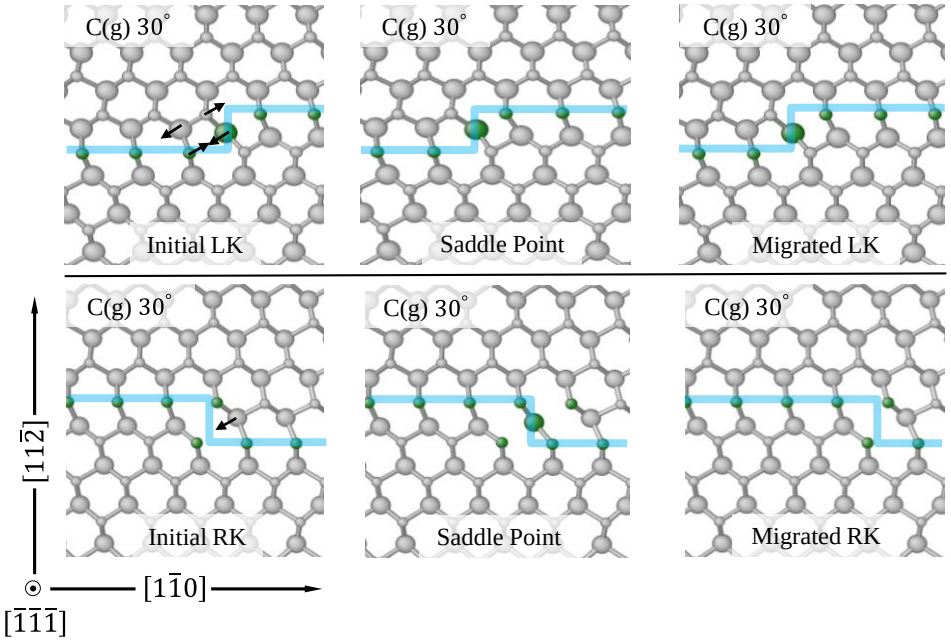

Figure 3.33 Kink migration paths for Si-core 30 °partial dislocations. The third and fourth row show the left and right kink (LK and RK) migration path respectively for the C-core glide set 30 °partial dislocation. The atom marked by black arrow is the major moving part in LK migration while two atoms shift during the RK migration path. The light blue lines show the changing of the kink pair width during kink migration.

Fig. 3.34 and Fig. 3.35 show the dependence of activation energy on the driving shear stress of LK and RK. Notice that, for 30 °partial dislocation kink migration simulation, only the high driving shear stress region is given. For the reason that, in low stress region, I can't get stable dislocation structure which probably due to the interatomic potential problem.

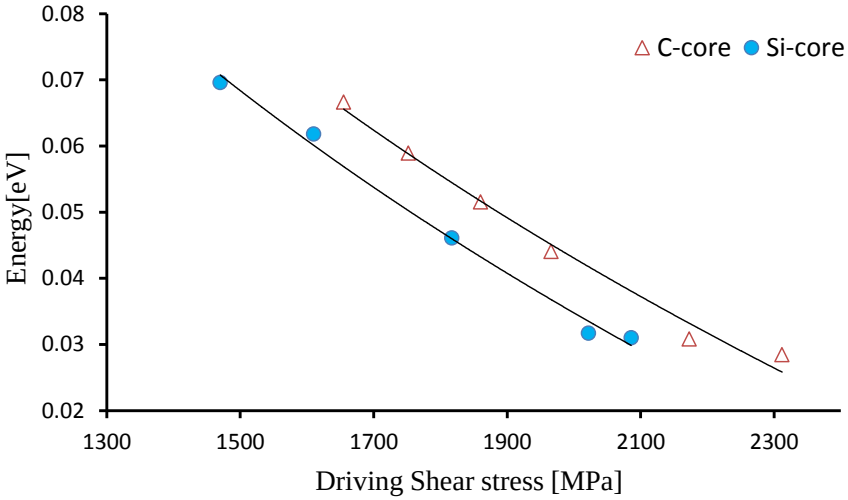

Figure 3.34 Dependence of activation energy on driving shear stress for LK kink migration in 30 °partial dislocation.

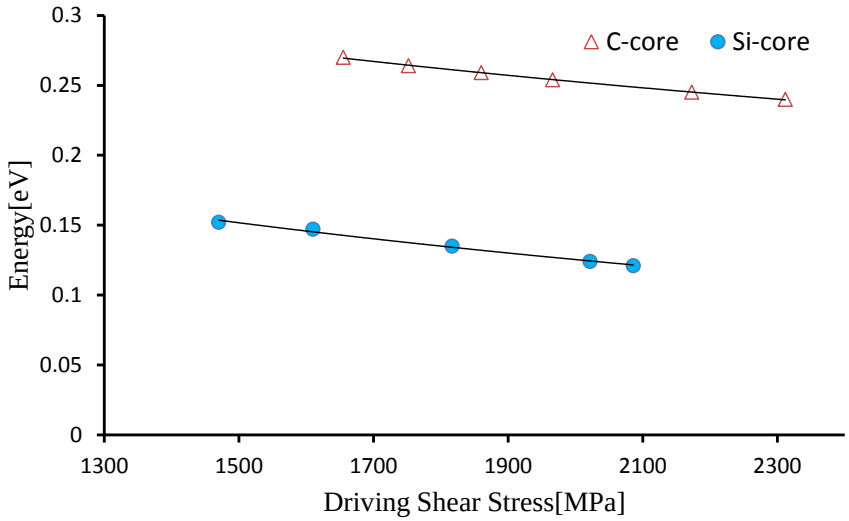

Figure 3.35 Dependence of activation energy on driving shear stress for RK kink migration in 30 °partial dislocation.

These simulation results show that the Si-core 30° degree partial dislocation has a lower activation energy barrier compared with C-core 30° partial dislocation. And, the energy

difference between the C-core and Si-core is around 0.07eV for LK, while the difference for RK is 0.13eV. Moreover, RK has a higher the activation energy barrier than LK. Compared with previous numerical study, our conclusion that LK has a lower activation energy barrier in C-core 30 ° partial dislocation is consistent with Savini's first-principle simulation (Savini *et al*., 2007a, 2007b). However, as regards the activation energy barrier of LK and RK in Si-core 30 ° partial dislocation, we have a contrary conclusion. Savini pointed out that, for Si-core 30 ° partial dislocation, the activation energy barrier for LK is 0.08eV and that for RK is 0.06eV. But in the present work, the saddle point energy is calculated to be 0.07eV and 0.152eV for LK and RK, respectively. Considering the structure similarity of RK for Si-core and C-core in 30 ° partial dislocation, the difference of migration activation energy of RK in C-core and Si-core should not be so large. Moreover, Savini's simulation result of the kink nucleation activation energy in 30 ° partial dislocation showed an opposite conclusion about the dislocation mobility compared with previous experimental results (Idrissi *et al*., 2007; Ha *et al*., 2003). Besides, as mentioned at the end of section 3.1, there is also a consistency with the fact that, for both the dislocation nucleation and migration, the partial dislocations with a larger separation between dangling bonds have a higher activation energy barrier than the partial dislocations with a smaller separation.

Fig. 3.36 shows the kink nucleation minimum energy path in C-core 30 ° partial dislocation under the driving shear stress of 3.0 GPa. And Fig. 3.37 shows kink nucleation process for both C-core and Si-core 30 ° partial dislocations. Notice that, the configurations of point 1 and point 2 do not represent the saddle point configuration in the reaction path. These two configurations are used to give a better illustration that, for each core of 30 ° partial dislocation, one RK and two LKs migrate in sequence to complete the kink nucleation process. Indeed, these migration processes are not exactly the same compared with the RK and LK migrations which are mentioned in Fig. 3.32. and Fig. 3.33 But, they have similarity in the migration mechanism of the major moving part. Moreover, the C-core and Si-core 30 ° kink nucleation paths are simulated with driving shear stresses of 3.0 GPa and 2.34 GPa respectively. The activation energy barriers are 1.03 eV and 1.04 eV for C-core and Si-core. It is well-known that the activation energy barrier decrease as the driving shear stress increase. Therefore, I can conclude that in the 30 ° partial dislocation kink nucleation the Si-core has a lower activation energy barrier than C-core 30 ° partial dislocation. The previous first-principle calculation that was done

by Savini *et al*. (2007a, 2007b) showed that the kink formation energy barriers are 1.48 eV and 2.12 eV for C-core and Si-core in 30 ° partial dislocations respectively. Our conclusion about which type of 30 ° partial dislocation has lower action energy barrier is contradicted to that of Savini's. This contradiction might be caused by the size of the model employed in the numerical simulation. In summary, the kink nucleation in 30 ° partial dislocation has a higher activation energy barrier than the 90 ° partial dislocation. At the same time, for kink migration, the 30 ° partial dislocation has a lower activation energy barrier compared with the 90 ° partial dislocation.

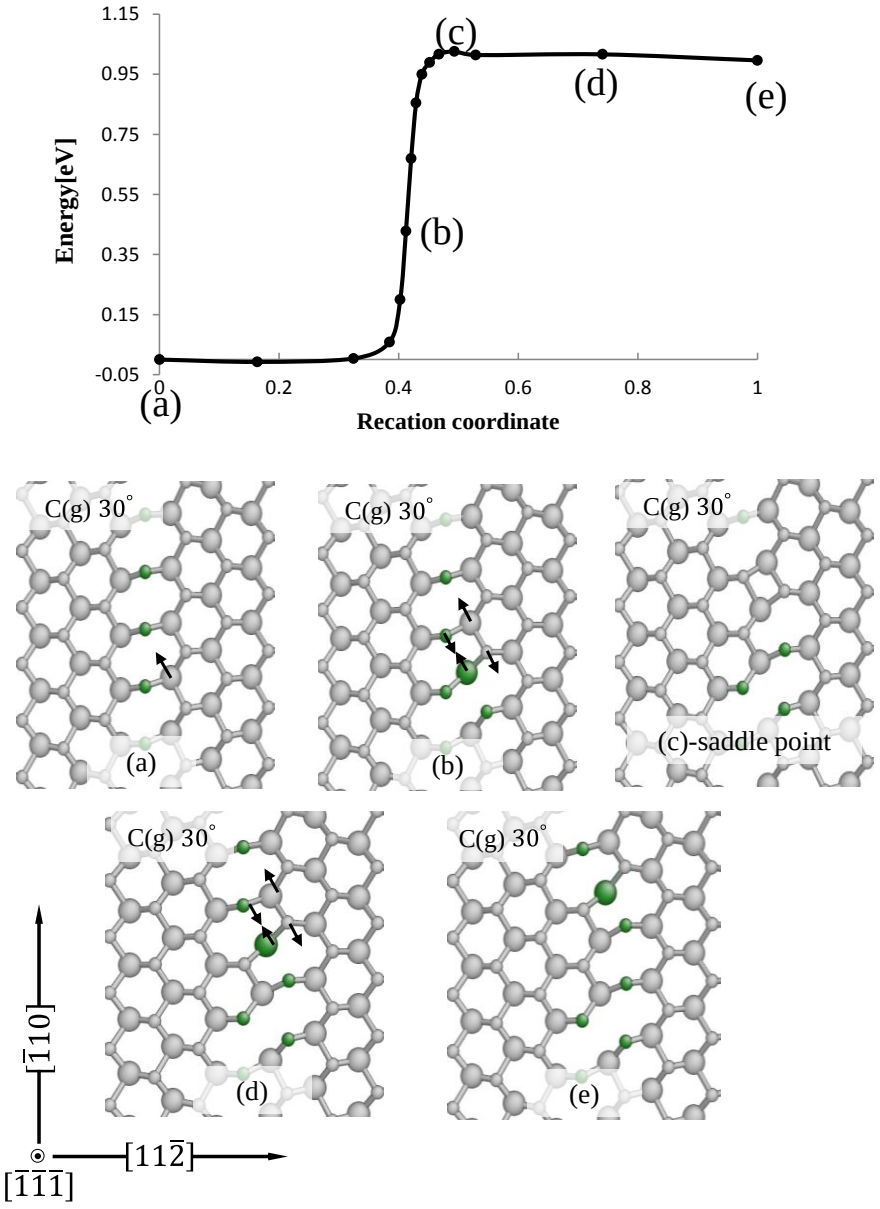

Figure 3.36 Minimum energy pathway of kink nucleation in C-core 30 ° partial dislocation.

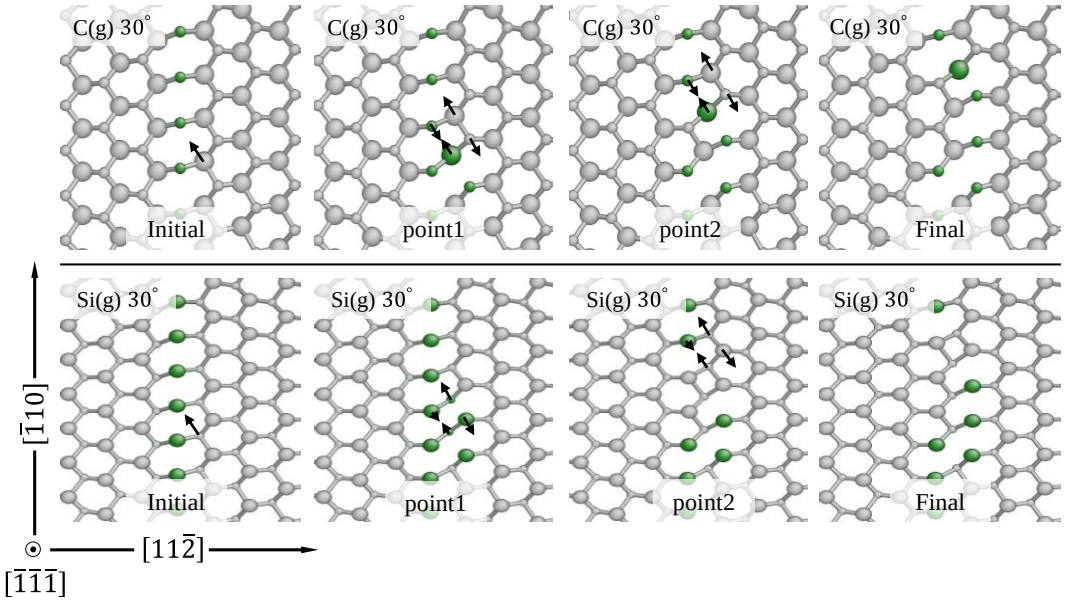

Figure 3.37 Kink nucleation paths for 30 ° partial dislocation. The first row shows nucleation path of the C-core glide set 30 ° partial dislocation with a driving stress of 3.0 GPa. The second row shows kink nucleation path of the Si-core glide set 30 ° partial dislocation with a driving stress of 2.26 GPa. The nucleation process can be thought of as one RK and two LKs migration.

3.4 Morphology of partial dislocations

In 1981, using an in-situ TEM technique, Hirsch *et al*. (1981) pointed out that the morphology of 90 ° partial and 30 ° partial dislocation lines are different, the 90 ° partial dislocation line was found to be cusped as a zigzagged line while the 30 ° partial dislocation line was smooth and straight. Since then, researchers have tried to find a connection between the morphology of the partial dislocation line and the types of dislocation line, such as different core nature or the types of partial dislocations (e.g., 30 °, 90 °). Ning and Pirouz (1996) and Stahlbush *et al*. (2004) showed that, in their observation, all the Si-core partial dislocation had a smooth shape while the C-core partial dislocation were zigzagged as shown in Fig. 3.38. They attribute the dislocation line morphology difference to their core nature.

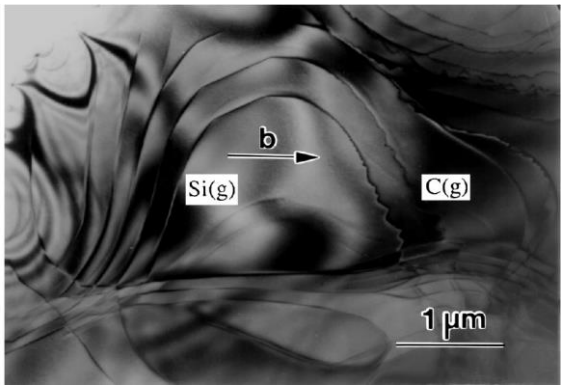

Figure 3.38 Dislocation line image by TEM (Ning and Pirouz, 1996). With permission from Cambridge University Press.

On the other hand, Pilyankevich *et al*. (1982, 1984) and Maeda *et al*. (1988) attribute the different morphologies of partial dislocations to their Burgers vector. After that, Mussi *et al*. (2007) and Lancin *et al*. (2009) found that C-core partial dislocation could be either straight or zigzagged. Moreover, Mussi *et al*. (2007) also pointed out that both the C-core partial dislocation and Si-core partial dislocation can be the leading partial dislocations when the perfect dislocation moves out the basal plane of 4H-SiC. In Fig. 3.39, a dislocation loop bounded by four partial dislocations is presented. All these partial dislocations including both the C-core and Si-core partial dislocations are seemed to be smooth. Their experimental data indicates the core nature of partial dislocations cannot be deduced from the morphology of the dislocation line.

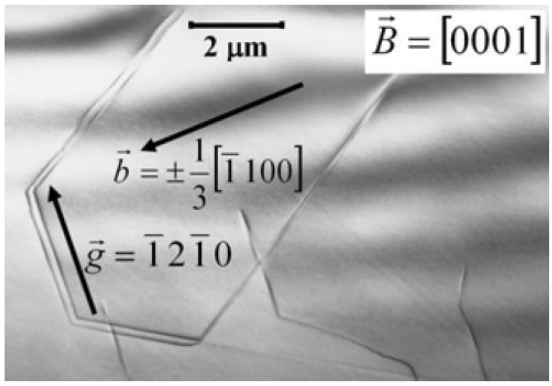

Figure 3.39 Dislocation loop bounded by partial dislocations. (Mussi *et al*., 2007) with the permission from John Wiley and Sons.

Until now, this controversy is still going on, and most of the research in this area is experimental. I have not seen any theoretical computation performed that has provided an

understanding of the partial dislocation line morphology. Here, based on the reaction path analysis of the partial dislocation activation energy, I propose new models to describe this morphology difference.

For representing the kink nucleation and migration paths in section of 3.1, I conclude that, migration and nucleation have similarities in terms of the motion of atoms at and near the dislocation core. Fig. 3.40 shows a comparison of the minimum energy path for kink nucleation and migration in 90 ° partial dislocation. Notice that in the kink nucleation path, the activation energy barrier for saddle point 1 is almost the same ($E_1 \approx E_s$) as the kink migration energy. This means that if for kink migration, part of the kink nucleation process has also been produced. Moreover, think of the activation energy as a pulse, if the pulse is not large enough to cover the barrier for saddle point 2 but large enough to cover saddle point 1, the existence of the local minimum which is marked by a red spot in Fig. 3.40 can insure that the kink has the probability to be stable with this configuration. In other words, the kink migration and nucleation have the same probability to be generated. Of course, in this case the kink nucleation process is not finished within a local minimum configuration. Based on the above, I propose a mechanism for the 90 ° partial dislocation kink propagation in Fig. 3.41. Once the 90 ° partial dislocation kink is nucleated, there are several possible activation energy barriers. Here, D1 and D3 present the probability for kink migration; D2 means the probability for a new kink nucleating from the top of the original one while D4 means the probability for another new kink to nucleate on the remaining dislocation line. We already know that, the activation energy barrier for the saddle point 1 is almost the same ($E_1 \approx E_s$) compared with the kink migration activation energy. These similar activation energy barriers indicate that the kink migration and part of the kink nucleation can be produced with similar possibilities. In addition, for the structure's symmetric character, we get that D1= D3. Based on the above, I conclude that about the possibility for four different kind of kink movement direction: D1= D3 ≈ D2 ≈ D4. This conclusion shows that, if the 90° partial dislocation kink has enough energy to be migrated, a part of the kink nucleation can be nucleated too. The phenomenon about the similar activation energy barriers in kink nucleation and kink migration is also found under other driving stress shown in Fig. 3.42. Therefore, I propose that the 90 ° partial dislocation lines have a zigzagged morphology.

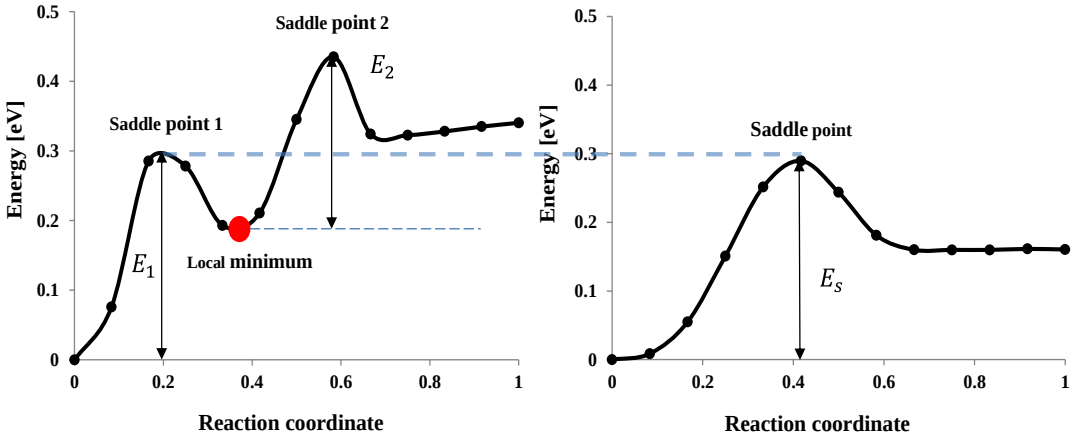

Figure 3.40 Minimum energy path for kink nucleation and migration in 90° partial dislocations under a driving shear stress of 0.3 GPa. The red spot shows the local minimum in the kink nucleation path. The light blue line show the value difference between the saddle point in kink migration and saddle point 1 in kink nucleation is very small. In kink nucleation path, $\boldsymbol{E_1}$ represents the activation energy barriers for saddle point1 while $\boldsymbol{E_2}$ represents the activation energy barriers from the local minimum spot to saddle point 2. $\boldsymbol{E_s}$ represents the activation energy barriers for kink migration. And, $\boldsymbol{E_1 \approx E_s > E_2}$.

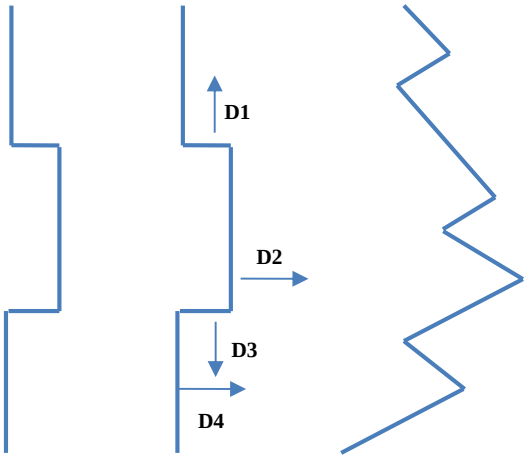

Figure 3.41 Kink propagation mechanism for 90° partial dislocation. D1, D2, D3 and D4 show the possibility for each direction which the kink can migration in. With the similar possibility each direction, the 90° partial dislocation line could have a zigzagged morphology.

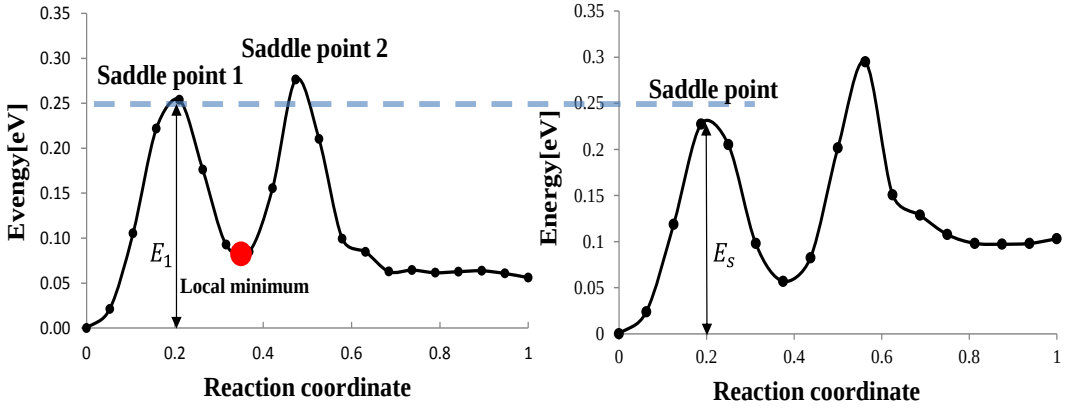

(a) Minimum energy path of Kink nucleation. (b) Minimum energy path of Migration.

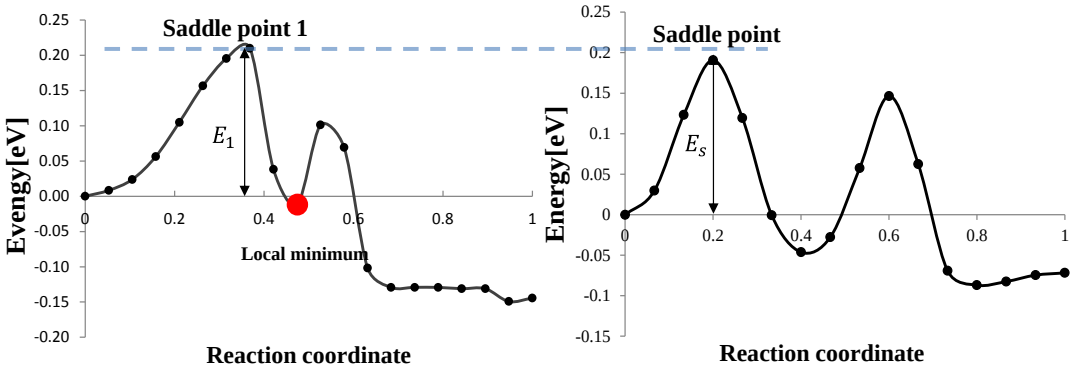

(c) Minimum energy path of Kink nucleation. (d) Minimum energy path of Migration.

Figure 3.42 The upper figures and bottom figures show the minimum energy path for kink nucleation and migration in 90 ° partial dislocations under a driving shear stress of 0.83 GPa and 1.34 GPa, respectively. The red spot shows the local minimum in the kink nucleation path.

The kink propagation mechanism for 30 ° partial dislocation is different. In Fig. 3.43, we show the minimum energy path way for the kink nucleation with a driving shear stress of 3.0 GPa and migration of RK and LK with a driving shear stress of 2.3 GPa. In the 30 ° partial dislocation kink nucleation path, there is only one saddle point, no local minimum. And the large difference of the activation energy barriers between the kink nucleation and migration indicate that once the kink is nucleated, both LK and RK can migrate freely while the kink still does not have enough energy to nucleate a second kink. Moreover, since the activation barrier of RK is about 10 times than that of LK, I propose that after nucleation, the kink prefers to migrate because of the lower activation energy of LK.

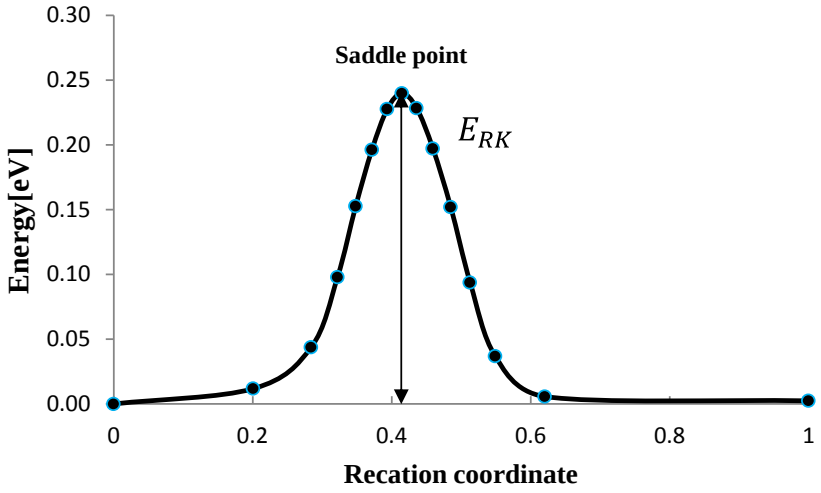

(a) LK migration under a driving stress of 2.3 GPa.

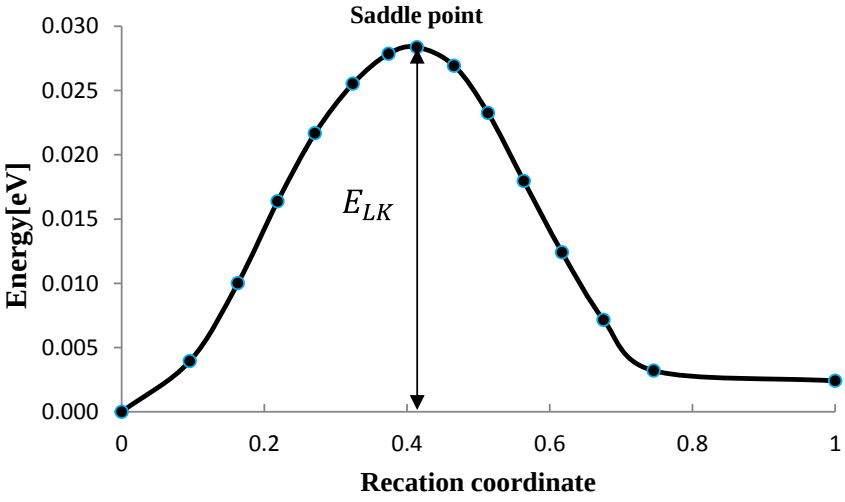

(b) RK migration under a driving stress of 2.3 GPa.

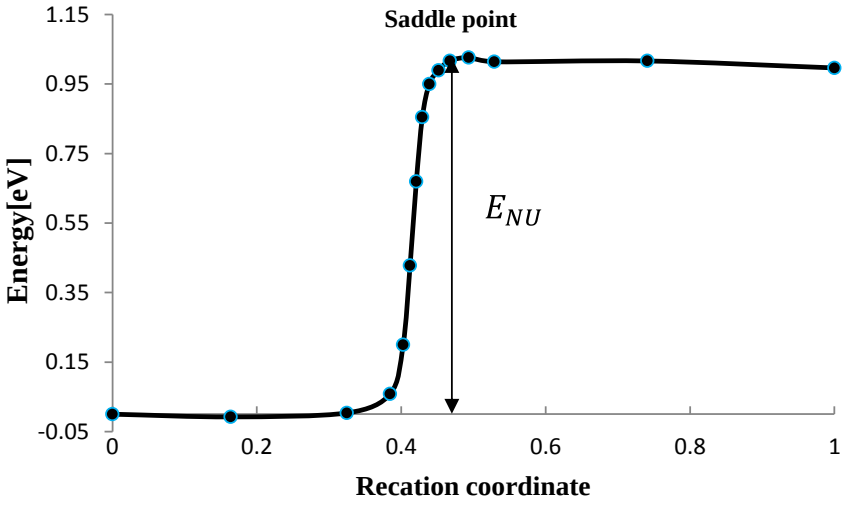

(c) Kink nucleation under a driving stress of 3.0 GPa.

Figure 3.43 Minimum energy path for kink nucleation and migration in 30° partial dislocations with a driving shear stress of 3.0 GPa and 2.3 GPa respectively. E_{RK} and E_{LK} represent the migration activation energy barrier for RK and LK, respectively. E_{NU} represents the activation energy barriers for nucleation.

Fig.3.44 shows the schematic representation of the glide energetic configuration, beginning from kink pair nucleation with different widths. Once the kink nucleation process is finished, for 90° partial dislocation, the kink can migrate in two directions. For the symmetric kink pair character of 90° partial dislocation, no matter which direction the kink migrates, the energy curve in Fig.3.44 would be the same because of the same activation energy barrier for RK and LK. However, for the 30° partial dislocation as mentioned in last paragraph that the LK kink prefers to migrate because of its lower migration activation energy after the kink nucleation process is finished. This glide process is showed in Fig.3.44 (b). Combination with the large difference in activation energy barrier for kink nucleation and migration, I propose that during the 30° partial dislocation propagation, once the LK is nucleated, it prefers to continue migrating since its migration energy is lower than that of RK. And the large difference of activation energy barrier between kink nucleation and migration can induce that the kink can keep migrating until the energy is large enough to nucleate a new kink. In this way, the 30° partial dislocation lines always have a smooth morphology. This kink propagation mechanism for 30° partial dislocation is shown in Fig.3.45. The RK with a larger activation energy barrier than LK should have a higher possibility be represented or left on the dislocation lines as step (e)

in Fig.3.45. This predication is verified by Ohno *et al.* (2012). Their experiment data is shown in Fig.3.46.

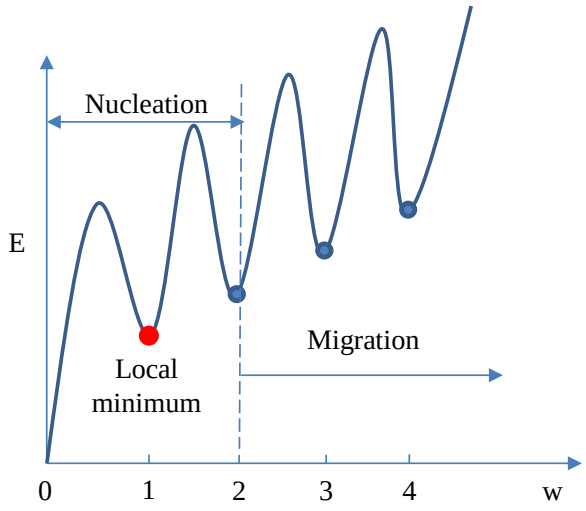

(a) 90° partial dislocation propagation.

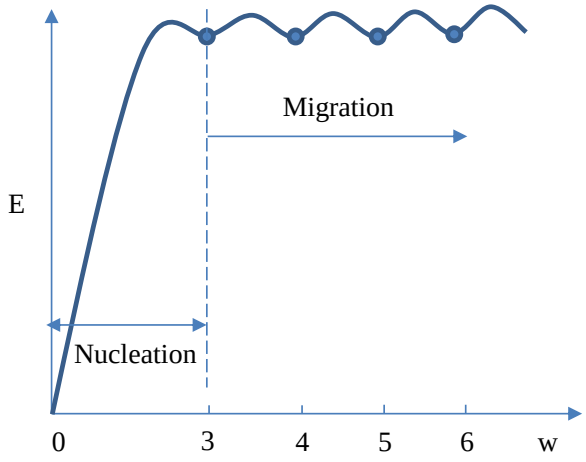

(b) 30° partial dislocation propagation.

Figure 3.44 Schematic representation of the glide energetics of a dislocation. w is the kink pair width during glide of the 30 °partial dislocation. (a) shows the energy in glide process for 90 ° partial dislocation, and the red spot shows the local minimum in the kink nucleation path. (b) shows the energy in glide process for 30 °partial dislocation. During this migration, only the LK migration is represented for the reason that LK has a much lower activation barrier as compared to RK.

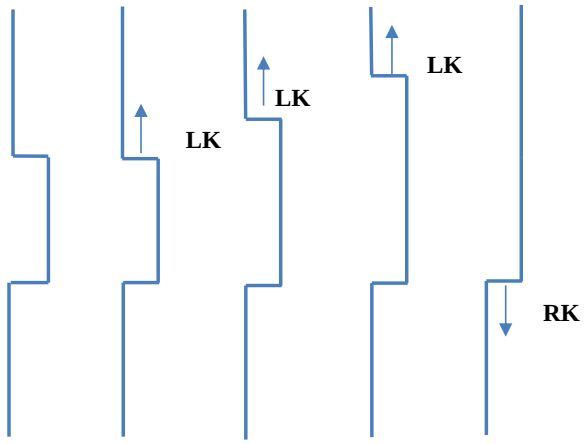

Figure 3.45 Schematic representation of shape evolution of a 30° partial dislocation line during glide. The (a) (b) (c) (d) (e) show each step of the dislocation propagation by energy preference.

The RK with a larger activation energy barrier than LK should have a higher possibility be represented or left on the dislocation lines. This predication is verified by Ohno *et al.* (2012). Their BF-TEM experiment images are shown in Fig.3.46. (a) and (b) show the image with 3 s electron irradiation when (c) shows the image after the irradiation. (d) shows the shape 30° partial dislocation line. By the BF-TEM data, Ohno *et al*. (2012) proposed that the RK structure is the dominate one on the dislocation line, because of the RK has been accumulated on the dislocation line for a lower mobility. The geometry of the kink is shown as (d) in Fig.3.46. This figure also shows that the 30° Si-core partial dislocation line is smooth and has a higher mobility than the C-core 30° partial dislocation under the electron irradiation. H. Idrissi *et al*. (2005) also observed the 30° Si-core partial dislocation line image by TEM in weak beam modes with the temperature range 400℃-700℃ that the dislocation line image is shown in Fig. 3.47. D1 and D2 represent two glide-set 30° Si-core partial dislocation lines as the boundaries of the double stacking fault. From the image, we can tell that the morphology of 30° Si-core partial dislocation lines tends to be straight line that is consistent with the observation from Ohno *et al*. More importantly, the controversy bout activation energy barriers of the RK and LK in 30° partial dislocation that which come from our molecule dynamics simulation result and the first principle calculation by Savini *et al*. (2007a, 2007b) can be solved. In Savini's result, for 30° Si-core partial dislocation, the activation energy barriers of RK and LK are 0.06eV and 0.08eV, respectively. Obviously, this result is contradicted with Ohno's observation result. At the same

time, our simulation result and dislocation morphology proposition are demonstrated well by these experiment data.

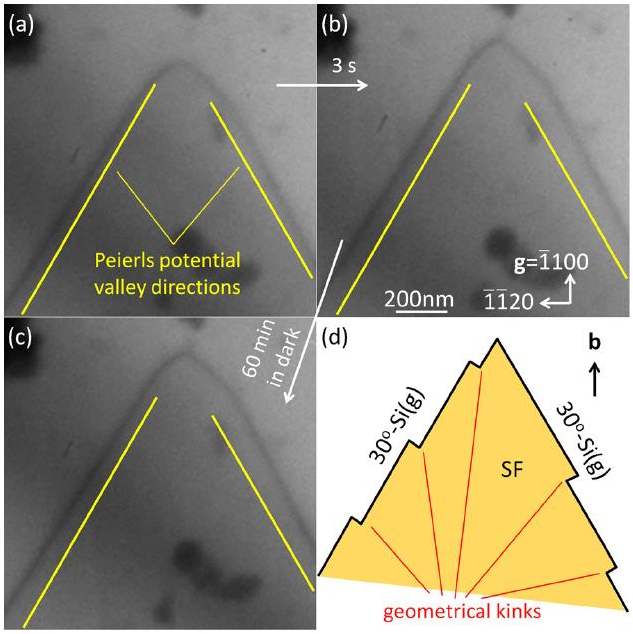

Figure 3.46 BF-TEM images of 30 ° Si-core partial dislocation line (Ohno *et al*., 2012). With the permission from AIP Publishing LLC.

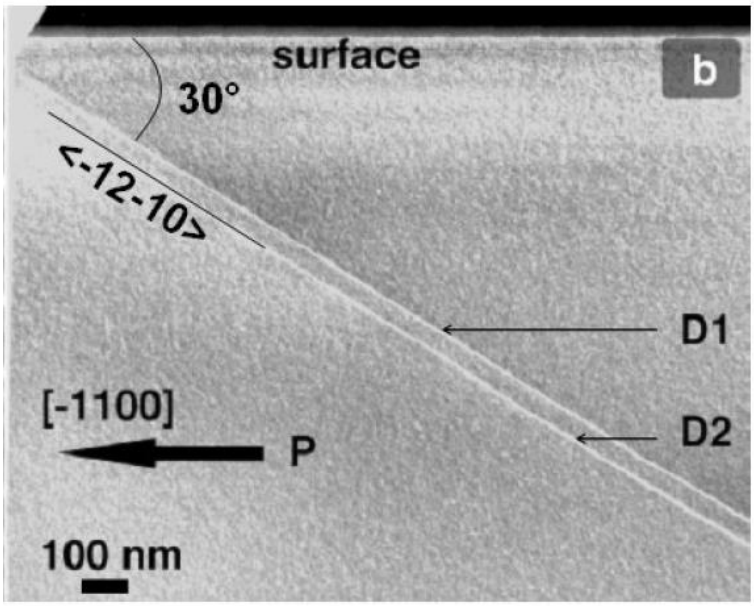

Figure 3.47 Weak beam image of two 30 ° Si-core partial dislocation line marked by D1 and D2. With permission from AIP Publishing LLC.

3.5 Stacking fault morphology

Stacking faults as the plane defect in silicon carbide are bounded by partial dislocations. And the stacking fault expansion is carried out by the motion of the partial dislocations. Therefore, the propagation and morphology of the stacking fault are related to the partial dislocation lines' propagation and shape. At first, based on our calculation of activation energy barriers and Equation 3-1, the energy Q which represents the dislocation velocity is summarized in Tab 3-1. And the F_k is given as Equation 3-2, E_{int} is the interaction between the kinks while the $E_{nucleation}$ is the activation energy barrier of the kink nucleation pair.

$$2F_k = E_{nucleation} - E_{int} \tag{3-2}$$

The E_{int} for 90° and 30° partial dislocations is given as Equation 3-3 and 3-4, respectively (Hirsh and Lothe, 1982). μ is the shear modulus, as 1.23ev/Å. b_p means the modulus of the burgers vector and ν=0.21 as the Possison's ratio. h is the height of the kink while $a_0 = 3.06$Å, and n =1 in here which represent the kink width (Savini *et al*., 2007).

$$E_{int} = -\frac{\mu b_p^2 h^2}{8\pi n a_0}\frac{1-2\nu}{1+\nu} \approx -\frac{0.24}{n}eV \tag{3-3}$$

$$E_{int} = -\frac{\mu b_p^2 h^2}{32\pi n a_0}\frac{4+\nu}{1-\nu} \approx -\frac{0.49}{n}eV \tag{3-3}$$

In the Table 3-1, most of the nucleation and migration energy barriers for Si-core and C-core partial dislocation are calculated with the driving stress 2.3GPa, expect the nucleation activation energy barrier of the 30° partial dislocation of C-core is given with the driving stress 3GPa. From Table 3-1 and Equation 3-1, I can conclude that $V_{\mathrm{si}}^{90} > V_{\mathrm{c}}^{90} > V_{\mathrm{si}}^{30} > V_{\mathrm{c}}^{30}$. The Si-core partial dislocation has a higher mobility than the C-core partial dislocation with the same partial dislocation burgers vector. As I mentioned in section 3.1, this conclusion is consistent with previous experimental data (Lara *et al*., 2012; Ning *et al*., 1996; Idrissi *et al*., 2007; Ha *et al*., 2003). Moreover, our calculation result also show indicate that 90° partial dislocation has a higher mobility than 30° partial dislocation for both C-core and Si-core. We should notice that most of these experiment data only provided the data about the comparison the C-core and Si-core 30° partial dislocations. In deformation test by Idrissi *et al*. (2007), he

asserted that the lacking of observation of the Si-core 90° partial dislocation is due to its highest mobility. The Si-core 90° partial dislocation line could have already moved out of the sample before the observation. In the TEM test by Lara (2012), the burger vectors of the partial dislocation lines are not concerned for the 90° and 30° partial dislocations. That may be caused by their experiments were applied on the 4H-SiC that the TED (threading edge dislocation) and TSD (threading screw dislocation) are the major dislocation types. Those observed partial dislocations are dissociated from the TED and TSD have different mechanism with that those of 3C-SiC. Therefore, by experimental method, we have a widely accept that the Si-core partial dislocation moves ahead of the C-core partial dislocation with a higher mobility. The mobility for 30° partial dislocation of Si-core is more complex than the 90° partial dislocation of C-core. For the several possible reasons that, the dangling bond along the dislocation line can serve as the efficient non-radiative recombination center that provides activation energy for the motion of the dislocation (Skowronski *et al*., 2002); the recombination-induced stacking fault could be another reason that the solitons on 30° partial dislocation of Si-core can providing electron-hole recombination energy that which enhance the motion of dislocations (Galeckas *et al*., 2006). These electron phenomena have a great influence on the mobility of Si-core 30° partial dislocation.

Table 3-1 Energy Q for dislocation velocity calculation.

Dislocation Types	$E_{nucleation}$	W_m	$2F_k$	$Q = 2F_k + W_m$
90° Si-core	0.131	0.11	0.371	0.481
90° C-core	0.205	0.22	0.445	0.665
30° Si-core	1.03	0.02	1.52	1.54
30° C-core	1.04(3Gpa)	0.028	1.53	1.55

By the dislocation velocity concluded above, the morphology of the stacking fault which is bounded by partial dislocation can be predicted. The stacking fault region can be formed by the moving of the partial dislocations. For the dislocation loop, as shown in Fig. 3.48, the light lines represent the Si-core partial dislocation lines when the blue lines represent the C-core partial

dislocation lines. The short blue arrow shows the burgers vector of the dislocation line. The partial dislocation types are identified by the angle between the dislocation line and the burgers vectors. Four possible kinds of half dislocation loops can be deduced from the dislocation loop, as shown in Fig 3.49. For the higher mobility of the 90° partial dislocations for both C-core and Si-core, these dislocation lines will move out of the dislocation loop. The reason why we are focusing on the half dislocation loop is that the interface between the substrate and the wafer of SiC always has the largest intrinsic stress. And the sharp corner can lower down the activation energy barrier for the dislocation loop migration.

As illustrated in Fig. 3.50, the dislocation loop develops into a triangle shape. The similar kind of stacking faults are observed by independent work, such as optical micrograph (Vasiliauskas *et al*., 2012), TEM (Hristu *et al*., 2014), luminescence image (Liu *et al*., 2007) and photoluminescence technique (Piluso *et al*., 2014). Liu *et al*. (2007) showed that both the Si-core and C-core 30° partial dislocations are electrically active. The Si-core 30° partial dislocations can move by the REDG mechanism while the C-core 30° partial dislocations were immobile that may be caused by the higher activation energy barrier. The image (c) in Fig. 3.50 also indicates that the 30° partial dislocations line has a smooth morphology. Moreover, Vasiliauskas *et al*. (2012) pointed out that the stacking fault of 3C-SiC which was grown on 6H-SiC had a triangle outline as shown in Fig. 3.50 image (b). The bounded partial dislocation lines were smooth either.

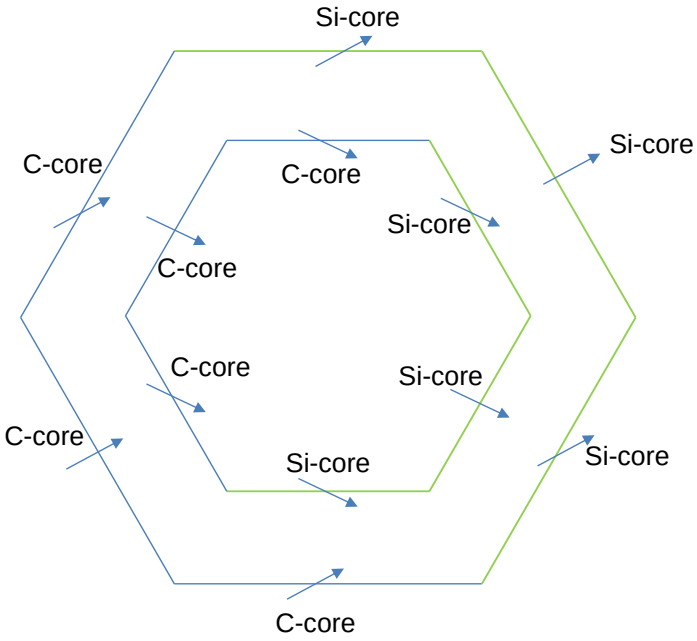

Figure 3.48 Dislocation loop in silicon carbide.

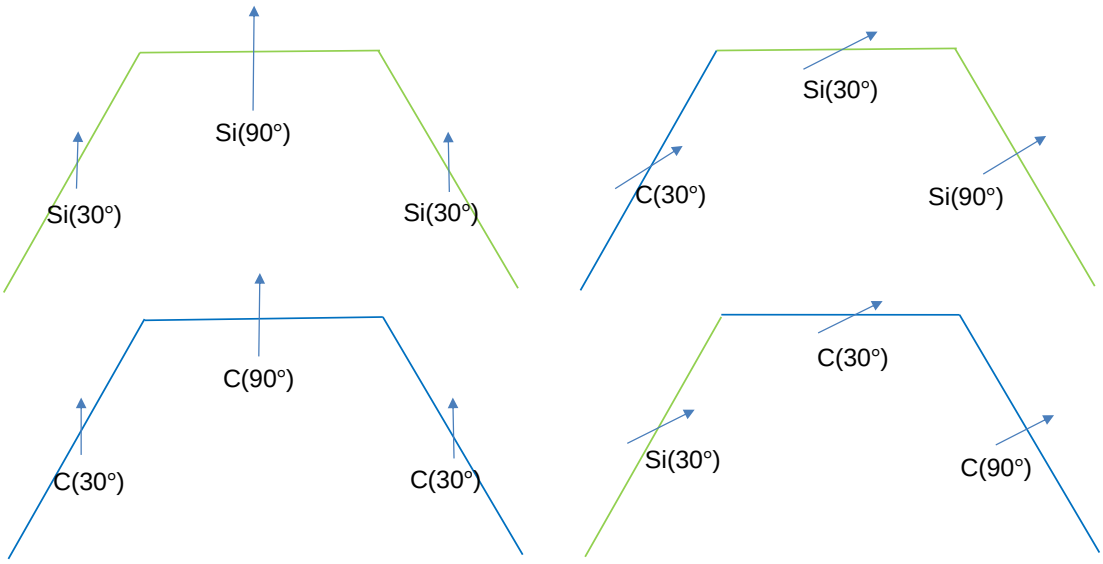

Figure 3.49 Possible half dislocation loops in 3C-SiC.

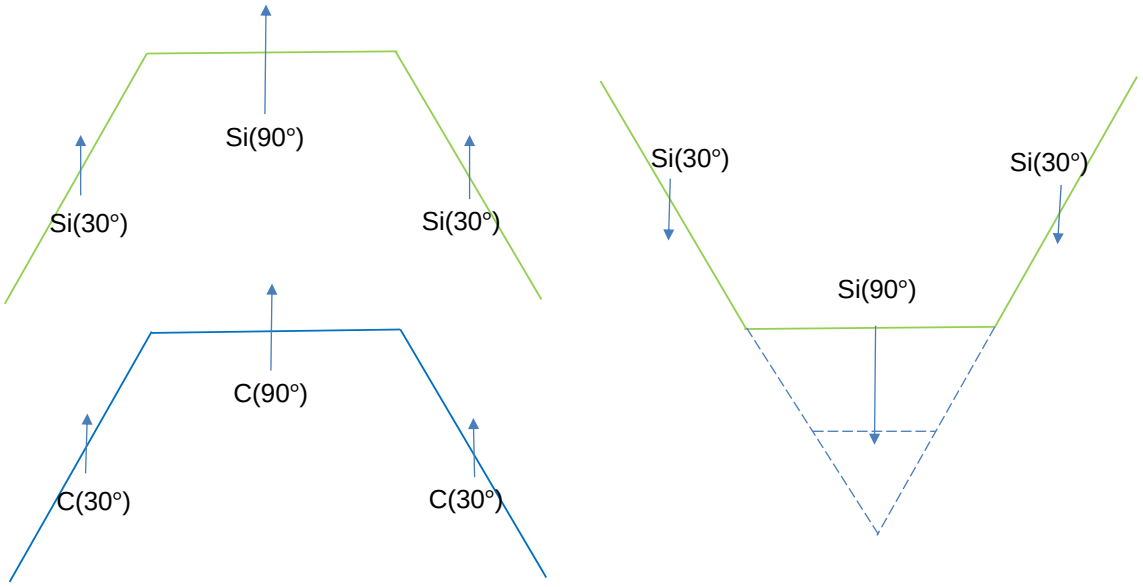

(a) Shape evolution of the dislocation loops.

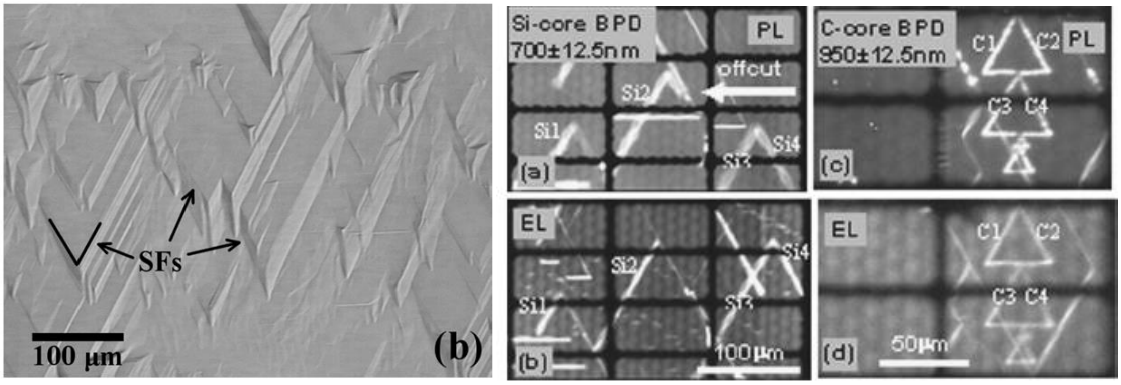

(b) Optical micrograph of 3c-sic (c) Luminescence image sic-4h

Figure 3.50 (a) Schematic representation of shape evolution for the triangle stacking faults. (b) Optical image of the triangle stacking fault along the (111) planes in 3C-SiC (Vasiliauskas *et al*., 2012). Photocopy right is covered by CCC Annual License Academic.(c) Luminescence image of triangle stacking fault which is bounded by 30° Si-core and C-core partial dislocations (Liu *et al*., 2007). With the permission from AIP Publishing LLC.

Based on the other two types of dislocation loops, the stacking fault expanded with the trapezoid shape. The shape evolution is shown in Fig. 3.51 image (a). By the higher mobility of 30° partial dislocations, the half dislocation loop expand this side more readily compare with that of others. Therefore, a trapezoid stacking faults can be formed. The image (b) shows the microscope image of stacking fault with a trapezoid in 3C-SiC (Nagasawa *et al*., 2006). The

bolded green lines are used for representing the outline of the stacking faults. Our prediction model is similar to their experimental data about the trapezoid stacking faults.

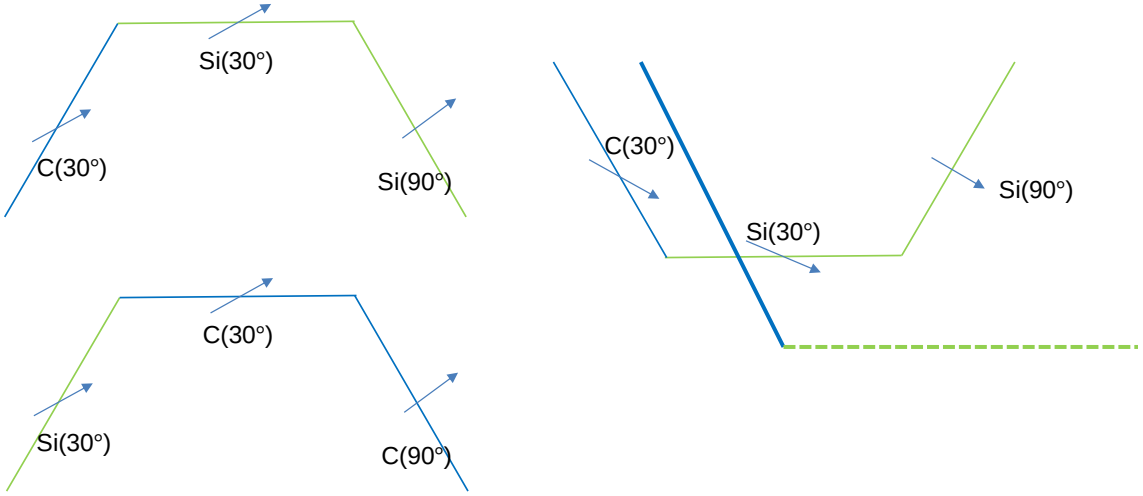

(a) Shape evolution of the dislocation loops.

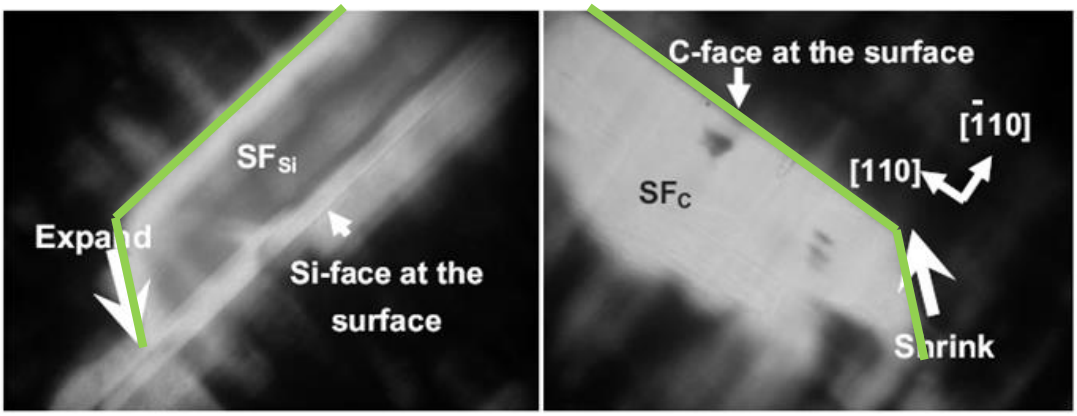

(b) Microscope image of stacking fault in 3C-SiC (Nagasawa *et al.*, 2006) with permission from the publisher John Wiley and Sons.

Figure 3.51 Schematic representation of shape evolution for the trapezoid stacking faults.

The stacking faults in the 4H-SiC are more complex than in the 3C-SiC for the existing of TED and TSD. Ha *et al*. (2003) observed two kinds of stacking faults by Optical emission microscopy. The images are shown in Fig. 3.52. The bright spot means a TED as shown in (a) developed into a pair of partial dislocations with same burgers vectors as shown in (b). This mechanism was also observed by (Maximenko and Sudarshan 2005a; Maximenko *et al.*, 2005b), Maximenko and the co-workers pointed out that the dislocation loop nucleated from the kink

segments of the TED, and both the Si-core and C-core 30° partial dislocations are electrically active. Our conclusion about the velocities of the partial dislocations that C-core has lower mobility than Si-core for a higher activation energy barrier explains the stacking fault expansion. The smooth outlines of the stacking faults also testified our dislocation morphology analysis in last section.

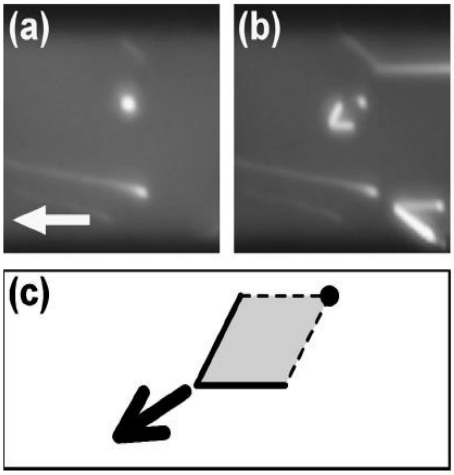

Figure 3.52 Optical emission microscopy images of stacking development in 4H-SiC (Ha *et al*., 2003). With permission from AIP Publishing LLC.

3.6 Conclusion

In this chapter, it is the first time to investigate the activation energy barriers of partial dislocations kink nucleation and migration in 3C-SiC by MD simulation. The activation energy barrier of kink nucleation and migration for each type of partial dislocations are calculated. Our results show that the Si-core partial dislocations have lower activation energy barriers than the C-core partial dislocations for both 30° and 90° partial dislocations. The conclusions agree with the experimental test.

Besides I also find that the partial dislocation with a larger distance between the dangling bond atoms along the dislocation line also has a higher activation energy barrier for both 30° and 90° partial dislocations. This could explain that why the C-core and Si-core have different mobility that which could be caused by their structure characters.

More importantly, I propose new models to explain the morphological character of different partial dislocation lines. I propose that the 30° partial dislocation prefer to be smooth because of the large activation energy difference between kink nucleation and kink migration.

And the 90 ° partial dislocations lines prefer to be zigzagged for the reason that the 90 ° partial dislocation lines have the possibility to migrate and nucleate simultaneously. On the other hand, dislocation velocity can be represented as a function of the activation energy barriers. I conclude that $V_{\mathrm{si}}^{90} > V_{\mathrm{c}}^{90} > V_{\mathrm{si}}^{30} > V_{\mathrm{c}}^{30}$. This conclusion is consistent with previous experiment data. In addition, the morphology of the stacking faults is discussed. The stacking fault formed by the half dislocation loop can develop into the trapezoid and triangle shape. The similar shapes of stacking fault had been observed by other researchers.

Chapter 4

4 Reaction path way analysis for shuffle-set perfect dislocation in silicon

4.1 Introduction

As mentioned in section 1.2.2, there are two dislocations types by defining which plane they are gliding on, i.e., the shuffle-set or the glide-set as shown in Fig. 4.1. The dashed green line shows the glide plane of the shuffle-set dislocation while the dashed black line shows that of the glide-set dislocation. The mobility for these two kinds of dislocations has been discussed for decades, such as which type is the dominate one under the lower temperature and high stress; is there any transition between these two types. Compared with the glide-set dislocation, fewer researches have reported for the non-dissociated shuffle-set dislocation. The non-dissociated shuffle-set dislocation includes the screw dislocation and the 60° perfect dislocation.

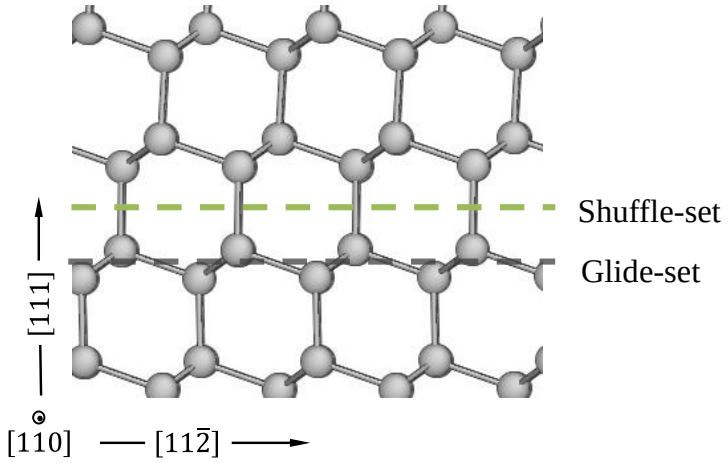

Figure 4.1 Illustration of the Shuffle-set and glide-set dislocation in silicon.

For 60° perfect dislocation, Godet *et al*. (2004) performed the simulation of the dislocation nucleation from a surface step with serval empirical potentials including SW, EDIP and Tersoff in a slab atomic model. Latter, an *ab initio* method had been employed for the dislocation nucleation from a surface step with a two dimension model (Godet *et al*., 2006). The dislocation migration process had been investigated which indicated that the surface step can reduced that dislocation nucleation barrier. In his study, the 60° perfect dislocation can be produced for both compression and tension state while no screw dislocation had been observed. A 3D model of the shuffle-set dislocation loop which was nucleated from the sharp corner had been performed by MD simulation (Izumi and Yip, 2008). The dependence of the activation energy barriers on shear strain were represented by reaction pathway analysis. The same model was applied by Shima *et al*. (2010) for solving the controversy between glide-set and the shuffle-set dislocations. Shima and the co-workers found a cross point of the glide-set and the shuffle-set curves which represent the dependences of the activation energy on shear stress. The cross point indicated that the shuffle-set dislocation was nucleated under high stress with low temperature, and the glide-set dislocation could be nucleated at high temperature and low stress (Shima *et al*., 2010). Their conclusion seemed agreed with Duesbery's theory (Duesbery and Joos, 1996). Pizzagalli *et al*. (2008b) investigated the activation energy barriers of the kink nucleation and migration for the screw dislocation by theoretical study. The EDIP potential is applied for the representation of the silicon. By calculating of the activation energy barriers, he pointed out that the kink formation energy is around 0.9eV to 1.36eV while the kink migration energy is 50 meV (Pizzagalli *et al*., 2008b). The results implied that, since the screw dislocation is nucleated, the

kink can migrate freely for the lower energy barrier. Moreover, the result also showed that the screw dislocation is more mobile than the 30° glide-set partial dislocations for the whole stress region (Cai 2001; Rabier *et al*., 2010) that is contradict to the Duesbery's theory.

Even though, there are still something unclear even the controversy about the shuffle-set dislocations. In addition, the kink nucleation and migration of shuffle-set 60° perfect dislocation have not been reported yet. Therefore, for a better understanding of the shuffle-set dislocation motion, the reaction pathway analysis is applied on the dislocation mobility.

4.2 Atomic model

Our simulation model is schematically shown in Fig. 4.2. The coordinate axes are [11-2], [-110], [111] for X, Y, Z directions. The model size is 23.95×13.82×9.4nm^3, including 38800 atoms. The dislocation line is on the slip plane (111), and the burgers vector is $b_{60} = a_0[01\bar{1}]/2$. The shear stress σ_{xz} was applied by displacing top and bottom atoms along the x and –x directions. Periodical boundary condition is applied in all the directions.

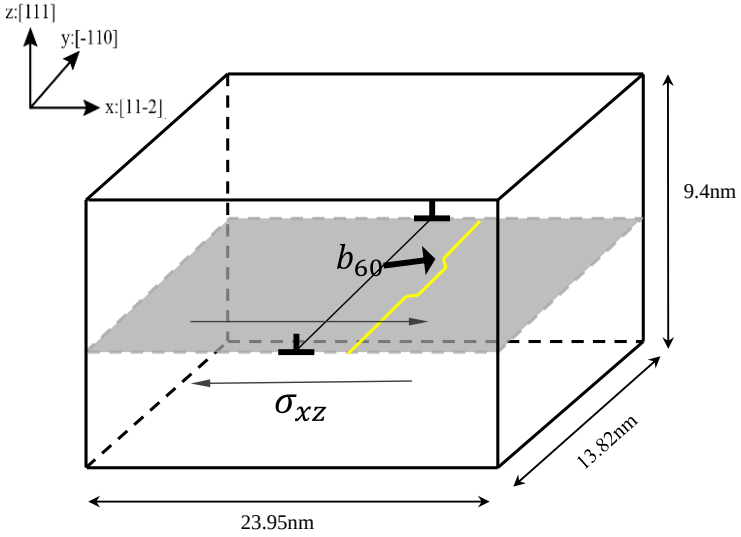

Figure 4.2 Schematic representation of the simulation model for shuffle-set dislocation in silicon.

In our simulation, three kinds of potentials are used to represent the dislocation structure including SW, EDIP and Tersoff. Three types of possible dislocation cores are obtained by moving part of lattice along the burgers vector as shown in Fig .4.3.

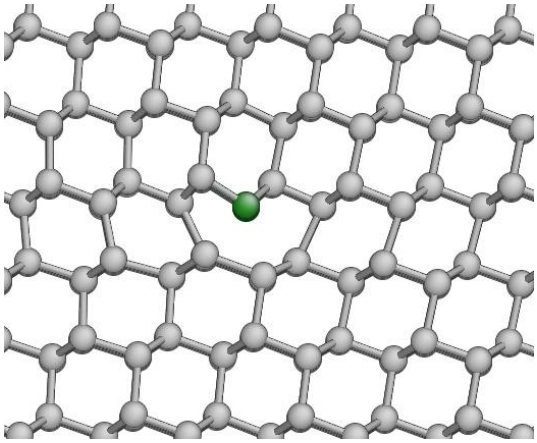

(a) S1

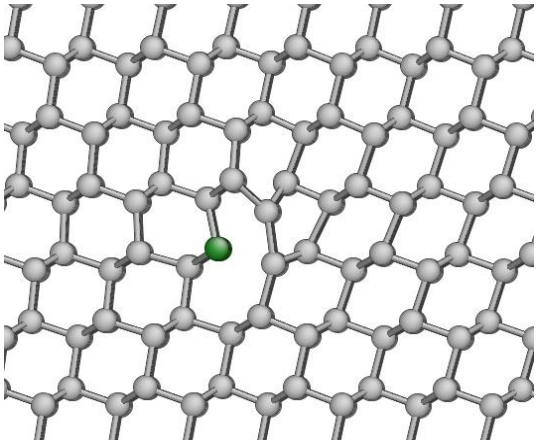

(b) S2

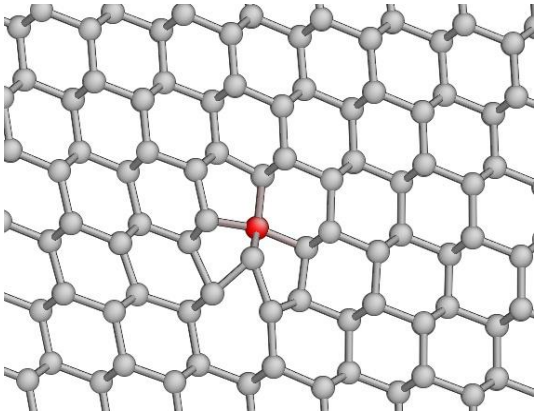

(c) S3

Figure 4.3 Three possible shuffle-set dislocation core structures. The gray balls represent the silicon atom with four coordinates while the green and red balls represent the atoms with three and five coordinates, respectively.

Pizzagalli *et al*. (2009b) reported that there are three kinds of possible shuffle-set dislocation core structures. The mobile S1 type, and the glissile S2 and S3. Moreover, Zhong *et al*. (2012) showed a new core structure named as S4 by DFT calculation. Similar dislocation core structures are obtained in our study. SW potential can only create the dislocation structure with S1 while the Tersoff and EDIP reproduce all the three kinds of core structures. Then, the kink structures in these dislocation core types with different potentials are testified. The kink on the dislocation line is involved with over fold atoms for SW and Tersoff potentials as shown in Fig. 4.4. Therefore, the EDIP potential that which is designed for describing the defects in silicon is chosen for the kink migration and nucleation analysis.

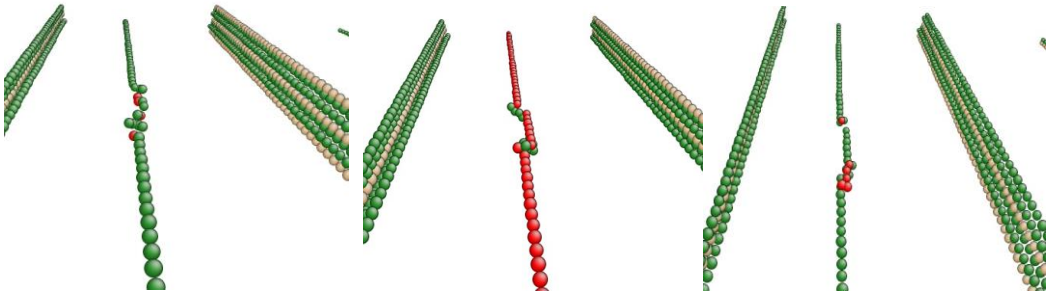

(a) S1 by SW. (b) S2 by Tersoff. (c) S3 by Tersoff.

Figure 4.4 Kink structures with over-fold atoms that represented by SW and Tersoff potentials. The gray atom balls are invisible here for a better comparison of the kink structures.

4.3 Simulation results and discussion

The kink structure in S1 type is shown in Fig. 4.5. In image (a), the red balls are the five-fold silicon atoms along the dislocation line. Four layers of atoms are used for the representation of the dislocation structure, and these layers are illustrated in image (b) marked by dashed black line. The dislocation core structure in image (b) is different with core structure shown in Fig. 4.3 (a) because of different band visualization condition. Atomeye (Li, 2003) is used to visualize the structure configuration, and in the upper image in Fig. 4.6., 2.50 Å is set up to decide whether the Si-Si bond will be shown in the visualization while 2.58 Å is set up for visualization in the bottom image.

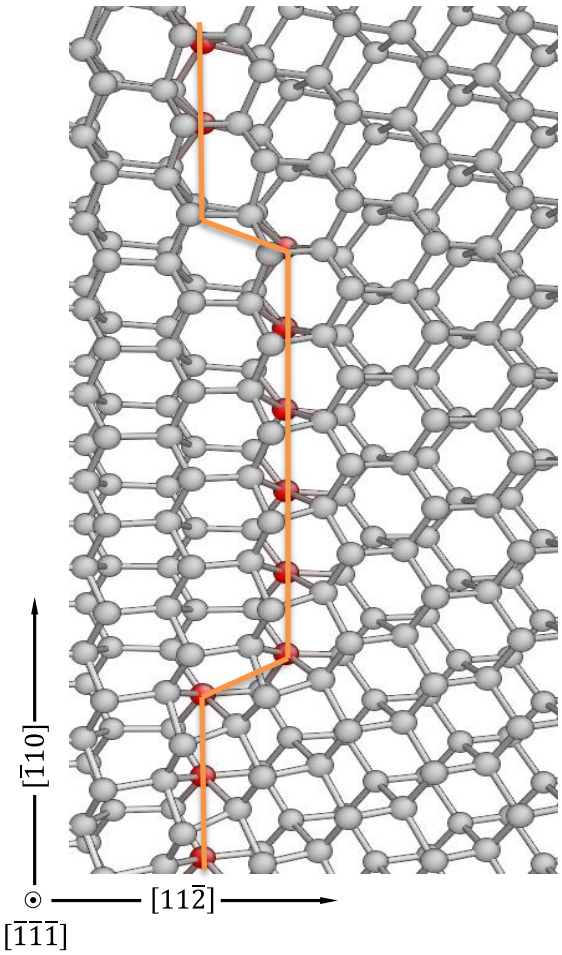

(a) The projection image of dislocation structures on (111) plane.

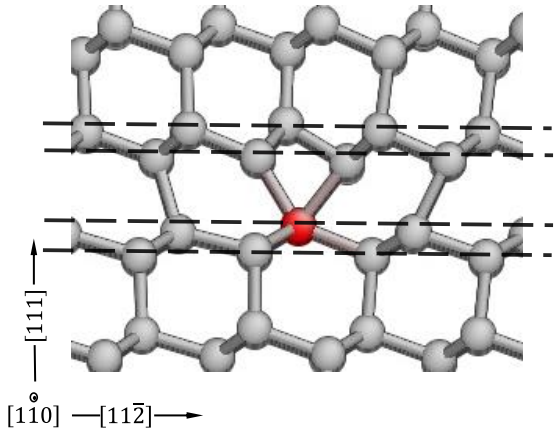

(b) Side view of the dislocation core.

Figure 4.5 Kink structure of the S1 dislocation core. The dislocation in (a) involves four layers of atoms which are marked by dashed black lines in (b). Orange line shows the kink along the dislocation line.

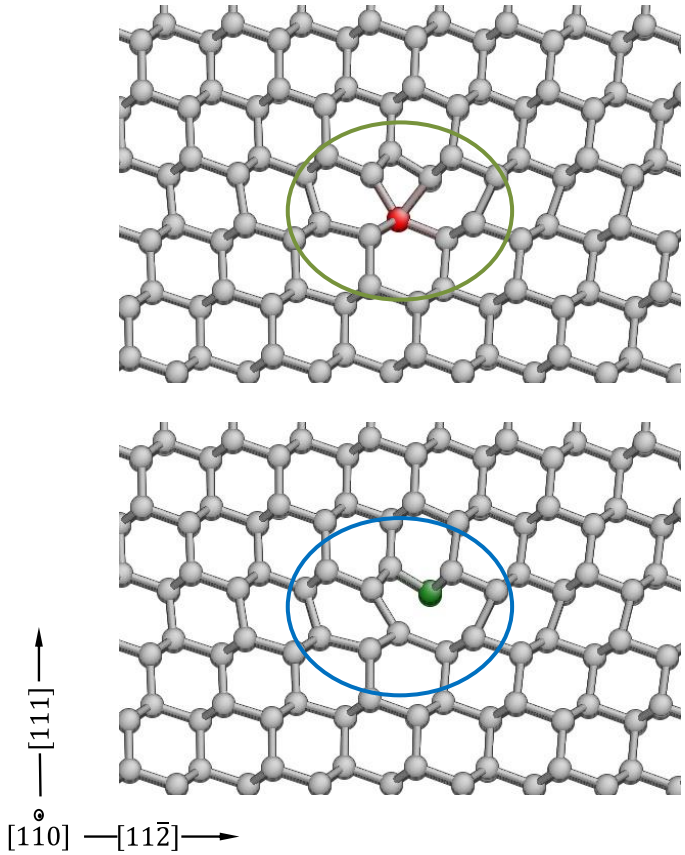

Figure 4.6 Different types of visualizations for S1 dislocation core. The top and bottom images show the same dislocation core. For the top image, 2.50 Å is set up to decide whether the Si-Si bond will be shown in the visualization while 2.58 Å is set up for the bottom image.

The kink with S1 dislocation core structure is symmetric. The activation energy barriers are the same for the left side and right side. The reaction pathway of the kink migration is shown in Fig. 4.7. During the kink migration path, an atom marked by the yellow circle is moving along the burgers vector. The process is completed by breaking a Si-Si bond and forming a new one. The minimum pathways of the kink migration for S1 core under different shear strain are shown from Fig. 4.8 to Fig. 4.13. The horizontal axis is the reaction coordinates and the perpendicular axis is the activation energy. The peak in the curve presents the activation energy barrier of the migration process. The dependence of activation energy on the shear strain is shown in Fig. 4.14. The activation barrier decreases when the shear strain increases.

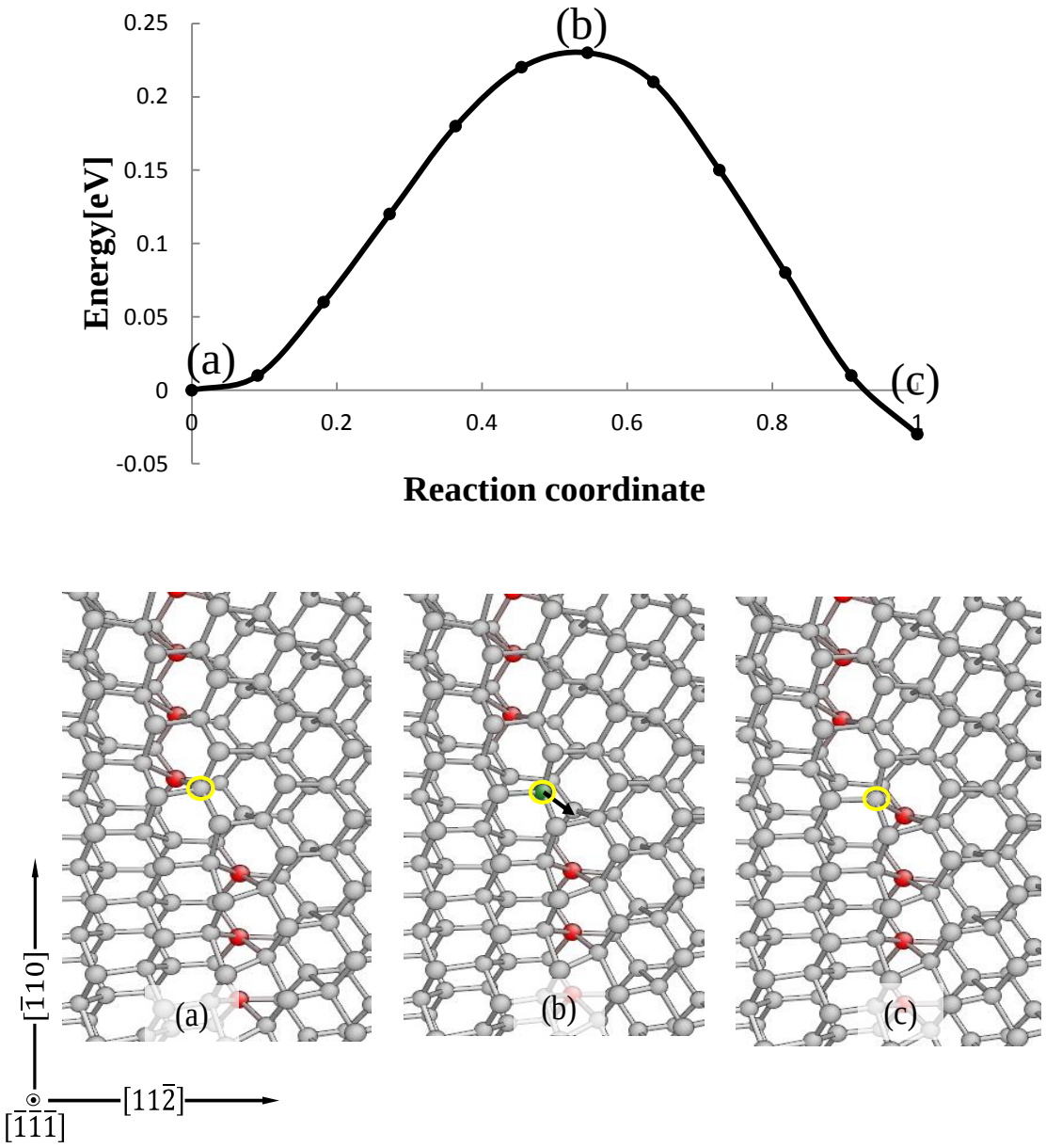

Figure 4.7 Kink migration pathway for S1 shuffle-set dislocation line with shear strain 2.84%. The moving atom is marked by the yellow circle and the moving direction is marked by the small black arrow.

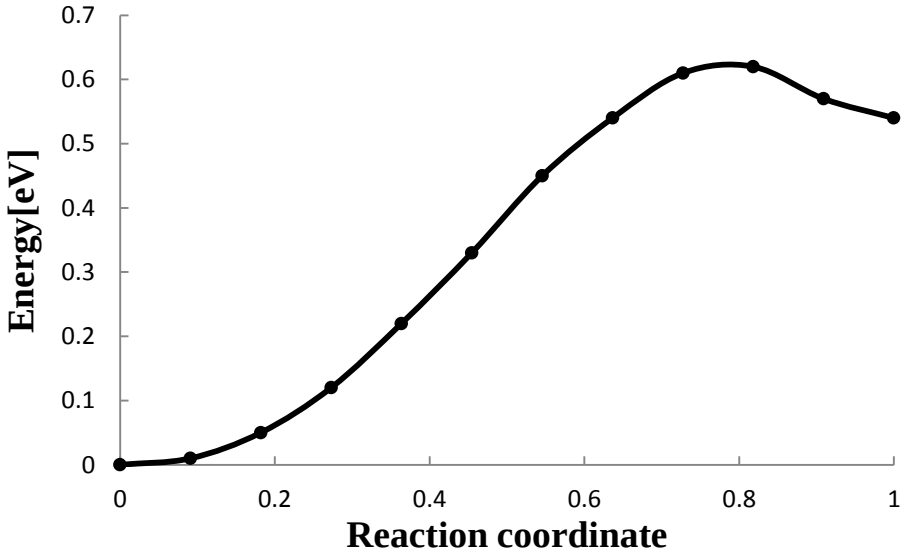

Figure 4.8 Minimum energy path for kink migration of S1 core under shear strain 0.945%.

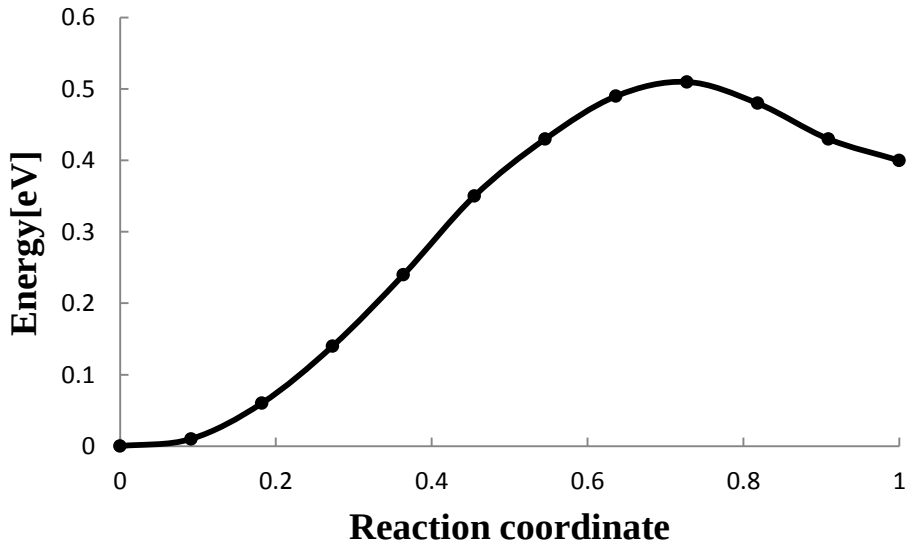

Figure 4.9 Minimum energy path for kink migration of S1 core under shear strain 1.42%.

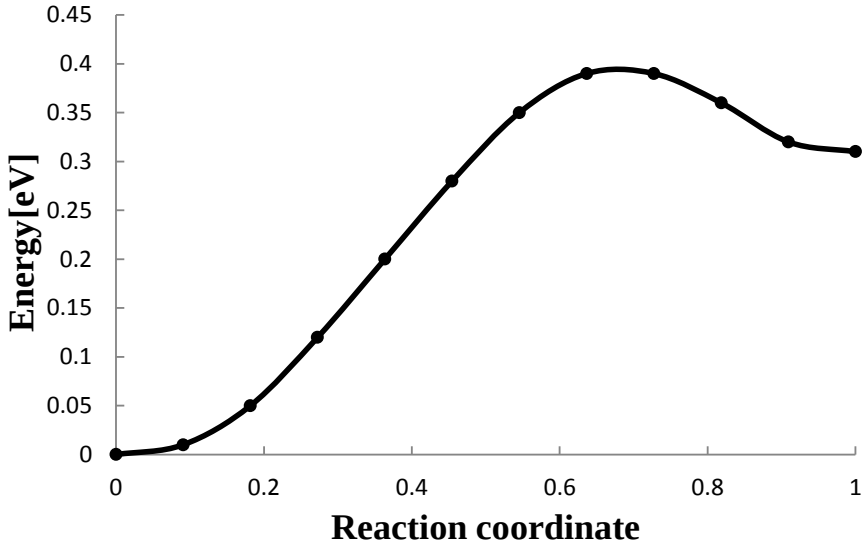

Figure 4.10 Minimum energy path for kink migration of S1 core under shear strain 1.89%.

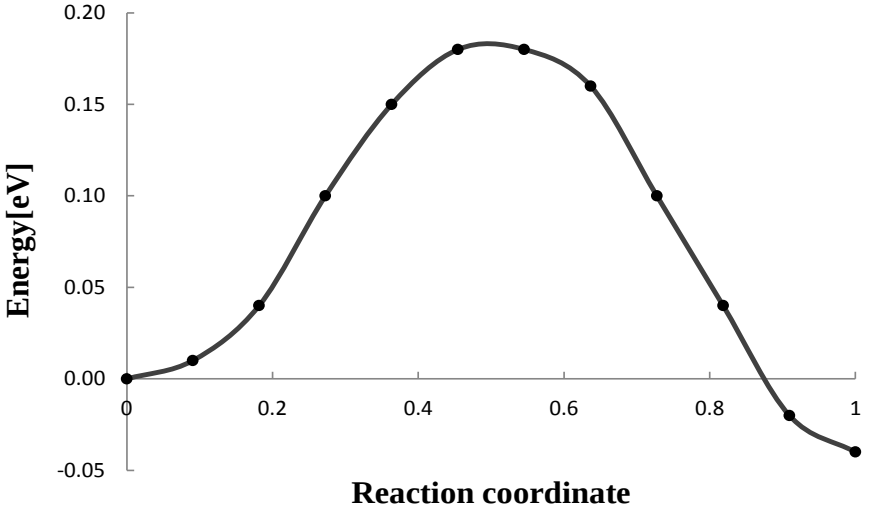

Figure 4.11 Minimum energy path for kink migration of S1 core under shear strain 2.84%

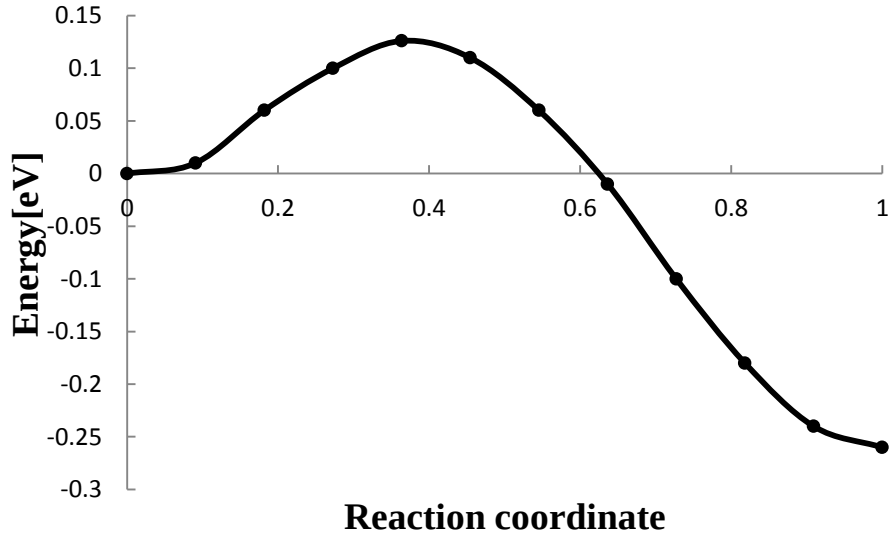

Figure 4.12 Minimum energy path for kink migration of S1 core under shear strain 3.78%

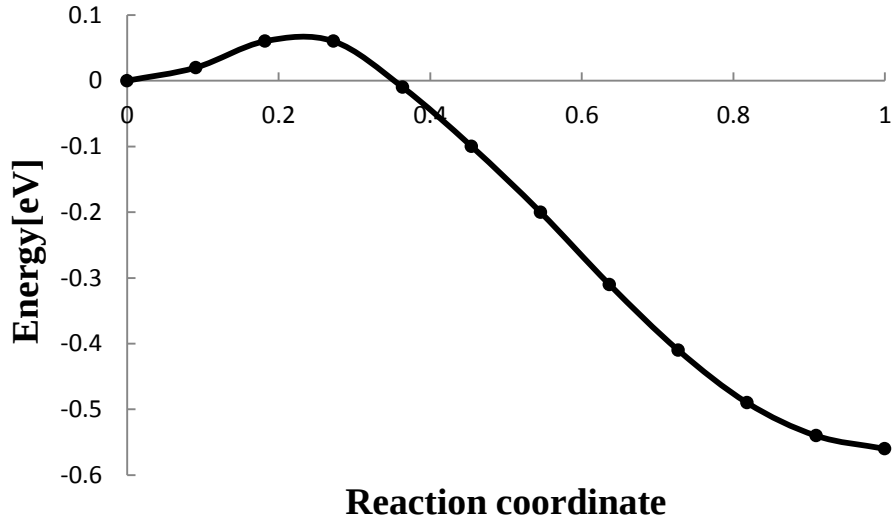

Figure 4.13 Minimum energy path for kink migration of S1 core under shear strain 4.73%

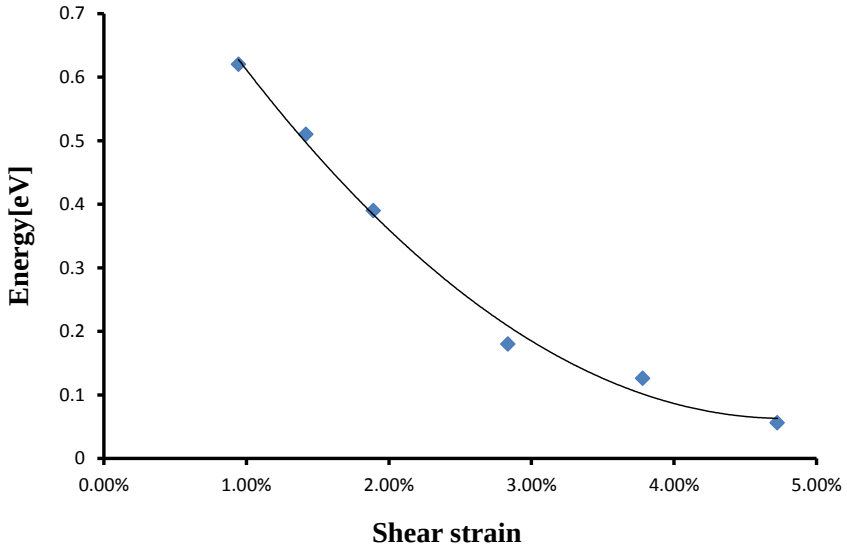

Figure 4.14 Dependence of activation energy barrier on shear strains for kink migration with S1 core shuffle-set dislocation.

The reaction pathway of the kink nucleation is shown in Fig. 4.15. The kink pair is forming by the moving of the marked atoms along the burgers vector simultaneously. The minimum energy path ways for the kink nucleation with different strain are shown from Fig. 4.16 to Fig. 4.21. The dependence of kink nucleation activation energy barriers on shear strain is represented in Fig. 4.22. The activation energy barriers decrease when the shear strain increases.

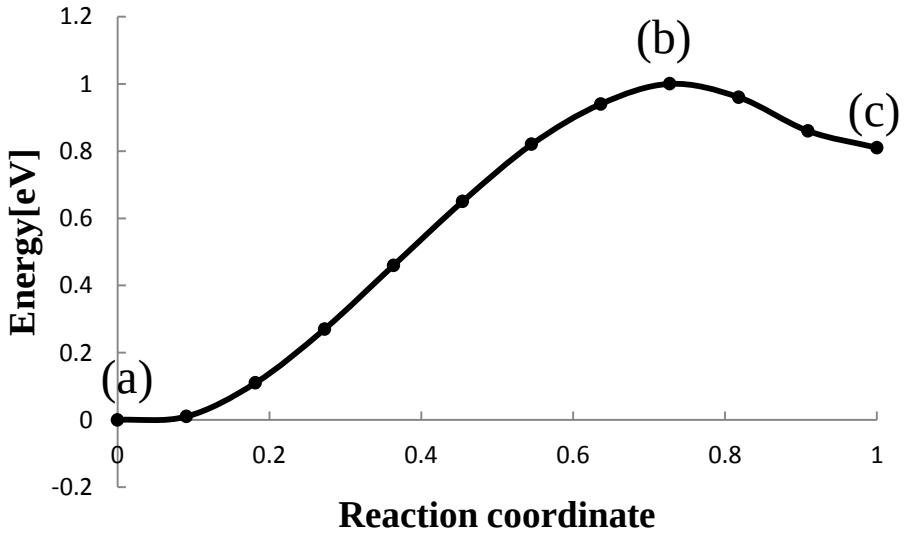

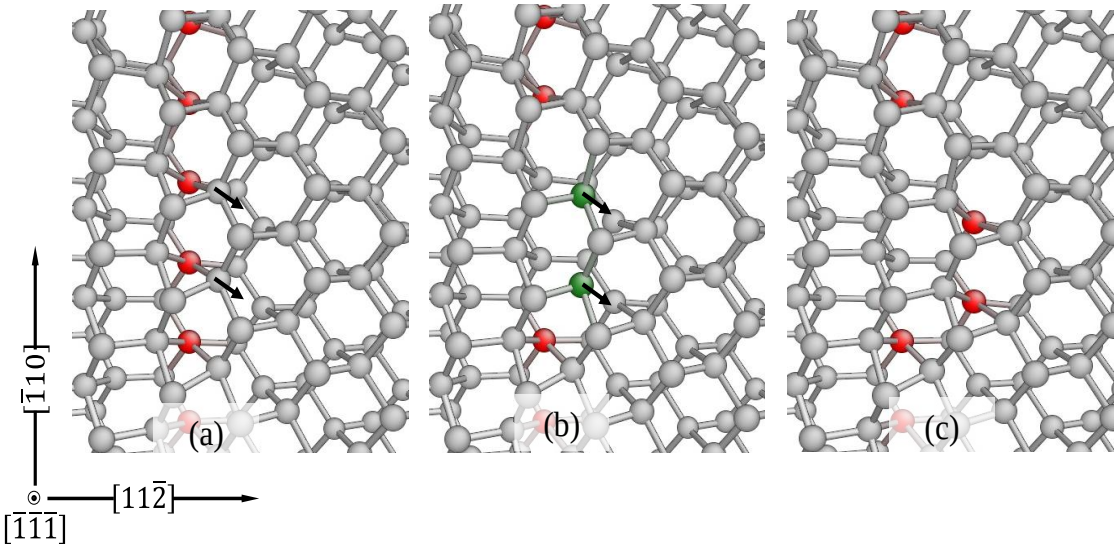

Figure 4.15 Kink nucleation pathway for S1 shuffle-set dislocation line. The moving direction of the atom is marked by the small black arrow. These two atoms are moving simultaneously during the kink nucleation with 2.84% shear strain.

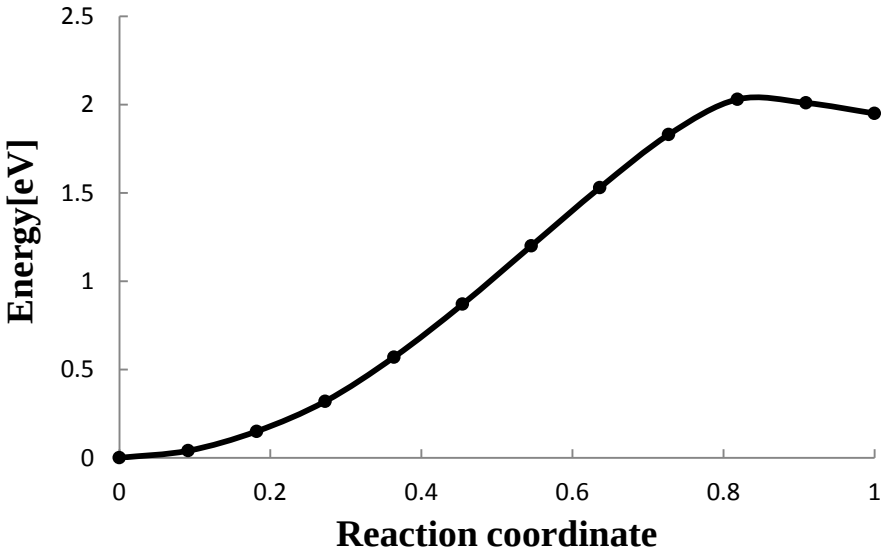

Figure 4.16 Minimum energy path for kink nucleation of S1 core under shear strain 0.945%.

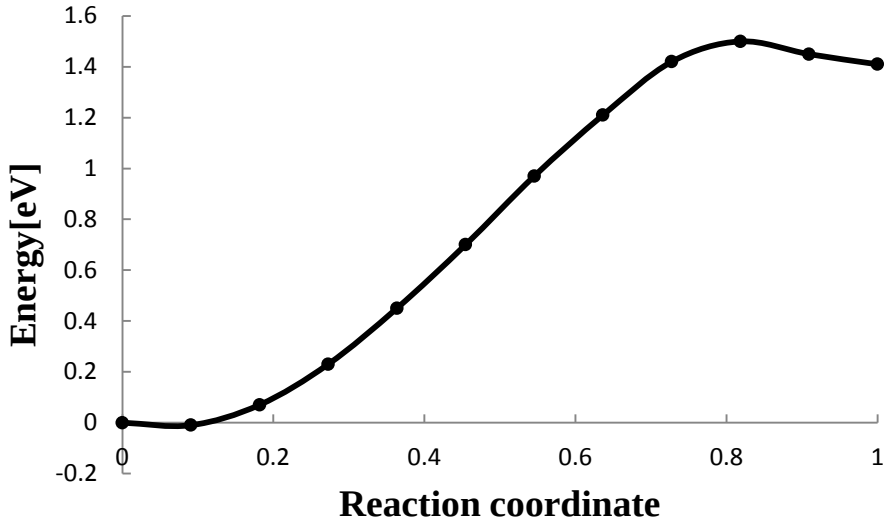

Figure 4.17 Minimum energy path for kink nucleation of S1 core under shear strain 1.89%.

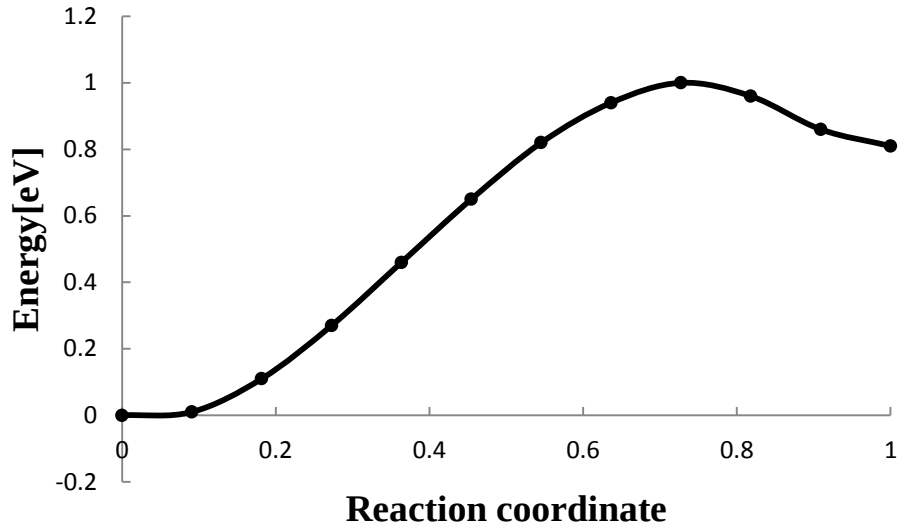

Figure 4.18 Minimum energy path for kink nucleation of S1 core under shear strain 2.84%.

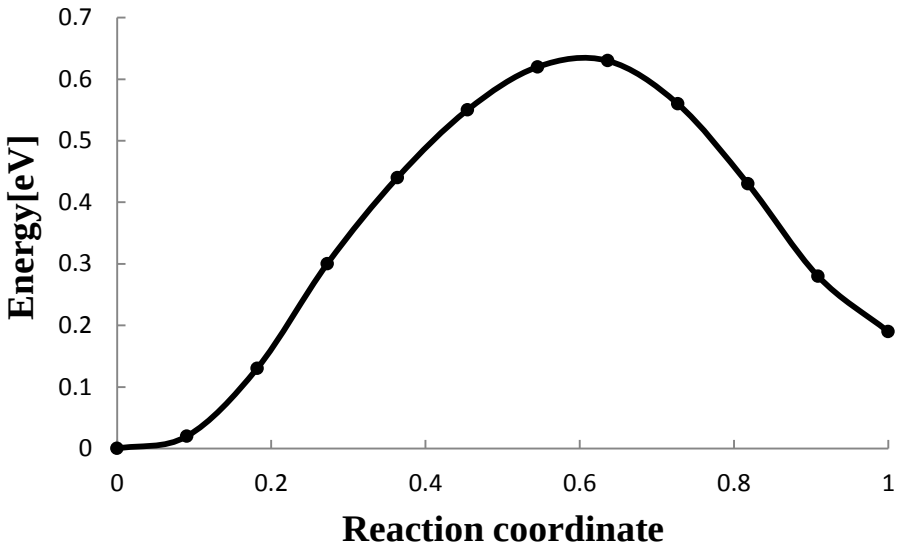

Figure 4.19 Minimum energy path for kink nucleation of S1 core under shear strain 3.78%.

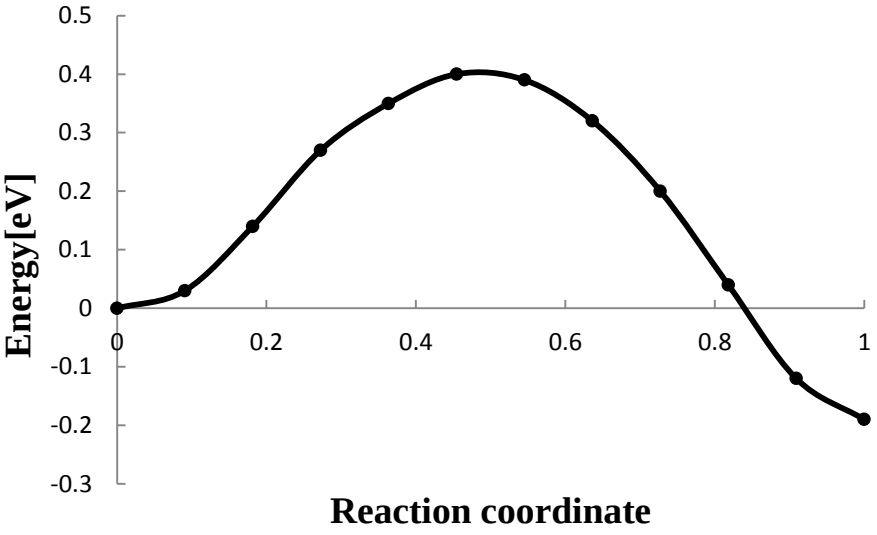

Figure 4.20 Minimum energy path for kink nucleation of S1 core under shear strain 4.25%.

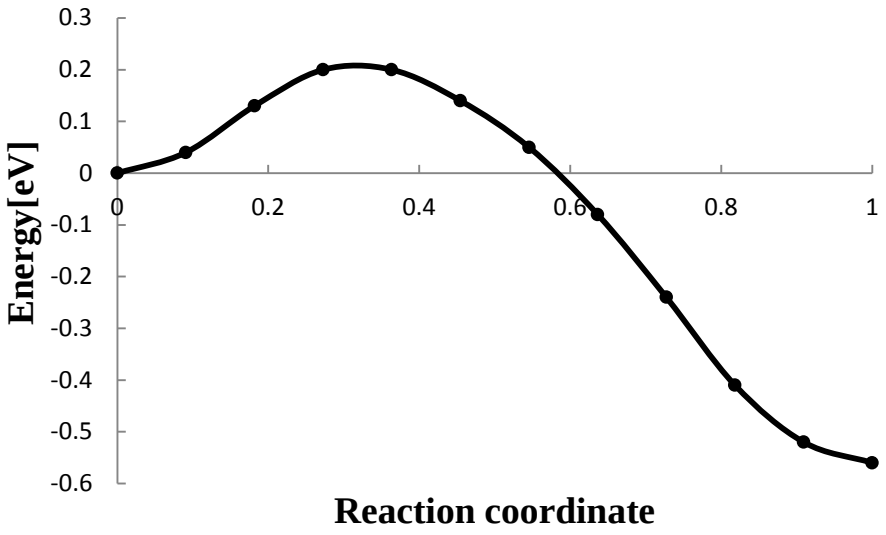

Figure 4.21 Minimum energy path for kink nucleation of S1 core under shear strain 4.725%.

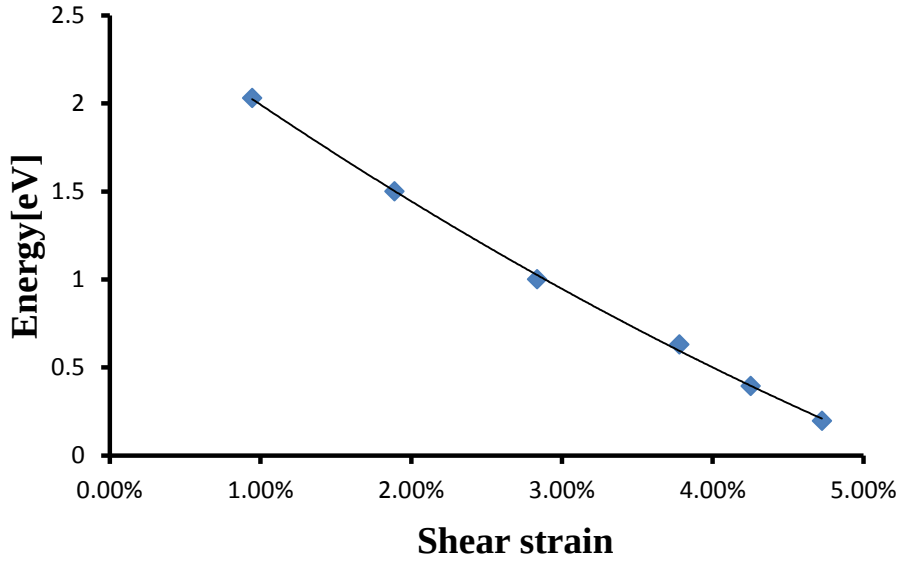

Figure 4.22 Dependence of activation energy barrier on shear strains for kink nucleation with S1 core shuffle-set dislocation. The black line is the fitting curve by polynomial method.

Moreover, the kink migration for both sides also has been investigated. An interesting phenomenon is observed that the activation energy barrier of the kink migration for both sides is around two times than that of the one side kink migration. Moreover, similar to kink nucleation process, the atoms are moving simultaneously. The kink pair migration minimum energy pathway and the reaction pathway are shown in Fig. 4.23 and Fig. 4.24. The activation energy barriers of the kink migration for the both sides and only one side are 0.24eV and 0.126eV under the shear strain 3.78%, respectively. For the kink nucleation and kink migration for two sides, there is no local minimum energy spot. This may imply that the shuffle-set perfect dislocation kink propagation mechanism is different with the one in the dislocation theory. The nearby atoms along the dislocation line have the possibility to be nucleated or migrated at the same time with a high enough activation energy. This could induce that only small dislocation segment can be observed in the TEM. In addition, the activation energy barriers of kink migration for both sides have also been calculated under the shear strain 1.89% and 2.84%. They are 0.84eV and 0.43eV for the shear strain 1.89% and 2.84%, respectively.

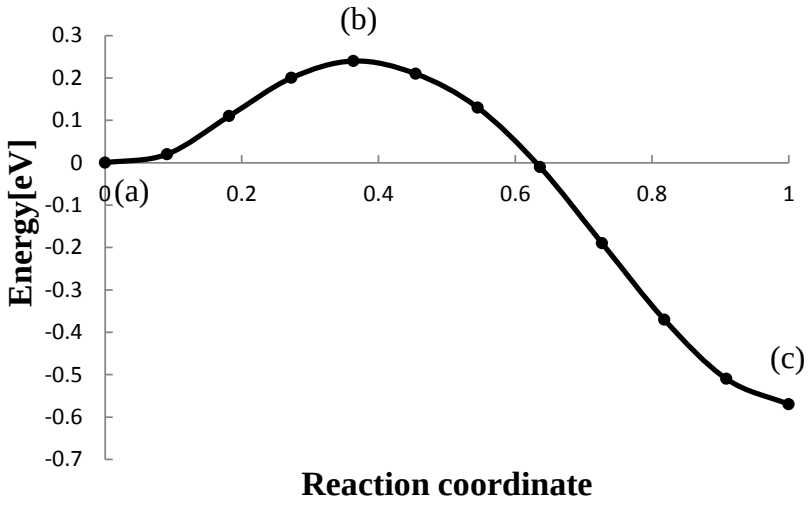

Figure 4.23 Minimum energy pathway for the S1 dislocation core structures kink migration with both sides under shear strain 3.78%. The atomic configurations for (a) (b) (c) are shown in Fig. 4.24.

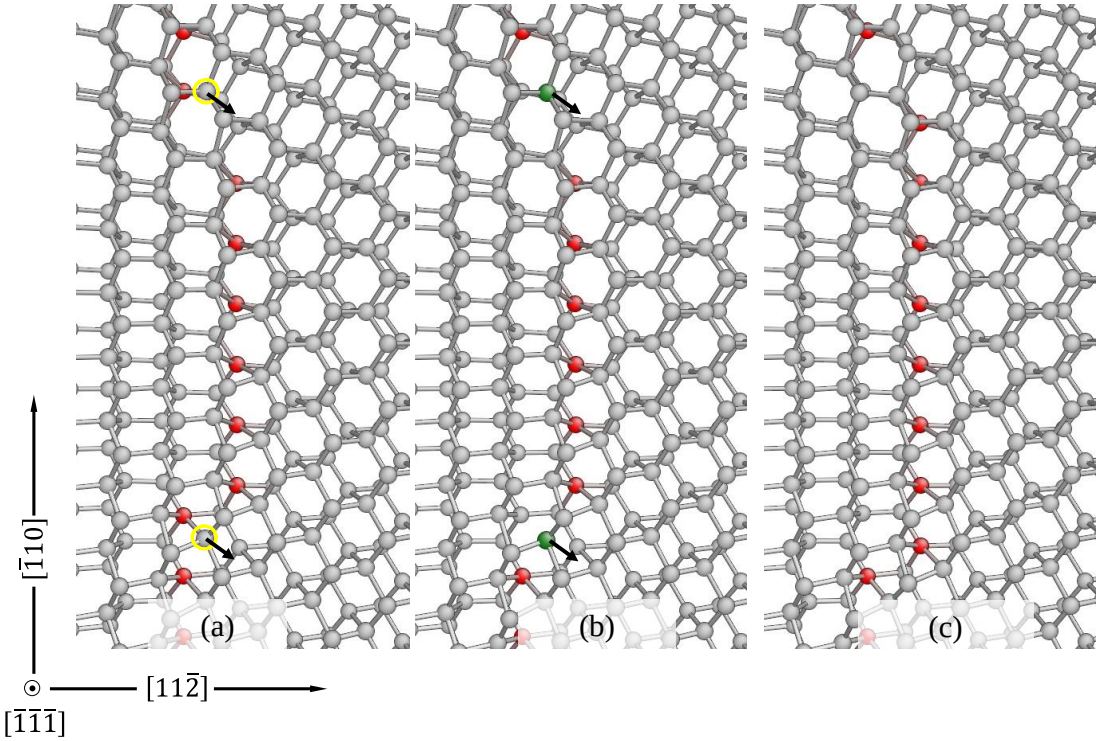

Figure 4.24 Kink migration path for both sides with S1 dislocation core. The moving atoms are marked by yellow circles while the moving direction is shown by black arrows. (b) is the saddle point atomic configuration.

The S2 dislocation core structure is obtained by increasing the shear strain. When the shear strain is large than 5%, the S1 dislocation core structures along the dislocation line are changing into the S2. These transformations for these cores are independent. In our simulation, the transformation begins from 5% shear strain and is accomplished when the shear strain is greater than 12.5%.

Considering the asymmetrical structures of the S2 dislocation line, there are LK (left kink) and RK (right kink) as shown in Fig. 4.25. The RK is complicate that a five-fold atom involved. As shown in Fig. 4.26., the migration path of RK involving the bond breaking and forming for both glide-set and shuffle-set. The definition of shuffle-set and glide-set bonds is illustrated in Fig. 4.27. In the RK migration, the major moving atoms are marked by yellow circles and their moving directions are shown by the black arrows. Moreover, the LK migration process is shown in Fig. 4.28. Only the shuffle-set bond breaking and forming in response, and the activation energy barrier for the LK migration is 0.05 eV under the shear strain 14.175%. With the same shear strain the activation energy barrier of the RK migration is above 1eV. That indicate the S2 dislocation line is difficult to move even with such a large shear strain.

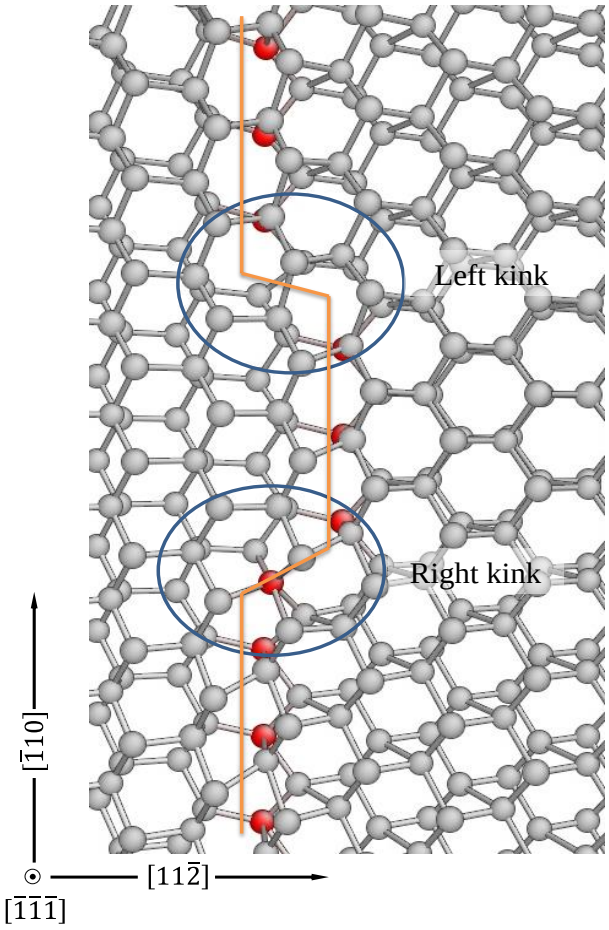

Figure 4.25 Kink structure with S2 dislocation core.

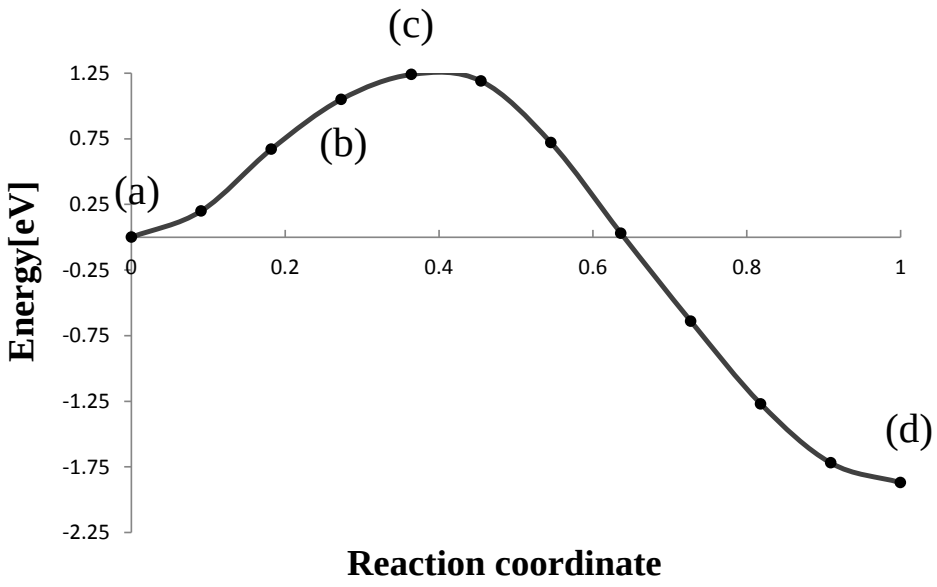

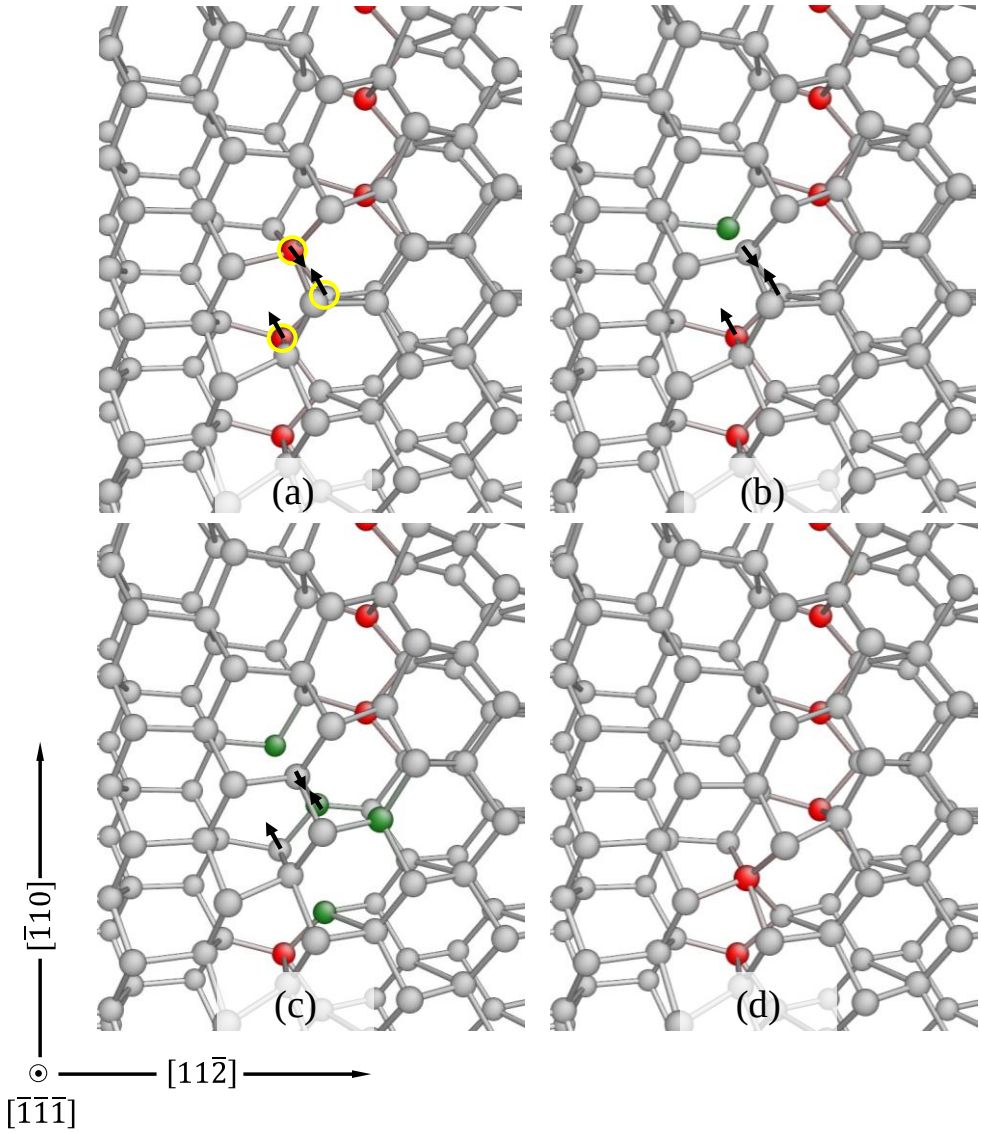

Figure 4.26 Minimum energy pathway of right kink migration process for S2 dislocation core. (c) is the saddle point atomic configuration.

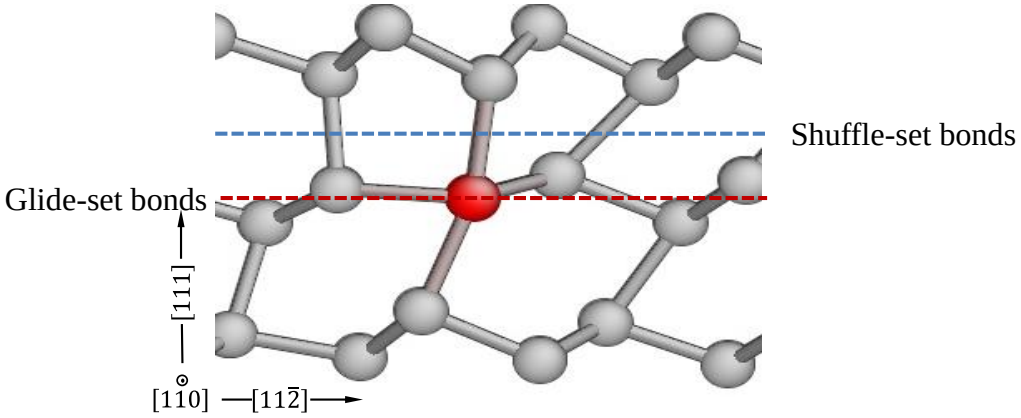

Figure 4.27 Representation of Shuffle-set and glide-set bonds in silicon.

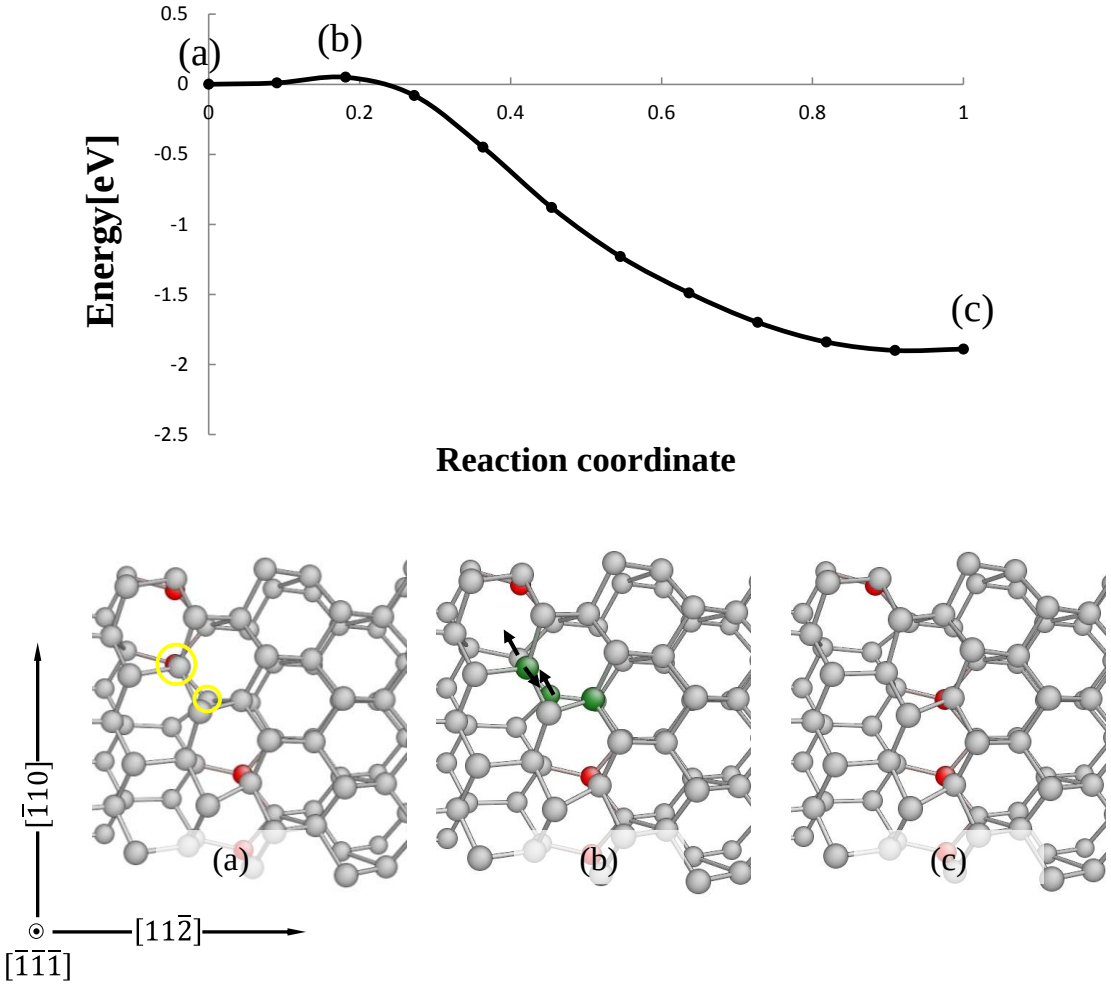

Figure 4.28 Minimum energy pathway of left kink migration process for S2 dislocation core. (b) is the saddle point configuration.

In addition, the kink nucleation process of the S2 dislocation core structures is also been investigated. Our simulation results show that there are two kinds of nucleated kink pair in S2 dislocation kink nucleation for different shear strain. As shown in Fig. 4.29., two possible configurations of the nucleated kink pair with S2 dislocation core are represented. The structure in (a) is obtained with a shear strain around 11.75%. The nucleated kink pair is in the type of S1 dislocation core. The configuration (b) is given with a shear strain 16.45%, and the nucleated kink pair is in the type of S2 dislocation core. This phenomenon could be caused by the interaction of initial kink pair. It also indicate that the S2 dislocation core is stable than the S1 type. Fig. 4.30 shows the minimum energy pathway of S2 nucleated with S1 kink pair structures.

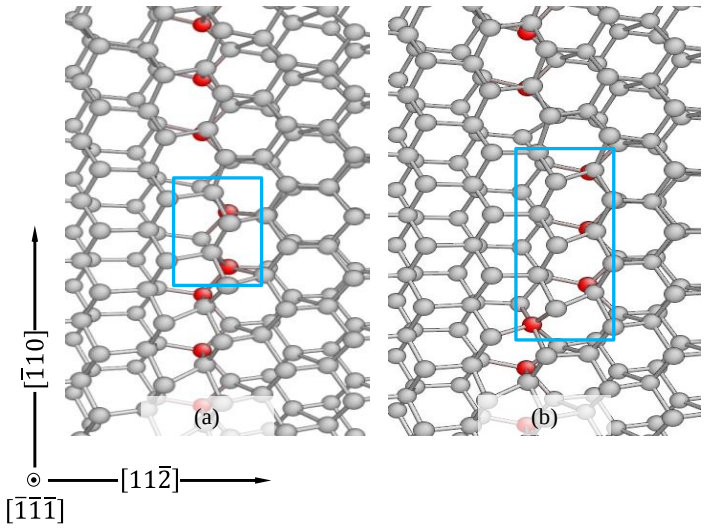

Figure 4.29 Two possible configurations of the nucleated kink pair with S2 dislocation core. Image (a) shows the nucleated kink pair with S1 core structure while (b) shows the nucleated kink pair with S2 core structure.

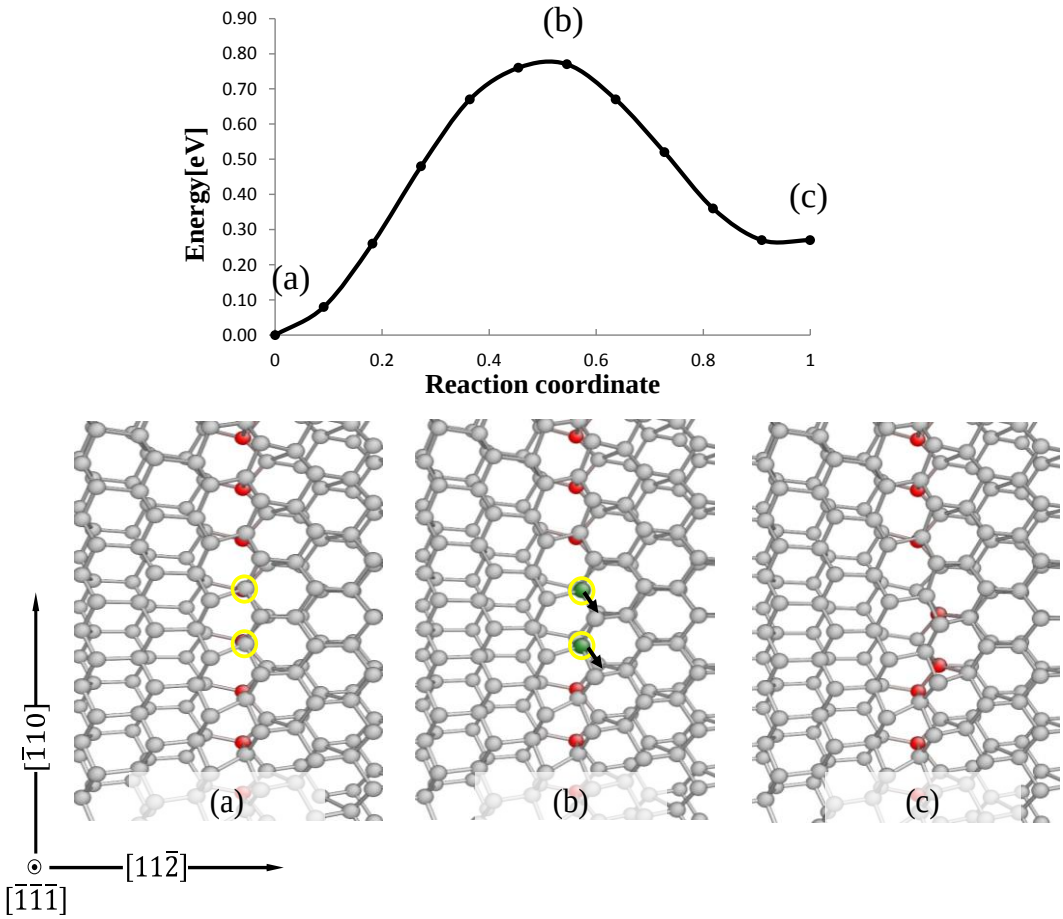

Figure 4.30 Minimum energy pathway of S2 dislocation nucleation process with the shear strain of 11.75%.

The S3 dislocation core structures can also been obtained in our simulation with applying an opposite shear strain on the S2 dislocation core structures. The shear strain of the whole model is still positive. However, when it comes to the kink structures, the over fold atoms appeared along the dislocation line which makes it unavailable for the calculation of the kink migration and nucleation.

For the S1 shuffle-set dislocation, the activation energy barrier decreases when the shear strain increases. Moreover, the S1 shuffle-set dislocation kink nucleation can be trigged with a shear strain larger than 5% for a low kink nucleation and migration barriers. This conclusion is consistent with the study by Izumi and Yip (2008). Izumi and Yip pointed out that the resolved strain is about 5.1% though the simulating of the kink nucleation from a sharp corner while the resolved strain is 6.2% (Rabier *et al*., 2010) for a shuffle-set half dislocation loop nucleated from a surface step (Godet *et al.,* 2009). The difference between the experiment data and the simulation results may due to that the material propriety is different in nanoscales (Zhu *et al*., 2009). Moreover, by comparing with the simulation of the shuffle-set screw dislocation (Pizzagalli *et al*., 2008b), the shuffle-set screw dislocation seemed has a higher mobility than the shuffle-set perfect dislocation for a lower activation energy barriers. I also find that the activation energy barriers of the two sides kink migration is nearly two times than that of the one side kink migration. The kink nucleation pair is accomplished by two atoms moving simultaneously. These imply that the S1 dislocation line could move without the kink pair function. This may explain the missing of long dislocation segment in the experimental studies. Therefore, I are wondering whether it is possible that the dislocation loop propagation and the movement of shuffle-set perfect dislocation segment have different mechanisms. Rabier *et al*. (2013) also pointed out that dislocation movement at low temperature does not show the kink features. More experimental data and simulation result data are needed for solving this problem.

The S2 dislocation core can be obtained by the increasing the applied shear strain larger than 5%. When the shear strain is large than 5%, the S1 core structure is changing into S2 core structure. During this strain region, the dislocation moves as S1 types. This conclusion agrees with Pizzagalli *et al*. (2009a) that S2 is transformed from S1 and be more stable than S1 core. Our simulation also shows that the kink with S2 core structure is asymmetric. The LK has a lower activation energy barrier than RK. I believe RK can be a pinned point during the S2 dislocation kink migration. More importantly, the investigation of the kink migration for RK

shows that both the shuffle-set and glide-set bond breaking and forming are involved. This may imply that there could be a possibility that the shuffle-set dislocation core can translated into a glide-set dislocation core. Besides, the high activation energy barrier of the RK migration in S2 also indicates that this shuffle-glide transition could only appear in the high temperature. These experimental data provided by Saka *et al*. (2006), Izumi *et al*. (2010) and Okuno and Saka (2013) also showed that the shuffle-glide transitions were observed above 400℃.

For S3 dislocation core, Pizzagalli *et al*. (2009a) and Zhong *et al*. (2012) obtained this structure by applying an opposite strain on S2 and by heating S1 to 200K, respectively. In our simulation, the S3 dislocation core structures are always involved with the S2 dislocation core structures. Moreover, the S3 dislocation core always comes with highly distorted lattice.

4.4 Conclusion

In this chapter, the relation between the shuffle-set dislocation core and the shear strain has been discussed. Our simulation results show that the S1 dislocation can be nucleated by a shear strain larger than 5%. During the shear strain from 5% to 12.5%, the dislocation can move as the S1 core kink nucleation and migration and the S1 dislocation core is in process of transforming into S2. The S2 dislocation core structures begin to appear along the S1 dislocation line since the shear strain is larger than 5% shear strain. S2 dislocation core structures became into the dominate one with a shear strain region from 12.5% to 17.5%. I also found that the activation energy barriers of the two sides kink migration is nearly two times than that of the one side kink migration. The kink nucleation pair is accomplished by two atoms moving simultaneously. These interesting phenomena could be response to the missing long segment in the experiment. I am guessing that whether it is possible that the dislocation propagation of shuffle-set perfect dislocation segment have different mechanisms. More information about the shuffle-set dislocation core structure is necessary for the further study.

More importantly, a new possible shuffle-glide core transition mechanism has been proposed. During the RK migration process in S2 dislocation core, both the shuffle-set and glide-set bond breaking and forming are involved. This may imply that there could be a possibility that the shuffle-set dislocation core can translated into a glide-set dislocation core. And the high activation energy barrier during the migration also indicates that this transition could only happen with a high temperature, which agrees with the precious experimental

observation that the glide-shuffle transition was observed above 500℃. S3 dislocation line is not considered here for the bad representation of kink structures.

Chapter 5

5 Conclusion and future work

5.1 Conclusion

With the purpose of a better understanding the dislocation mobility in semiconductor materials, the reaction pathway analysis is performed to identify the activation energy barriers of kink nucleation and migration for the partial dislocations in 3C-SiC and shuffle-set perfect dislocation in Silicon.

In chapter 3, it is the first time to investigate the activation energy barriers of the four kinds of partial dislocations kink nucleation and migration in 3C-SiC by MD simulation. The simulation results show that Si-core partial dislocation has higher mobility than C-core partial dislocation. Then the partial dislocation morphology is discussed by the activation energy difference. I propose that the 30° partial dislocation lines prefer to be smooth while the 90° partial dislocation lines prefer to be zigzagged for the reason that the 90° partial dislocation lines have the possibility to migrate and nucleate simultaneously. Furthermore, the relation between the activation energy barriers in dislocation motion and the dislocation velocity can be

established by an empirical function. I conclude that $V_{si}^{90} > V_{c}^{90} > V_{si}^{30} > V_{c}^{30}$. This conclusion is consistent with previous experiment data. With regarding that the stacking faults are bounded by partial dislocations, the morphology of the stacking faults is also discussed. The stacking fault formed by the half dislocation loop can develop into the trapezoid or triangle shape. The similar shapes of stacking fault were observed by other researchers.

Chapter 4 is devoting to provide more evidence for solving this controversy about the shuffle-set and glide-set dislocation in silicon that which has been studied for decades. In this chapter, the relation between the shuffle-set dislocation core and the shear strain has been discussed. The S1 dislocation is domain in the shear strain from 0% to 5%. The resolved shear strain of the S1 core dislocation is around 5%, at which the activation energy barrier is almost zero. The conclusion of the resolved shear strain is close to the previous studies. When the shear strain keeps increasing, the S1 dislocation migrates and part of core structure along the dislocation line transforms to S2. This transformation is completed when the shear strain is larger than 12.5%. And the S2 core dislocation is domain in the shear strain from 12.5% to 17.5%. More importantly, during the RK migration process in S2 types, both the shuffle-set and glide-set bond breaking and forming are involved. This finding could be used for the explanation of the shuffle-glide transition. Besides, the interest finding about the atoms along the dislocation can move simultaneously during the kink nucleation and the kink migration with two sides could be response to the missing long segment in the experiment. Therefore, I am guessing that whether it is possible that the shuffle-set perfect dislocation propagation has different mechanism. More information about the shuffle-set dislocation core structure is necessary for the further study.

I believe that this dislocation reaction pathway analysis can improve our understanding of dislocation motion in 3C-SiC and silicon and provide more evidences for solving the unclear issues in both of them.

5.2 Future work

For experimental aspects, most experimental studies in SiC are focusing on the hexagonal silicon carbide that which has a more complex slip system than 3C-SiC. More information about dislocation and stacking fault of 3C-SiC can help understanding the dislocation mobility well. On the other hand, the gap between the simulation and the experiment for the time length and

dimensions still exists. When it comes to the difference between the RK and LK which had been mentioned in section 3.4, little information is provided. In additions, some direct evidences about which types of kink structures is dominate, the reconstructed or unreconstructed ones, are needed. These evidences could include the kink structure images and the percentage of dangling atoms along the dislocation line.

The investigation about shuffle-set and glide-set issue in silicon is strongly constrained by the experiment limitation. For example, whether the dislocations which had been observed in such small pieces of area are the same with other dislocations in bulk silicon? More importantly, for solving this issue, the experiment of the shuffle-set un-dissociated dislocation is performing with a very high stress region. In such a high stress, the accompanied sample damage, cracks and other kinds of defects affect the analysis. On the other hand, by comparison of our shuffle-set perfect dislocation simulation result and the previous studies of screw dislocations, the conclusion about the shuffle-set perfect dislocation has a lower mobility than the screw dislocation is in contradiction with some experimental data in low stress regime (0-40MPa). The performances of the shuffle-set dislocation in different stress and temperature should be concerned.

For theoretical aspect, in this study, the morphologies of partial dislocation lines are analyzed by activation energy barriers which are calculated by NEB method under zero Kelvin. However, no experiment performed in that low temperature. And the kink migration and kink nucleation are also affected by other factors, such as temperature, strain-rate and even the geometry of the sample. For a better understanding of those influences on partial dislocation morphologies, multi-scale MD with long time is necessary due to the scale gap between the MD simulation and the experimental data. The Kinetic Monte Carlo simulation, parallel time method and accelerated molecule dynamics can help us to enlarge the length and time scales. Then the simulation could be more close to the real conditions.

On the other hand, in the dislocation motion study, whether the empirical potential can represent both the atomic configuration and the material property well is very important. This study about the dislocation in SiC and silicon are qualitative analyses for the applied empirical potential cannot reproduce the stacking fault energy very well. Therefore, for obtaining more accurate activation energy barriers in dislocation motion, further DFT calculation should be performed. Besides, our simulation results can be used in the dislocation dynamic (DD)

simulation on μm scale under different strain rate in which the dislocation motion in bulk semiconductor can be better illustrated.

Our study is aiming at explaining the observed experimental phenomena of dislocations in 3C-SiC and silicon, figuring out the controversy between those previous studies and experiment data. It is answering why these phenomena happened rather than how to change that. When it comes to the engineering view, there is still a gap between our MD study of dislocations and the application in the producing for a high quality semiconductor wafer. As mentioned in paragraph one in this section, the time-scale difference stop us for obtaining a directly study on the whole process of wafer growth with a long time. It is no possible for us to give a direct instruction on the engineering aspect (in second and millimeter scale) from this MD study (in picosecond and nanometer scale) right now. But we still need keep an open mind and be clearly aware that the major limitation is the computational capacity and nanotechnology. The MD simulation is a kind of atomic camera, tell us how the atoms or molecules interact with each other in nano-scale. I deeply believe, in the future, with the new nanotechnology like atoms can be located by human will, the MD method can be used as the manual book that guide people to produce the material with whatever structure character and performance they want with understanding the basic mechanism of defects.

Appendix A

Intrinsic stress calculation of GaN wafer

GaN as an attractive semiconductor material can be grown on the silicon by MOCVD (Metalorganic Chemical Vapor Deposition), the AlN buffer layers are employed for reduce the lattice mismatch between the substrate and GaN layers. The growth temperature of the GaN wafer is higher than 1100℃, then decrease to the room temperature. During the temperature circling, the thermal misfit caused by the different thermal expansion coefficient is response to the dislocations propagation in the wafer. Table A.1 shows the materials properties of silicon, AlN and GaN. When the GaN layer is growing on the (111) surface of silicon, the silicon substrate is under a compressive stress while the GaN layer is under a tensile stress for the reason that GaN has a smaller lattice constant than that of silicon. The same analysis, for the GaN grown on AlN, the AlN layer is in a tensile condition while the GaN layer is in the compressive stress.

Table A-1 Material parameters of Silicon, GaN and AlN**.**

Material parameters	Si (111)	GaN (0001)	AlN (0001)
Lattice constant (Å) a	5.430	3.189	3.112
Lattice mismatch ($\Delta a/a_{Si}$)	-	16.9%	19.0%
Thermal expansion coefficient α (10^{-6}/K) (linear)	2.59[a]	5.59[b]	6.43[c]
Thermal expansion mismatch	53.7%	-	15%
Biaxial modulus (Gpa)	228	450	470

(a) Yasumasa and Tokumaru, 1984.

(b) Roder *et al*., 2005

(c) Stephan *et al*., 2009

The biaxial modulus of anisotropic crystal (Wright, 1997) in Table A.1 is given by Equation. A-1. M_s represents the biaxial modulus when the C_{xx} comes from the elastic parameter matrix. These parameters are used for the stoney-formula for calculating the intrinsic stress of the thin layers in the growth system.

$$M_s = C_{11} + C_{12} - 2C_{13}(C_{13}/C_{33}) \quad \text{(A-1)}$$

The material thermal expansion coefficient $\alpha(T)$ can be generally written as Equation A-2. Table. A.2 show the parameter for the calculation of the thermal expansion coefficient. Furthermore, Figure A.1 shows the dependence of thermal expansion coefficient on temperature.

$$\alpha(T) = \{C_1[1 - \exp(-C_2(T - C_3) \times 10^{-3})] + C_4 T \times 10^{-4}\} \times 10^{-6} \ K^{-1} \quad \text{(A-2)}$$

Table A-2 Parameter for calculating the thermal expansion coefficient

Materials	C_1	C_2	C_3	C_4
Si	3.725	5.88	124.0	5.548
AlN	6.122	4.437	165.3	3.302
GaN	5.786	6.174	86.43	2.051

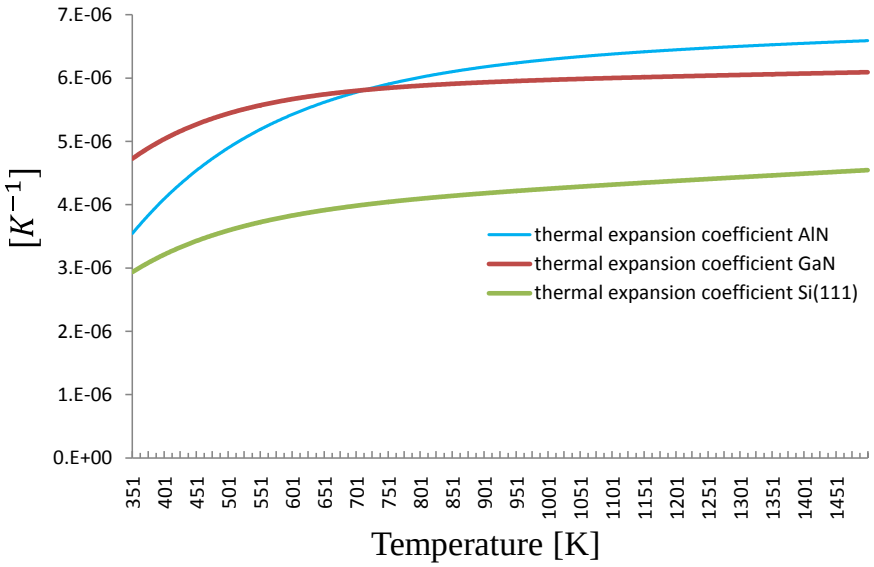

Figure A.1 The dependence of thermal expansion coefficient on temperature for Si, AlN and GaN.

Stoney formula (Freund and Suresh, 2003) is employed for the analyzing of the intrinsic stress of the film as shown in Equation. A-3. Here the curvature is written as κ. f shows the membrane force which is composed by the $f_{thermal}$ and $f_{epitaxial}$. They are defined by Equation A-4. α_s and α_f represent the lattice constants for the substrate and the film,

respectively. ΔT shows the temperature change while the h_f and M_f are the thickness and biaxial modulus of the film. For the multiple layers system, the relation between the wafer curvature and the each layer's stress condition is given by Equation A-5.

$$\kappa = \frac{1}{R} = \frac{6f}{M_s h_s^2} \tag{A-3}$$

$$f_{thermal} = M_f(\alpha_s - \alpha_f)\Delta T h_f$$
$$f_{epitaxial} = M_f\left(\frac{a_s - a_f}{a_s}\right)h_f \tag{A-4}$$

$$\kappa = \frac{6}{M_s h_s^2}\sum_{i=1}^{n}(\sigma_{i-intrinsic} + \sigma_{thermal})h_i \tag{A-3}$$

One of our calculation samples is shown in Fig. A.2. Notice that the thickness unit of the substrate silicon and the upper layers are different. The thin orange areas represent the AlN buffer layers with the thickness of 6nm. The growth temperature and curvature changing are shown in Fig. A.3 and Fig. A.4.

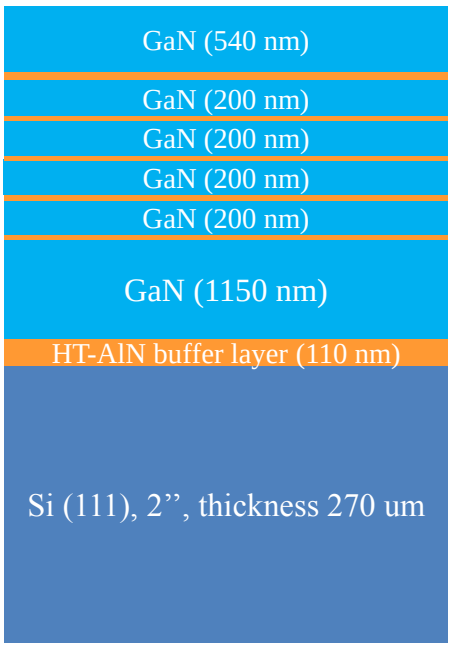

Figure A.2 GaN sample grown on silicon by MOCVD.

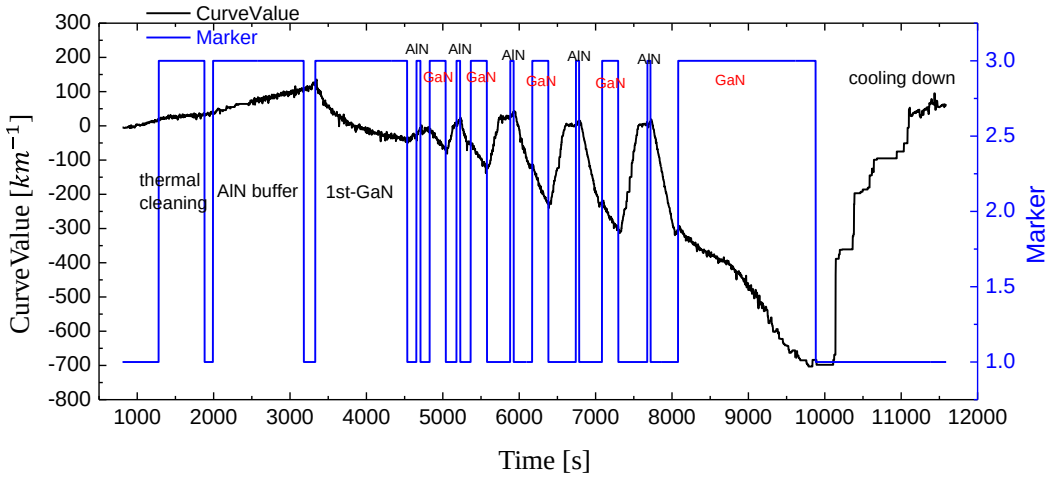

Figure A.3 Curvature of the sample for the whole growth process.

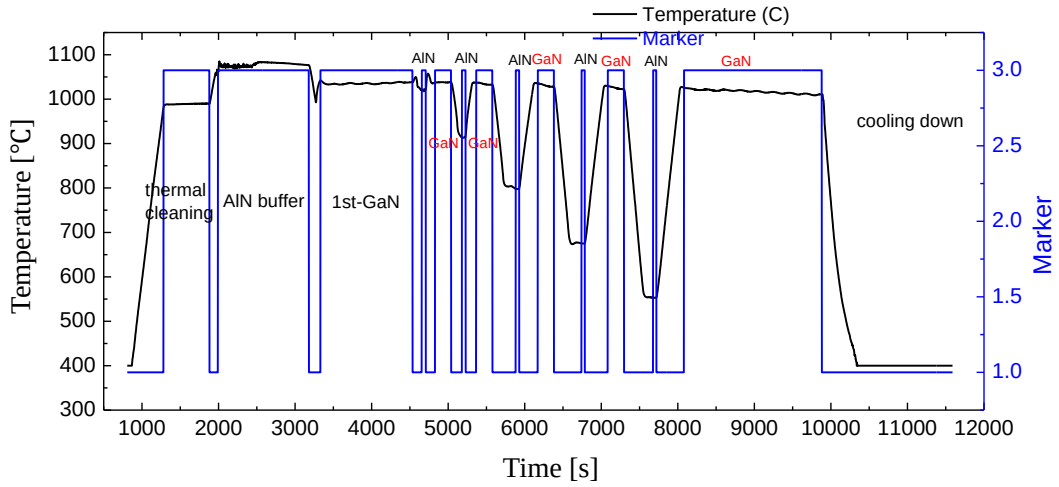

Figure A.4 Curvature of the sample for the whole growth process.

Here, some typical intrinsic stresses of the layers are shown for the following discussion. The intrinsic stress of the 110 nm HT-AlN is shown in Fig. A.5. The average intrinsic stress of the HT-AlN layer is became a constant value 1.70 GPa after 500 seconds' growth. Similar value was given by Raghavan and Redwing (2004). They showed that AlN film grown on 250μm has an intrinsic around 1.78 GPa. The intrinsic stress of AlN on Silicon is highly related on the lattice mismatch between these two materials. The layer of 1150 nm 1st-GaN is grown on the HT-AlN layers. The intrinsic stress of the 1st-GaN is shown in Fig. A.7. At the end of growth, the intrinsic stress is around -370 MPa. Wang *et al*. (2006) showed in their experiment data that

the intrinsic stress is around -304 MPa.

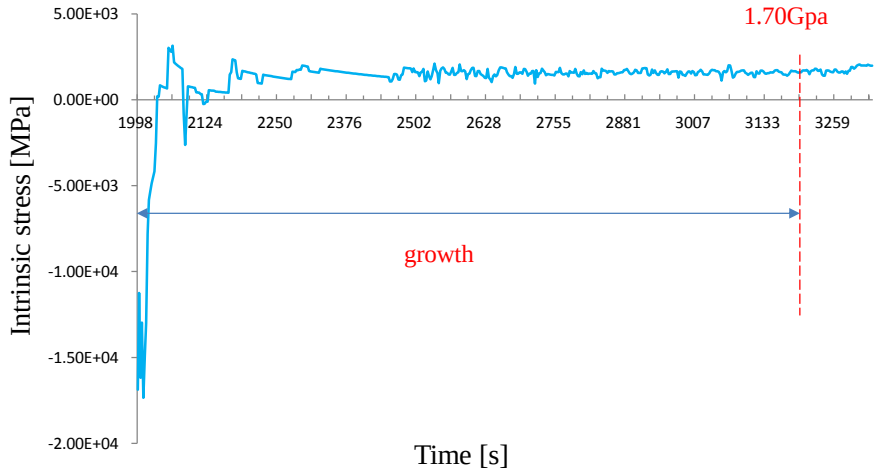

Figure A.5 Intrinsic stress of the 110nm HT-AlN. The time is ended when the next GaN layer is began to grow.

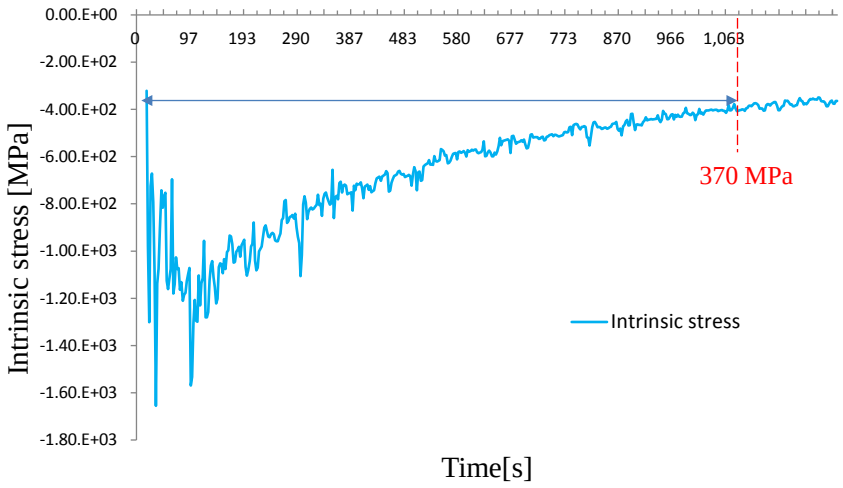

Figure A.6 Intrinsic stress of the 1150nm GaN grown on the 110nm HT-AlN. The dashed red line shows the growth ending time.

The thin AlN layers with different growth temperature in the sample are used for reduce the top layer's intrinsic stress for a high quantity of GaN wafer. The intrinsic stresses of these layers are not given here due to the stoney formula is not applicable here. H. Lahrèche *et al*. (2000) and S. Zamir *et al*. (2000) showed that a high quantity film of AlN should be grown in the temperature around 1100℃. These AFM images showed that the AlN films always have a rough surface with individual grains in the growth temperature lower than 1100℃. S. Zamir *et al*.

(2000) also pointed out that the low temperature can result in the uncover area on the top of the bottom layer. All of these make the application of stoney formula on the stress calculation of the 6 nm AlN layer meaningless.

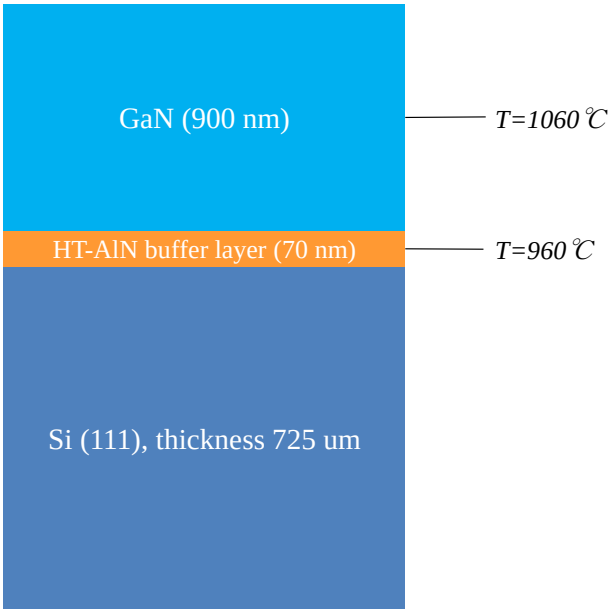

Figure A.7 GaN sample on silicon with the HT-AlN buffer layer.

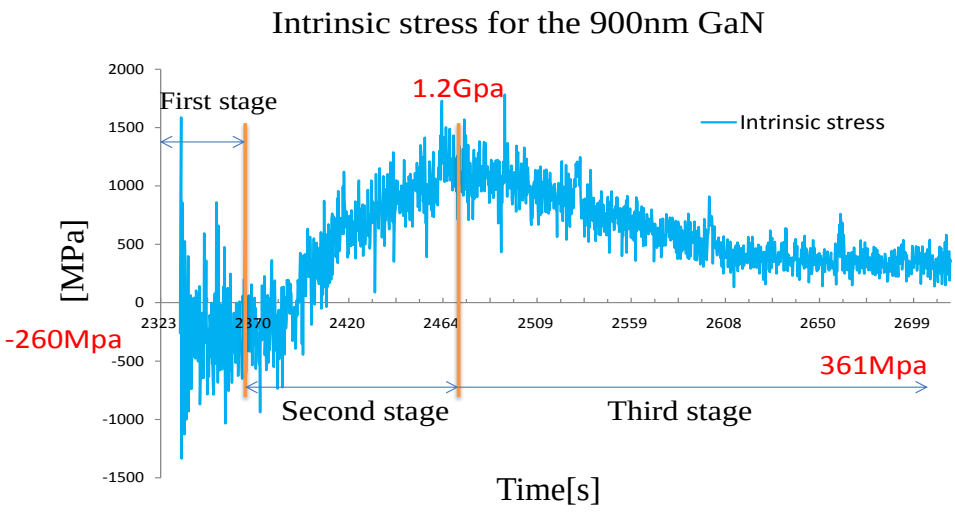

Figure A.8 Intrinsic stress of the 900nm grown on the silicon substrate with a 70nm HT-AlN buffer layer.

Moreover, for a better understanding of the growth mechanism of the GaN film, the following sample shown in Fig. A.7 is analyzed. Figure A.8 shows the intrinsic stress of the

GaN wafer during the whole growth period. It seemed that there are three stages for the growth process. For the 60 seconds first stage, GaN crystal is growing with the lattice constrained from HT-AlN layer. In this stage the GaN in island model is nucleated on the surface of the AlN. Next, in the second stage, GaN layer was grown without constrain, may because of the GaN inlands begin to coalescence with each other. The peak of the curve appeared at the 130 seconds that represent the completion of the island coalescence. At the beginning of third stage, the vanishing of the grain boundary, cracks and dislocations propagations appeared to reduce the intrinsic stress. The similar process had been observed by Krost and Dadgar (2004) with FEREM images as shown in Fig. A.9. This process is a typical Volmer-weber process.

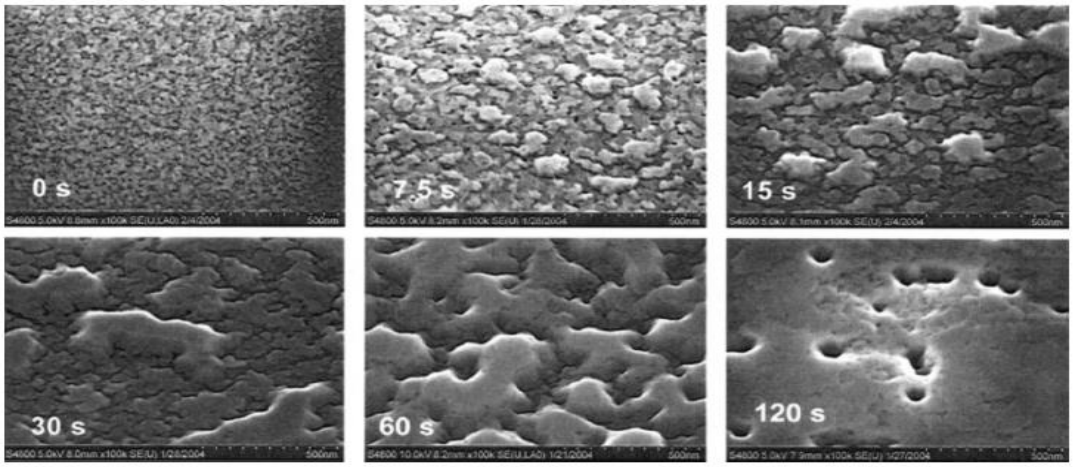

Figure A.9 Birds eye view FEREM images GaN grown on AlN (Krost and Dadgar 2004). With permission from AIP Publishing LLC.

Appendix B

This part is the reliability test for our simulation system including the code verification, potential validation and system stability.

Code verification and potential validation

For code verification, serval important material parameters are calculated shown in Table B-1 and Table B-2. In 3C-SiC, the lattice constant, cohesive energy and the elastic constant C11 which are obtained in this study agree with the previous simulation data in the Vashishta column (Vashishta, 2007). This consistent means our code is fine, which can be considered as the code verification. Moreover, by comparing with the experiments data in the Experiments column (Harrison, 1980; Feldman *et al*., 1968), the matched data means the Vashishta potential represent the 3C-SiC material well. That is the potential validation in 3C-SiC.

Table B-1 Material parameters of 3C-SiC

Material parameters	Experiments	Vashishta	This study
Lattice constant(Å)	4.3596	4.3581	4.3581
Cohesive/atom(eV)	-6.34	-6.3410	-6.3405
C11(Gpa)	390	390.0	389.86

In Table B-2, the material parameters of silicon are from this study, previous study (Bazant *et al*., 1997) and the experiments (Lucas *et al*., 2009). Via the comparison of these data, the code verification and potential validation is finished. The good agreement between these data show that our code is trustful and the EDIP can represent the silicon material well.

Table B-2 Material parameters of Si

Material parameters	Experiments	EDIP	This study
Lattice constant(Å)	5.43	5.430	5.430
Cohesive/atom(eV)	-4.63	-4.650	-4.650
C11(Gpa)	168	175	172

Stability analysis

Moreover, the system stability has been investigated via the result fluctuation analyze with different setting of parameters, such as kink widths, time step, relaxation time and model size. Fig. B.1 and Table B-3 show the activation energy barriers of LK migration in 30° partial dislocation and kink migration in 90° partial dislocation, respectively. The small difference

between the activation energy barriers indicate that the kink width effect can be ignored in the study of partial dislocation motion in 3C-SiC.

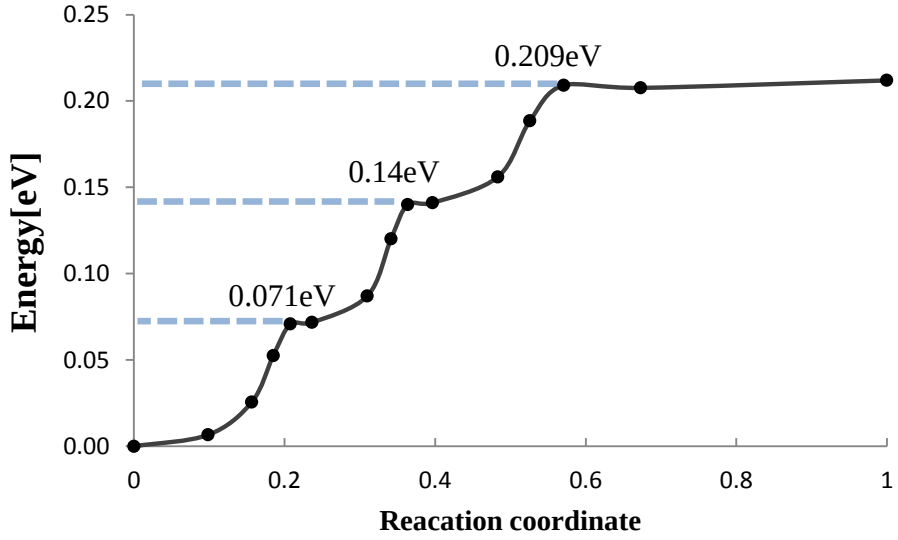

Figure B.1 Migration path of three left kinks in C-core 30 ° partial dislocation under the driving stress of 1.61GPa from kink width 10 to 13.

Table B-3 Activation energy barrier of Si-core 90° partial dislocation under the driving stress of 300MPa with different widths.

Kink width	Activation energy barrier [eV]
6 to 7	0.288
12 to 13	0.289

The kink width effect of dislocation in silicon is also investigated. As shown in Table B-4, there is very small difference between the activation energy barriers which are calculated with different kink widths under different shear strain. The kink width effect in shuffle-set perfect dislocation motion can be ignored.

Table B-4 Activation energy barrier of shuffle-set perfect dislocation kink migration in silicon with the shear strain 0.945% and 1.89%. (S1 dislocation core)

Kink width	Activation energy barriers [eV] (0.945%)	Activation energy barriers [eV] (1.89%)
6 to 7	0.6307	0.3939
9 to 10	0.6310	0.3942
12 to 13	0.6283	0.3956

As mentioned in Section 3.2, since the initial atomic model is created based on dislocation theory, the relaxation process is employed to make the artificial structure more nature. The relaxation process is performed with NVT ensembles, in which the atom numbers, simulation volume and temperature are keeping as setting constant. The system energy and temperature curve is shown in Fig. B.2. The initial energy decreasing is caused by the initial stress in the model had been released. During NVT relaxation, the temperature around 1 ± 0.0005 K while the system energy has a little fluctuation caused by temperature. The dependence of activation energy barrier on the relaxation time length is investigated. The results are shown in Fig. B.3. These energy barriers have a very little difference when the relaxation time is longer than 8 ps.

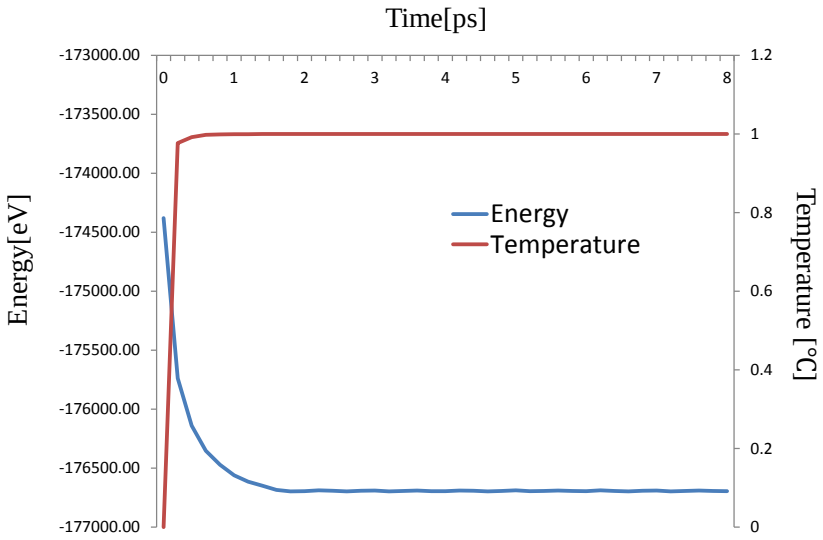

Figure B.2 Energy and temperature curve.

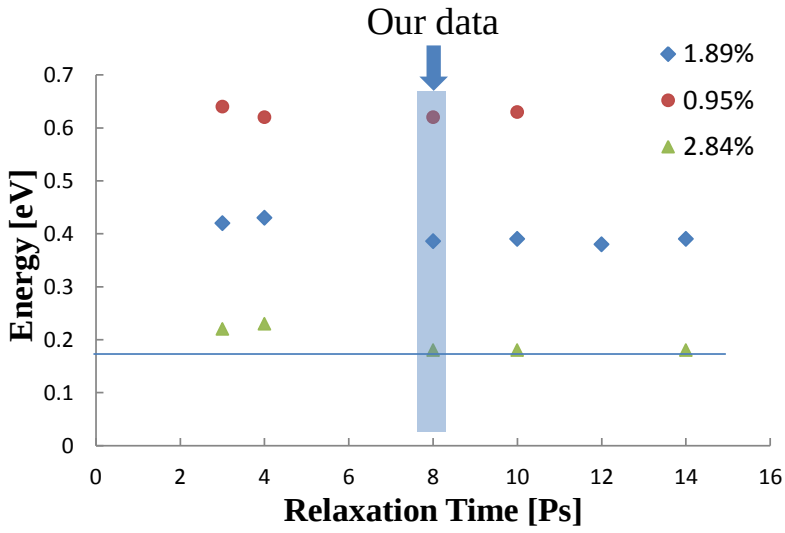

Figure B.3 The dependence of activation energy barrier on relaxation time.

Then, the model size effect is considered. A larger atomic model with 54432 atoms is employed to show that whether the simulation results will be varied with different model sizes. The large atomic model is obtained by adding atom planes in Z direction, which represent the thickness of the bulk. The same kink migration activation energy barriers are calculated, which is shown in Fig. B.4; the values from the two models agree with each other well. Therefore, the model size has no effect on our simulation results.

In addition, the dependence of simulation results on the time step has been discussed. Because of the MD simulation is based on the Newton's law, the atoms' position is updating by one time step. In other words, if we know the current atom positions at one moment, then the atom position for next moment can be obtained by the equation of motion. Usually, the time step is setting as the one tenth of the shortest atom bond vibration period in the system. Too large time step sometime makes bad simulations, while too small one could waste time and needs a large storage space. For the system stability analysis, the dependence of simulation results on the time step has been investigated. As shown in Table B-5, the kink migration activation energy barriers with different time steps in silicon with the shear strain of 0.945% are calculated. These data also have a small difference, since the time step is large than 0.2fs. In our study, the activation energy barriers are calculated under 1fs.

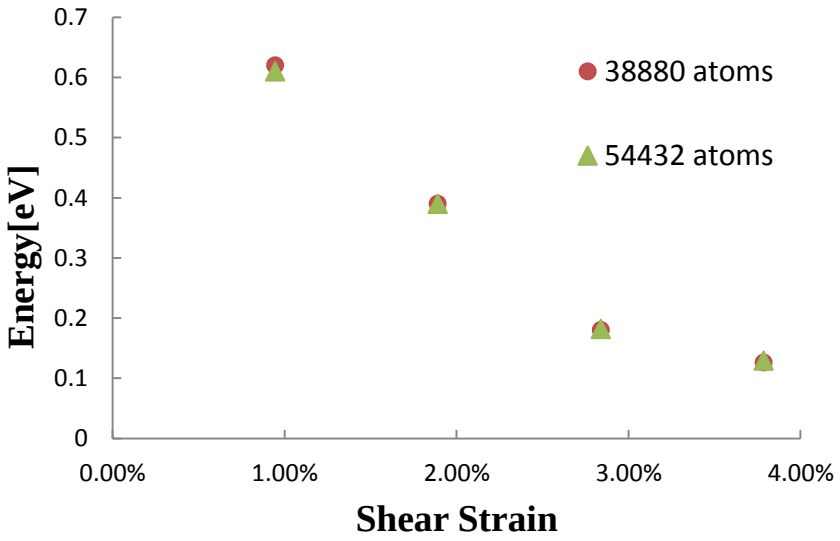

Figure B.4 Activation energy barriers of shuffle-set 60° perfect dislocation kink migration in silicon with different shear strain. The green triangle is the data calculated from the model with 54432 atoms while the red dot is for that of the model with 38880 atoms.

Table B-5 Activation energy barriers of S1 shuffle-set dislocation kink migration with different time step under the shear strain of 0.945 % in silicon.

Time step [fs]	0.2	0.5	0.8	1.0	1.5
Energy barriers [eV]	0.402	0.393	0.394	0.390	0.390

In conclusion, our simulation is reliable by testing the code, potential and various setting parameters. The code verification and potential validation part shows that our code is fine and the chose potentials can represent the material well. The result fluctuation analysis shows that the system is stable.

References

Alexander, H., Labusch, R. and Sander, W., Elektronenspin-resonanz in verformtem silizium, Solid State Communications, Vol.3, 357 (1965).

Alexander, H. and Teichler, H., Dislocations. Materials Science and Technology, 2013.

Bazant, M.Z., Kaxiras, E. and Justo, J.F., Environment-dependent interatomic potential for bulk silicon, Physical Review B, Vol.56, 8542 (1997).

Bennetto, J., Nunes, R.W. and Vanderbilt, D., Period-doubled structure for the 90 partial dislocation in silicon, Physical Review Letters, Vol.79, 245, (1997).

Blumenau, A.T., Fall, C.J., Jones. R., Öberg, S., Frauenheim, T. and Briddon, P.R., Structure and motion of basal dislocations in silicon carbide, Physical Review B, Vol.68, 174108 (2003).

Bulatov, V.V., Yip, S. and Argon, A.S., Atomic modes of dislocation mobility in silicon, Philosophical Magazine A, Vol.72, 453 (1995).

Cai, W., Bulatov, V.V., Justo, J.F., Li, J. and Yip, S., Dislocation core effects on mobility. In Dislocations in Solids, (ed. F.R.N. Nabarro and J.P. Hirth), Vol.12, (2004).

Carnahan, R.D., Elastic properties of silicon carbide, Journal of the American Ceramic Society, Vol.51, 223 (1968).

Chaussende, D., Mercier, F., Boulle, A., Conchon, F., Soueidan, M., Ferro, G., Mantzari, A., Andreadou, A., Polychroniadis, E.K., Balloud, C., Juillaguet, S., Camassel, J. and Pons, M., Prospects for 3C-SiC bulk crystal growth, Journal of Crystal Growth, Vol.310, 976 (2008).

Chow, T.P. and Tyagi, R., Wide bandgap compound semiconductors for superior high-voltage unipolar power devices, IEEE Transactions on Electron Device, Vol.41, 1481 (1994).

Duesbery, M.S. and Joos, B., Dislocation motion in silicon: the shuffle-glide controversy, Philosophical Magazine Letters Vol.74, 253 (1996).

Feldman, D.W., Parker, J.H., Choyke, W.J. and Patrick, L., Phonon Dispersion Curves by Raman

Scattering in SiC, Polytypes 3C, 4H, 6H, 15R, and 21R, Physical Review, Vol.173, 787 (1968).

Freund, L.B. and Suresh, S., Thin Film Materials Stress, defect formation and surface evolution, (2003).

Figge, S., Kröncke, H., Hommel, D. and Epelbaum, B.E., Temperature dependence of the thermal expansion of AlN, Applied Physics Letters, Vol.94, 101915 (2009).

Galeckas, A., Linnros, J. and Pirouz, P., Recombination-Induced Stacking Faults: Evidence for a General Mechanism in Hexagonal SiC, Physics Review Letters, Vol.96, 025502 (2006).

Godet J., Brochard, S., Pizzagalli, L., Beauchamp, P. and Soler, J. M., Dislocation formation from a surface step in semiconductors: An ab initio study, Physical Review B, Vol.73, 092105 (2006).

Godet, J., Hirel, P., Brochard, S. and Pizzagalli, L., Evidence of two plastic regimes controlled by dislocation nucleation in silicon nanostructures, Journal of Applied Physics, Vol.105, 026104 (2009).

Godet, J., Pizzagalli, L., Brochard, S. and Beauchamp, P., Theoretical study of dislocation nucleation from simple surface defects in semiconductors, Physical Review B, Vol.70, 054109 (2004).

Gomez, A., Cockayne, D.J.H., Hirsch, P. B. and Vitek, V., Dissociation of near-screw dislocations in Ge and Si, Philosophical Magazine, Vol.31, 105 (1975).

Ha, S., Benamara, M., Skowronski, M. and Lendenmann, H., Core structure and properties of partial dislocations in silicon carbide p-i-n diodes, Applied Physics Letters, Vol.83, 4957 (2003).

Hara, S., 構造緩和アモルファスシリコンの原子モデリング及び表面界面特性評価：分子動力学アプローチ, doctor thesis, 2004.

Harrison, W. A., Electronic Structure and the Properties of Solids: The Physics of the Chemical Bond (Freeman, San Francisco, 1980).

Heggie, M. and Jones, R., Solitons and the electrical and mobility properties of dislocations in silicon, Philosophical Magazine Part B, Vol.48, 365 (1983).

Henkelman, G., Jóhannesson, G. and Jónsson, H., Methods for finding saddle points and minimum

energy paths, Theoretical Methods in Condensed Phase Chemistry, Vol.5, 269 (2002).

Henkelman, G., Uberuaga, B.P. and Jónsson, H., A Climbing Image Nudged Elastic Band Method for Finding Saddle Points and Minimum Energy Paths, The Journal of Chemical Physics, Vol.113, 9901 (2000).

Hirsch, B.P., Ourmazd, A. and Pirouz, P., Relaxation of dislocation in deformed silicon, Microscopy of Semiconducting Materials, No.60, 29 (1981).

Hristu, R., Stanciu, S.G., Tranca, D.E., Matei, A. and Stanciu, G.A., Nonlinear optical imaging of defects in cubic silicon carbide epilayers, Scientific Reports 4, No.5258, (2014).

Hirth, J.P. and Lothe, J., Theory of Dislocations, 2nd edition, Wiley, New York, (1982).

http://www.ioffe.ru/SVA/NSM/ (Ioffe Institute, 2003).

Idrissi, H., Pichaud, B., Regula, G. and Lancin, M., 30° Si(g) partial dislocation mobility in nitrogen-doped 4H-SiC, Journal of Applied Physics, Vol.101, No.11, 113533 (2007).

Izumi, S., Ohtab, H., Takahashic, T., Suzukic, T. and Sakac, H., Shuffle-set dislocation nucleation in semiconductor silicon device, Philosophical Magazine Letters, Vol.90, 707 (2010).

Izumi, S. and Yip, S., Dislocation nucleation from a sharp corner in silicon, Journal of Applied Physics, Vol.104, 033513 (2008).

Kiani, S., Leung, K.W.K., Radmilovic ,V., Minor, A.M., Yang, J.-M., Warner, D.H. and Kodambaka, S., Dislocation glide-controlled room-temperature plasticity in 6H-SiC single crystals, Acta Materialia, Vol.80, 400 (2014).

Krost, A. and Dadgar, A., Evolution of stress in GaN heteroepitaxy on AlN/Si(111): From hydrostatic compressive to biaxial tensile, Applied Physics Letters, Vol.85, 3441 (2004).

Kolar, H.R., Spence, J.C.H. and Alexander, H., Observation of Moving Dislocation Kinks and Unpinning, Physical Review Letters, Vol.77, 4031 (1996).

Lahrèche, H., Vennéguès, P., Tottereau, O., Laügt, M., Lorenzini, P., Leroux, M., Beaumont, B. and

Gibart, P., Optimisation of AlN and GaN growth by metalorganic vapour-phase epitaxy (MOVPE) on Si (111), Journal of Crystal Growth, Vol. 217, 13 (2000).

Lancin, M., Texier, M., Regula, G. and Pichaud, B., Defects created in N-doped 4H-SiC in the brittle regime: Stacking fault multiplicity and dislocation cores, Philosophical Magazine, Vol.89, No.15, 1251 (2009).

Lara, A., Muñoz, A., Castillo-Rodríguez, M. and Domínguez-Rodríguez, A., Plastic behaviour of 4H–SiC single crystals deformed at temperatures between 800 and 1300 °C, Ceramics International, Vol.38, No.2, 1381 (2012).

Levinshtein, M.E., Rumyanstsev, S.L. and Michael, S.S., Properties of Advanced Semiconductor Materials: GaN, AIN, InN, BN, SiC, SiGe, John Wiley & Sons, 2001.

Li, J., Modelling and Simulation in Materials Science and Engineering, Vol.11, 173 (2003).

Li, S. and Gao, X.L., Handbook of Micromechanics and Nanomechanics, 2013.

Liu, K.X., Stahbush, R.E., Maximenko, S.I. and Caldwell, J.D., Differences in emission spectra of Si- and C-core partial dislocations, Applied Physics letters, Vol.90,153503 (2007).

Long, G.G., Chapman, K.W., Chupas, P.G., Bendersky, L.A., Levine, L.E., Mompiou, F., Stalick, J.K. and Cahn, J.W., Highly Ordered Noncrystalline Metallic Phase, Physical Review Letters, Vol.111, 015502 (2013).

Lucas, G., Bertolus, M. and Pizzagalli, L., An environment-dependent interatomic potential for silicon carbide: calculation of bulk properties, high-pressure phases, point and extended defects, and amorphous structures, Journal of Physics: Condensed Matter, Vol.22, 035802 (2009).

Maeda, K., Suzuki, K., Fujita, S., Ichihara, M. and Hyodo, S., Defects in plastically deformed 6H SiC single crystals studied by transmission electron microscopy, Philosophical Magazine A, Vol.57, 573 (1988).

Maximenko, S. I. and Sudarshan, T. S., Stacking fault nucleation sites in diffused 4H-SiC p-i-n diodes, Journal of Applied Physics, Vol.97, 074501 (2005a).

Maximenko, S.I., Pirouz, P. and Sudarshan, T.S., Investigation of the electrical activity of partial dislocation in SiC p-i-n diodes, Journal of Applied Physics, Vol.87, 033503 (2005b).

Muranaka, R., 3C-SiC 中の転位の移動度の反応経路解析, master thesis, the University of Tokyo, 2013.

Mussi, A., Rabier, J., Thilly, L. and Demenet, J.L., Plasticity and deformation microstructure of 4H-SiC below the brittle-to-ductile transition, Physica Status Solidi (c), Vol.4, No.8, 2929 (2007).

Nagasawa, H. and Yagi, K., 3C-SiC Single-Crystal Films Grown on 6-Inch Si Substrates, Physica Status Solidi (b), Vol.202, 335 (1997).

Nagasawa, H., Yagi, K., Kawahara, T. and Hatta, N., Reducing Planar Defects in 3C–SiC, Chemical Vapor Deposition, Vol.12, 502 (2006).

Neudeck, P.G. Trunek, A.J., Spry, D.J., Powell, J.A., Du, H., Skowronski, M., Huang, X.R. and Dudley, M., CVD Growth of 3C-SiC on 4H/6H Mesas, Chemical Vapor Deposition, Vol.12, 531 (2006).

Ning, X.J. and Pirouz, P., A Large Angle Convergent Beam Electron Diffraction Study of the Core Nature of Dislocations in 3C-SiC, Journal of Materials Research, Vol.11, 884 (1996).

Ohno, Y., Yonenaga, I., Miyao, K, Maeda, K. and Tsuchida, H., In-situ transmission electron microscopy of partial-dislocation glide in 4H-SiC under electron radiation, Applied Physics Letters, Vol.101, 042102 (2012).

Okada, Y. and Tokumaru. Y., Precise determination of lattice parameter and thermal expansion coefficient of silicon between 300 and 1500 K, Journal of Applied Physics, Vol.56, 314 (1984).

Okuno, T. and Saka, H., Electron microscope study of dislocations introduced by deformation in a Si between 77 and 873 K, Journal of Materials Science, Vol.48, 115 (2013).

Parrinello, M. and Rahman, A., Crystal Structure and Pair Potentials: A Molecular-Dynamics Study, Physical Review Letters, Vol.45, 1196 (1980).

Peach, M.O. and Koehler, U.F., The force exerted on dislocations and the stress field produced by

them, Physical Review, Vol.80, 1581 (1950).

Pizzagalli, L. and Beauchamp, P., Dislocation motion in silicon: the shuffle-glide controversy revisited, Philosophical Magazine Letters, Vol.88, 421 (2008a).

Pizzagalli, L., Demenet, J.L. and Rabier, J., Theoretical study of pressure effect on the dislocation core properties in semiconductors, Physical Review B, Vol.79, 045203 (2009a).

Pizzagalli, L., Godet, J. and Brochard, S., Glissile Dislocations with Transient Cores in Silicon, Physical Review Letters, Vol.103, 065505 (2009b).

Pizzagalli, L., Godet, J. and Brochard, S., Dislocation cores in silicon: new aspects from numerical simulations, Journal of Physics: Conference Series, Vol.281, 012002 (2011).

Pizzagalli, L., Pedersen, A., Arnaldsson, A., Jonsson, H. and Beauchamp, P., Theoretical study of kink on screw dislocation in silicon, Physical Review B, Vol.77, 064106 (2008b).

Plimpton, S., Fast Parallel Algorithms for Short-Range Molecular Dynamics, Journal of Computational Physics, Vol.117, 1 (1995).

Pilyankevich, N.A., Britun, F.V. and Kravets, A.V., Sov. X-ray spectroscopic investigation and calculation of the energy band structure of rare earth monophosphide and monosulphide, Physics of the Solid State, Vol.24, 862 (1982).

Pilyankevich, N.A. and Bbitun, F.V., Motion of partial dislocation in silicon carbide, Physica Status Solidi (a), Vol.82, 449 (1984).

Piluso, N., Camarda, M. and La Via, F., A novel micro-Raman technique to detect and characterize 4H-SiC stacking faults, Journal of Applied Physics, Vol.116, 163506 (2014).

Pirouz, P. and Yang, J.W., Polytypic transformations in SiC: the role of TEM, Ultramicroscopy, Vol.51, (1993), 189-214.

Rabier, J., High-stress plasticity and the core structures of dislocations in silicon, Physica Status Solidi (a), Vol.204, 2248 (2007).

Rabier, J., On the core structure of dislocations and the mechanical properties of silicon,

Philosophical Magazine Vol.93, 162 (2013).

Rabier, J. and Demenet, J.L., On the nucleation of shuffle dislocations in Si, Physica Status Solidi (a), Vol.202, 944 (2005).

Rabier, J., Pizzagalli, L. and Demenet, J.L., Dislocations in silicon at high stress, Dislocations in Solids, Vol.16, 47 (2010).

Raghavan, S. and Redwing, J. M., Intrinsic stresses in AlN layers grown by metal organic chemical vapor deposition on (0001) sapphire and (111)Si substrates, Journal of Applied Physics, Vol.96, 2995 (2004).

Rahman, A. and Parrinello, N., Polymorphic transitions in single crystals: A new molecular dynamics method, Journal of Applied Physics, Vol.52, 7182 (1981).

Raya, I.L.F. and Cockaynea, D.J.H., The observation of dissociated dislocations in silicon, Philosophical Magazine, Vol.22, 853 (1970).

Ren, Q., Joos, B. and Duesbery, M. S., Test of the Peierls-Nabarro model for dislocations in silicon, Physical Review B, Vol.52, 13223 (1995).

Roder, C., Einfeldt, S., Figge, S. and Hommel, D., Temperature dependence of the thermal expansion of GaN, Physical Review B, Vol.72, 085218 (2005).

Ruff, M., Mitlehner, H. and Helbig, R., SiC devices: physics and numerical simulation, Electron Devices, IEEE Transactions on, Vol.41, 1040 (1994).

Saka, H., Yamamoto, K., Arai, S. and Kuroda, K., In-situ TEM observation of transformation from shuffle to glide sets in Si under supersaturation of interstitials. Philosophical Magazine, Vol.86, 4841 (2006).

Sasaki, K., Sakuma, E., Misawa, S., Yoshida, S. and Gonda, S., High‐temperature electrical properties of 3C‐SiC epitaxial layers grown by chemical vapor deposition, Applied Physics Letters, Vol. 45, 72 (1984).

Sato, K., Hiraga, K. and Sumino, K., HVEM Structure Images of Extended 60°-and Screw

Dislocations in Silicon, Japanese Journal of Applied Physics, Vol.19, L155 (1980).

Savini, G., Theory of partial dislocations in SiC, Physica Status Solidi (c), Vol.4, 2883 (2007a).

Savini, G., Heggie, M.I. and Öberg, S., Core structures and kink migrations of partial dislocations in 4H–SiC, Faraday discussions, Vol.134, 353 (2007b).

Seitz, F., The plasticity of silicon and germanium, Physical Review, Vol.88, 722 (1952).

Severino, A., D'Arrigo, G., Bongiorno, C., Scalese, S., LaVia, F. and Foti, G., Thin crystalline 3C-SiC layer growth through carbonization of differently oriented Si Substrates, Journal of Applied Physics, Vol.102, 023518 (2007).

Shen, X.Q., Matsuhata, H., Ide, T. and Shimizu, M., Direct measurement of lateral macrostep velocity on an AlN vicinal surface by transmission electron microscopy, Journal of Applied Physics, Vol.111, 103529 (2012).

Shima, K., Izumi, S. and Sakai, S., Reaction pathway analysis for dislocation nucleation from a sharp corner in silicon: Glide set versus shuffle set, Journal of Applied Physics, Vol.108, 063504 (2010).

Shimojo, F., Kalia, R.K, Nakano, A. and Vashishta, P., Linear-scaling density-functional-theory calculations of electronic structure based on real-space grids: design, analysis, and scalability test of parallel algorithms, Computer Physics Communications, Vol.140, 303 (2001).

Skowronski, M., Liu, J.Q., Vetter, W.M., Dudley, M., Hallin, C. and Lendenmann, H., Recombination enhanced defect motion in forward-biased 4H–SiC p-n diodes, Journal of Applied Physics, Vol.92, 4699 (2002).

Stahlbush, R.E., Twigg, M.E., Irvine, K.G., Sumakeris, J.J., Chow, T.P., Losee, P.A., Zhu, L., Tang, Y. and Wang, W., Stacking fault formation sites and growth in thick-epi SiC PiN diodes, Materials Science Forum, Vol.457, 533 (2004).

Stillinger, F.H. and Weber, T.A., Computer simulation of local order in condensed phases of silicon, Physical Review B, Vol.31, 5262 (1985).

Sun, Y., Izumi, S., Sakai, S., Yagi, K. and Nagasawa, H., Saddle-shape warpage of thick 3C-SiC

wafer: effect of nonuniform intrinsic stress and stacking faults, Physica Status Solidi (b), Vol.249, 555 (2012).

Sun, Y., Izumi, S., Sakai, S., Yagi, K. and Nagasawa, H., Core element effects on dislocation nucleation in 3C–SiC: Reaction pathway analysis, Computational Materials Science, Vol.79, 216 (2013).

Taylor, G.I., The Mechanism of Plastic Deformation of Crystals. Part I. Theoretical, Proceedings of the Royal Society of London, Vol.145, 362 (1934).

Tersoff, J., Empirical interatomic potential for silicon with improved elastic properties, Physical Review B, Vol.38, 9902 (1988).

Vashishta, P., Kalia, R.K., Nakano, A. and Rino, J.P., Interaction potential for silicon carbide: A molecular dynamics study of elastic constants and vibrational density of states for crystalline and amorphous silicon carbide, Journal of Applied Physics, Vol.101, 103515 (2007).

Vasiliauskas, R., Mekys, A., Malinovskis, P., Juillaguet, S., Syväjärvi, M., Storasta, J. and Yakimova, R., Impact of extended defects on Hall and magneto resistivity effects in cubic silicon carbide, Journal of Physics D: Applied Physics, Vol.45, 225102 (2012).

Wang, J.F., Yao, D.Z., Chen, J., Zhu, J.J., Zhao, D.G., Jiang, D.S., Yang, H. and Liang, J.W., Strain evolution in GaN layers grown on high-temperature AlN interlayers, Applied Physics Letters, Vol.89, 152105 (2006).

Wang, C.Z., Li, J., Ho, K.M. and Yip, S., Undissociated screw dislocation in Si: Glide or shuffle set?, Applied Physics Letters, Vol.89, 051910 (2006).

Wang, L., Dimitrijev, S., Han, J., Iacopi, A., Hold, L., Tanner, P. and Harrison, H.B., Growth of 3C–SiC on 150-mm Si(100) substrates by alternating supply epitaxy at 1000 °C, Thin Solid Films, Vol. 519, 6443 (2011).

Wessel, K. and Alexander, H., On the mobility of partial dislocations in silicon, Philosophical Magazine, Vol.35, 1523 (1977).

Wright, A.F., Elastic properties of zinc-blende and wurtzite AlN, GaN , and InN, Journal of Applied

Physics, Vol.82, 2833 (1997).

Zamir, S., Meyler, B. and Zolotoyabko, E., The effect of AlN buffer layer on GaN grown on (1 1 1)-oriented Si substrates by MOCVD, Journal of Crystal Growth, Vol.218, 181 (2000).

Zhong, K., Meng, Q. and Zhao, Wei., A new stable core structure of 60 °shuffle dislocation in silicon and associated mobility behavior, Physica Status Solidi (b), Vol. 249, No. 6, 1250 (2012).

Zhu, Y., Xu, F., Qin, Q., Fung, W. and Lu, W., Mechanical properties of vapor liquid solid synthesized silicon nanowires, Nano Lett, Vol.9, 3934 (2009).

Zielinski, M., Ndiaye, S., Chassagne, T., Juillaguet, S., Lewandowska, R., Portail, M., Leycuras, A. and Camassel, Strain and wafer curvature of 3C-SiC films on silicon : influence of the growth conditions, J., Physica Status Solidi (a), Applications and materials science, Vol.204, 981 (2007).

Academic activities

Publications

1. Jing YANG, Satoshi Izumi, Ryota Muranak, Yu Sun, Shotaro HARA and Shinsuke Sakai, Reaction pathway analysis for differences in motion between C-core and Si-core partial dislocation in 3C-SiC, The Japan Society of Mechanical Engineers, Vol.2, No.4(2015).
2. Jing YANG, Satoshi Izumi and Shinsuke Sakai, Reaction pathway analysis for the shuffle-set perfect dislocation in silicon, to be submitted.

International conferences

1. Satoshi Izumi, Ryota Myranaka , Jing Yang, Yu Sun, Shotaro Hara and Shinsuke Sakai, Reaction pathway analysis for the partial dislocation mobility in 3C-SiC, International Symposium on Atomistic Modeling for Mechanics and Metaphysics of Material, July 22-24, 2013, Tokyo, JAPAN.
2. Jing YANG, Satoshi IZUMI, Ryota MURANAKA, Yu SUN, Shotaro HARA and Shinsuke SAKAI, Reaction pathway analysis for the partial dislocation mobility in 3C-SiC, 7th International Conference on Multiscale Materials Modeling, October 6th to 10th, 2014, Berkeley, California, USA

Award

Award for Best Technical Proposal in Global Center of Excellence for Mechanical Systems Innovation summer camp, 2013, Tokyo, Japan.

Acknowledgements

First and foremost, I would like to express my very great appreciation to Professor Satoshi Izumi. Thanks for giving me the precious opportunity to study in the University of Tokyo. Thanks for patience instructions and kind advices from Prof. Izumi during the past years. I have fostered an objective attitude with Izumi-sensei's help and guide. I would also like to offer my appreciation to Prof. Shinsuke Sakai, my improvement is depending on his kind support and the free environment in our laboratory. Prof. Sakai and Prof. Izumi also help me a lot when I was trying to find a job in Tokyo. My special thanks go to Prof. Shotaro Hara, thanks for his kind help when I was trapped by the NEB calculation problems. By the way I was always affected by his optimism attitude.

I would also like to thank Prof. Yoshikawa Nobuhiro and Prof. Yasushi Shibuta for serving as my committee members. Thanks for their valuable comments, which had improved the thesis a lot.

My special thanks are extended to the assistance professor Tanaka Hiro and HATANO Asuka, thanks for their looking after for these years. Thanks for so many pleasure talks and conversations. Wish their further research goes well. I am particularly grateful for the support and good times given by these lovely, energetic students who have graduated or not from out Lab. Thanks Mr. Takamoto So for helping with these programming and computer setting problems. Thanks Mr. Qu Qiang and Mr. Zhou Lijun. I really join the happy time be with you gays.

I am really not good at express my feeling in writing. What I want to say is that, as a foreigner Ph.D student, these professors, assistance professors and the students are the closest and important people for me. Thanks for their kind helps and caring which make my "journey" wonderful.

For the past three years, what I have got is far more than the degree. This study abroad experience is also a journey of my soul. I have realized who I am, what I am looking for in my life and be mature. Lucky for my personal and world values can be established in a real open world. Thanks Izumi-sensei again for giving me the chance to study abroad and thanks the financial support provided by China Scholarship Council.

To my beloved wife Wu Wenjing for all the things she had done for me. "You rise me up, makes me a better man."

My heartfelt thanks go to my parents. Thanks for their support all the times.